KU LEUVEN

FACULTEIT BIO-INGENIEURSWETENSCHAPPEN

Dip, a novel and inspiring bacteriophage-based mechanism for transcript protection in the host cell.

Structural and functional elucidation of a phiKZ encoded inhibitor of the RNA degradosome.

Promotoren:
Prof. Rob Lavigne
Departement Biosystemen
Afdeling Dier en Mens

Prof. dr. Ben Luisi

Masterproef voorgedragen
tot het behalen van het diploma van
Master of science in de bio-ingenieurswetenschappen:
cel- en gentechnologie

Tom Dendooven

juni 2016

KU LEUVEN

FACULTEIT BIO-INGENIEURSWETENSCHAPPEN

Dip, a novel and inspiring bacteriophage-based mechanism for transcript protection in the host cell.

Structural and functional elucidation of a phiKZ encoded inhibitor of the RNA degradosome.

Promotoren:
Prof. Rob Lavigne
Departement Biosystemen
Afdeling Dier en Mens

Prof. dr. Ben Luisi

Masterproef voorgedragen
tot het behalen van het diploma van
Master of science in de bio-ingenieurswetenschappen:
cel- en gentechnologie

Tom Dendooven

juni 2016

Acknowledgements

After an intensive period of nine months, I finally got to write this note of thanks as the finishing touch on my master's thesis. It has been a very interesting journey, not only at a scientific level, but also personally. As such, writing this thesis has had a big impact on me. I would like to reflect on all the people that have supported me and helped me throughout this journey.

First of all I would like to thank Prof. Dr. Ir. Rob Lavigne from the Lab of Gene technology, KU Leuven. Professor Lavigne has had a major role in pretty much all aspects of this project, as he arranged the collaboration with the lab of Prof. Dr. Ben Luisi, University of Cambridge, and provided financial support for my stay in Cambridge. Moreover, Prof. Lavigne has shown a sincere interest in the progress of this project and was always available for advice and sharp suggestions when an obstacle had to be overcome. Finally I would like to thank Rob for his extensive proofreading of this dissertation and his patience when listening to the sometimes crazy hypotheses that were formulated during this project.

Second, I would like to thank Prof Dr. Ben Luisi, Department of Biochemistry, University of Cambridge, for his kindness and eternal patience along the Journey. In particular, I would like to thank Prof. Luisi for hosting me in his lab and making me feel comfortable in the Luisi Group. Moreover, I would like to thank Ben for challenging me and exciting my scientific interest by letting me join his trips to synchrotrons, conferences, etc. and by inviting me to give a research seminar in the department, as well as introducing me to some very prominent researchers in the field of structural biology. Finally, I would like to thank Ben for his precious help and support during this project and for the great talks we had in the lab and during our journeys.

Next I would like to sincerely express my gratitude to Dr. Steven Hardwick, Department of Biochemistry, University of Cambridge. Steven has been an excellent supervisor and companion throughout this journey. His remarkable patience, calm, experience, expertise and in depth understanding of structural biology have been of incredible value to my thesis. There is a reason they call Steven 'The man who can crystallize anything'. Moreover, Steven has been a very pleasant colleague with a great deal of humor. I am looking forward to resume our daily trips to Boots.

Subsequently, I would like to thank Ir. Jeroen De Smet and Ir. Hanne Hendrix, Lab of Gene Technology, KULeuven, for their help and advice during this project. In particular, I would like to thank Hanne for her patience and help in the lab and for making this project enjoyable and exciting. As my daily supervisor, she learned me a great deal of new techniques. Moreover I would like to

thank Jeroen for his great and invaluable advice on experimental approaches and set up. His experience and expertise in interactomics have been of great use during this dissertation. In addition I appreciate Jeroen's extensive proofreading of this dissertation.

Also, I would like to thank Dr. Heather Bruce, Dr. Grecia Gonzalez and Dr. Kasia Bandyra, Department of Biochemistry, University of Cambridge, for their help and advice in processing crystallographic and SAXS data. In particular, my gratitude goes out to Dr. Nathan Cowieson, Beamline 21, Diamond lightsource, UK, for his great help and advice when processing the SAXS datasets.

Furthermore I would like to thank my parents and brothers for supporting me throughout this project. In particular, I would like to thank my father for the in depth reviews of this dissertation. In addition, I would like to thank my girlfriend, Ilona, for supporting me during this journey and providing some distraction when needed.

Last but not least, my gratitude goes out to all members of the Luisi group and the Lab of Gene Technology, for making this journey enjoyable and interesting. In particular, I would like to thank Bob Blasdel for his help with the western blot and RNA seq. data. Finally, I would like to thank my fellow master students for their support and for the pleasant times we had together.

Samenvatting

Pseudomonas aeruginosa is een opportunistische pathogeen die voornamelijk personen met een verzwakt immuunsysteem infecteert. Daarnaast kan deze bacterie vanwege zijn groeiende antibioticumresistentie de huidige antibioticum therapieën omzeilen. Daarom worden inventieve strategieën ontwikkeld om deze en andere multiresistente bacteriën te bestrijden. Bacteriofagen hebben na miljarden jaren van co-evolutie met hun gastheer een heus repertoire van mechanismen ontwikkeld om het gastheer metabolisme te activeren, heroriënteren of simpelweg te inhiberen. Aan de basis van deze mechanismen liggen interacties tussen faageiwitten en essentiële bacteriële complexen. Zowel in het kader van inventieve therapeutische toepassingen als nieuwe biotechnologische 'tools' kunnen een subset van deze interacties een directe bron van inspiratie zijn.

In deze dissertatie werd vertrokken van een inspirerende en tevens unieke interactie tussen een eiwit gecodeerd door de faag phiKZ en het RNA degradosoom van P. *aeruginosa*. Dit eiwit, dat tot het 'degradosoom interagerend proteïne' of Dip gedoopt werd, vormt een 'open-claw' dimeer structuur en bindt beide RNA bindingsplaatsen op het 'scaffold' domein van RNase E, dat deel uitmaakt van het RNA degradosoom. Zo verhindert Dip dat gestructureerde RNA species, zoals mRNA, binden met RNase E en gedegradeerd worden. In deze dissertatie werd via kristallografie, 'site-directed' mutagenese en interactomics de exacte RNase E bindingsplaats op het oppervlak van de Dip dimeren blootgelegd. Dip bindt de RNA bindingsplaatsen op het RNase E scaffold domein via grote, negatief geladen 'patches' op zijn oppervlak. Daarnaast tonen 'Small-angle X-Ray Scattering' (SAXS) experimenten aan dat er significante verschillen zijn tussen de kristal structuur van Dip en de structuur in oplossing. Dip vormt verdraaide en compacte klem-achtige dimeren, zoals bevestigd door '*ab initio*' SAXS modellen. Vervolgens suggereren SAXS data van een complex tussen Dip en het RNase E 'scaffold' domein dat Dip na binding van RNase E oligomeriseert tot een helix-achtig ensemble van drie Dip dimeren, mogelijks om duplex RNA na te bootsen. Tot slot tonen western blot experimenten aan dat *in vivo* Dip gehalten gradueel stijgen tussen 9 en 24 minuten na de infectie en dat Dip persistent aanwezig blijft gedurende de infectiecyclus. Daarom is het mogelijk dat phiKZ het gastheer RNA afbreekt in de eerste stappen van de infectie cyclus, waarna Dip geproduceerd wordt om het RNA degradosoom te inhiberen en het faag RNA te beschermen.

Dit onderzoek heeft mogelijks een eerste lid van de bacteriofaag gecodeerde RNA mimicry geïdentificeerd. Daarenboven opent het deuren naar nieuwe biotechnologische tools, en het RNA degradosoom als een antibacteriëel doelwit.

Summary

Pseudomonas aeruginosa is an opportunistic pathogen which predominantly infects immunocomprised persons. Because of its ever growing resistance against antibiotics, this bacterium can escape most of today's antibiotic therapies. Therefore, new and inventive strategies are required to combat these and other multidrug resistant superbugs. Bacteriophages, however, have had billions of years to develop a vast repertoire of strategies to activate, reorient or simply inhibit the host metabolism. Interactions between bacteriophage-encoded effector proteins and essential bacterial complexes form the base of these mechanisms. A subset of these phage-host interactions may serve as a source of inspiration for inventive therapeutic applications, as well as new biotechnological tools.

In this dissertation we set out from an inspiring and unique interaction between a phiKZ-encoded protein and the *P. aeruginosa* RNA degradosome. This protein, which is called the 'degradosome interacting protein' or Dip, adopts an 'open-claw' dimeric structure and hijacks both RNA binding sites on the scaffold domain of RNase E, which is part of the RNA degradosome. As such, Dip prevents structured RNAs, like mRNA, from being bound and degraded by the RNA degradosome. In this dissertation, crystallography, site-directed mutagenesis and interactomics approaches revealed the exact RNase E interaction site on the Dip dimer surface. Dip hijacks the RNA binding sites of the RNase E scaffold domain via large, acidic patches on its outer surface. In addition, Small-angle X-Ray Scattering (SAXS) experiments reveal significant differences between the crystal structure and the solution structure of Dip. As such, Dip forms a twisted and compact clamp-like structure, as is confirmed by '*ab initio*' SAXS models for Dip. Next, SAXS data of a complex of Dip and the RNase E scaffold domain suggest that Dip forms higher order and helical assemblies of three Dip dimers upon binding of RNase E, possibly to mimic duplex RNA. Finally, Western blot experiments indicate that Dip levels gradually increase between 9 and 24 minutes post phiKZ infection and that Dip is persistent during the remainder of the infection cycle. Therefore, it is possible that phiKZ degrades the host RNA during the initial stages of the infection cycle, after which Dip is being produced to inhibit the RNA degradosome and protect the phiKZ mRNA.

This research might have identified the first member of bacteriophage-encoded RNA mimicry. On top of that, it opens new doors towards novel biotechnological tools, as well as a possible new antibacterial target, the RNA degradosome.

List of Abbreviations

APS	ammonium persulfate
AUC	analytical ultracentrifugation
bp	base pairs
cAMP	cyclic adenosyl monophosphate
CF	cystic fibrosis
CRISPR-Cas	Clustered Regularly-Interspaced Short Palindromic Repeats-CRISPR associated protein
CTD	C-terminal domain of the endoribonuclease RNase E (scaffold domain)
Da	Dalton
Dip	degradosome interacting proteins
DNA	deoxyribonucleic acid
dNTP	deoxyriboncleotide triphosphate
ds	double stranded
EDTA	ethylenediaminetetraacetic acid
EM	electron microscopy
EMSA	electrophoretic mobility shift assay
EPS	extracellular polysaccharide
gp	gene product
Gst	glutathione S-transferase
HK	histidine kinase
HRP	Horse Radish Peroxidase
IPTG	isopropyl-β-D-1-thiogalactopyranoside
kb	kilobase
kDa	kiloDalton
LB	Lysogeny Broth
MALS	multi-angle light scattering
Mbp	megabasepairs
MME	monomethyl ether
mRNA	messenger RNA
MW	molecular weight
nvRNAP	non-viral RNA polymerase
NTD	N-terminal domain of the endoribonuclease RNase E
OD_{600nm}	optical density at 600 nm
ORF	open reading frame

PBS	phosphate buffered saline
PCR	polymerase chain reaction
PEG	polyethylene glycol
pfu	plaque forming units
PNPase	polynucleotide phosphorylase/polyadenylase
QS	quorum sensing
RBS	ribosomal binding site
RNA	ribonucleic acid
RNAi	RNA interference
RNAP	RNA polymerase
RNase	endoribonuclease
RND	resistance nodulation-cell division
RppH	RNA pyrophosphohydrolase
RR	response regulator
rRNA	ribosomal RNA
SAXS	small-angle X-ray scattering
SEC	size-exclusion chromatography
SD	standard deviation
SDS-PAGE	sodium dodecyl sulphate-polyacrylamide gel electrophoresis
T3SS	type 3 secretion system
TAE	tris, acetic acid, EDTA buffer
TCS	two-component systems
TEMED	N,N,N',N' tetramethylethylenediamine
T_{room}	room temperature
tRNA	transfer RNA
UTR	untranslated region
vRNAP	viral RNA polymerase

List of Publications

- Van den Bossche A, Hardwick SW, Ceyssens P-J, Hendrix H, Voet M, Dendooven T, Bandyra KJ, De Maeyer M, Aertsen A, Noben J-P, Luisi B.F, Lavigne R (2016) Structural elucidation of a novel mechanism for the bacteriophage-based inhibition of the RNA degradosome. *eLife,* In submission.

List of Tables

List of Figures

Table of contents

1. Introduction and background

1.1. *Pseudomonas aeruginosa,* a versatile and opportunistic pathogen

In 1882, Gessard isolated a rod-shaped bacterium and named it *Bacillus pyocyaneus*, as its colour was blue-green by the production of the pyocyanin pigment. This bacterium, nowadays known as Pseudomononas *aeruginosa*, is a Gram-negative, facultative anaerobic, monoflagellated Ɣ-proteobacterium and a member of the family of *Pseudomonaceae* (Silby *et al.*, 2011). *P. aeruginosa* is capable of colonizing a wide range of environmental niches, like terrestrial and aqueous habitats, plants and animal tissues, due to its high genomic complexity and metabolic and physiologic versatility (Stover *et al.*, 2000). A common anecdote among *Pseudomonas* scientists is that for any real or imagined hydrocarbon, there is at least one *Pseudomonas* species that can metabolize it given oxygen or nitrite is present and a sufficient amount of time is available.

Moreover, *P. aeruginosa* is an important opportunistic human pathogen causing often lethal infections in immunocompromised hosts, hospitalized patients and people with cystic fibrosis (CF). This success as a pathogen is due substantially to the versatility and adaptability encoded in its large genome, which contains a complex regulatory network (Galán-Vásquez *et al.*, 2011; Gellatly & Hancock, 2013). Furthermore, its ability to form biofilms and the production of a vast repertoire of virulence factors add to this pathogenicity (Gellatly & Hancock, 2013). Finally, due to its high antimicrobial resistance *P. aeruginosa* is extremely hard to eradicate and is therefore a member of the ESKAPE pathogens, which can escape most of the current antibiotic therapies (Rice, 2008). The search for new antibiotic classes has suffered from an 'innovation gap' during the last five decennia and only four new classes of antibiotics have been discovered since the early 1960's (see Figure 1) (Bassetti *et al.*, 2013). It is clear that the need for new and innovative strategies to develop novel antibacterial therapies against *P. aeruginosa* is high (see 1.1.4).

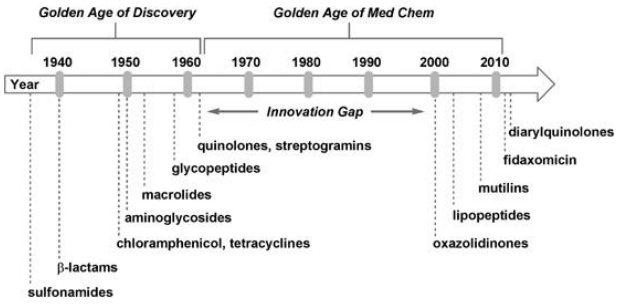

Figure 1: Timeline of antibiotic classes discovered between 1930 and 2000. After the golden age of antibiotic discovery (1940-1960) no new classes of antibiotics were discovered between 1962 and 2000, creating a significant innovation gap in the genomic era (adapted from Walsh & Wencewicz, 2013).

1.1.1. *P. aeruginosa* as a pathogen: susceptibility and symptoms

As stated before, *P. aeruginosa* causes both acute and chronic infections mainly in immunocompromised hosts. Therefore, infections are mostly nosocomial, although community acquired infections are reported as well. In these cases the host immune system is impaired, for example by HIV-infection, age or cancer (Gellatly & Hancock, 2013).

P. aeruginosa infers acute infections in the bloodstream, on the skin or in soft tissues, but can also cause urinary tract infections and surgical site infections (Driscoll *et al.*, 2007). When *P. aeruginosa* is not eradicated during the acute phase of a lung infection, it can adapt to the lung environment and produce a biofilm, which results in a chronic infection (see 1.1.2). In this case the bacteria become less inflammatory and lose several virulence factors. Also, they evolve into a non-motile mucoid morphotype and become more resistant to antibiotics (Mathee *et al.*, 2008). Such chronic *Pseudomonal* lung infections occur frequently in CF patients, as more than 80% of them acquire a chronic lung infection by adolescence, reducing their life expectancy. In these patients, a point mutation in the cystic fibrosis transmembrane regulator (CFTR), which is a cAMP-dependent chloride channel, is considered to be one of the most important causes. Malfunctioning of the CFTR thickens and dehydrates the airway surface liquid (ASL), hindering mucociliary clearance from the conducting airways, which allows the bacteria to reside in this altered ASL (Sadikot *et al.*, 2005). Furthermore, *P. aeruginosa* infections are the primary cause of death in burn wound patients, where 75% of the fatalities are caused by infections rather than the by burn wounds (Yali *et al.*, 2014). Finally *P. aeruginosa* is the second most common cause of ventilator associated pneumonia (VAP), hospital acquired pneumonia (HAP) and healthcare associated pneumonia (HCAP), where *P. aeruginosa* can grow in biofilms on the endotracheal tube (Williams *et al.*, 2010).

1.1.2. The main virulence factors of *P. aeruginosa*

P. aeruginosa strains isolated from acute infections exhibit significantly different phenotypes from those isolated from chronic infections. Both phenotypes produce different virulence factors, each contributing to their success as a pathogen (Smith *et al.*, 2006). The major virulence factors produced by isolates from acute infections comprise the type 3 secretion system exotoxins (T3SS), flagella and type IV pili, the siderophore pyoverdine and proteases (Sadikot *et al*, 2005; Ben Haj Khalifa *et al.*, 2011; Li *et al.*, 2014). However, acute virulence factors are downregulated during chronic infection. These cells overexpress the exopolysaccharide alginate, causing the cells to become mucoid, and form biofilms (Balasubramanian *et al.*, 2013; Gellatly & Hancock, 2013).

In acute infections, *P. aeruginosa* has one single polar flagellum, for 'swimming' motility, and several much shorter type IV pili for 'twitching' motility. These appendages also function as adhesins and can cause a first inflammatory response (Miao *et al.*, .2007). After adhesion to the host epithelial cells, *P. aeruginosa* uses the 'needle-like' multicomponent machinery of the T3SS to inject effector molecules and other virulence factors in the host cells. Depending on the strain, *P. aeruginosa* can produce and inject four effector proteins: ExoY, ExoT, ExoS, and ExoU. In particular ExoU, a phospholipase, is estimated to be 100 times more cytotoxic than ExoS, causing rapid necrosis of the host eukaryotic cell through loss of cell membrane integrity (Hauser, 2010). Other important injected virulence factors comprise exotoxin A, which inhibits elongation factor 2 (EF2) and thereby protein synthesis (Schultz *et al.*, 2000), and pyoverdine, a siderophore that sequesters iron from the host environment and induces the upregulation of both pyoverdine itself and exotoxin A (Shen *et al,* 2002). At last several elastases, protease IV and alkaline proteases inhibit the host immune system by degrading important components like fibronectin and complement proteins (Toder *et al.*, 1994; Engel *et al.*, 1998, Laarman *et al.*, 2012;). In addition, type six secretion systems are able to deliver toxin components of toxin-immunity systems to other bacteria. This way *P. aeruginosa* ensures an increased fitness compared to the targeted bacteria (Hood *et al.*, 2010).

Following an acute infection stage, a *P. aeruginosa* infection may evolve to a chronic infection. The planktonic cells form microcolonies and start overexpressing the extracellular polysaccharide (EPS) alginate. This results in the formation of mucoid cells, which will trigger biofilm formation. A biofilm is a surface-associated multicellular bacterial community, encapsulated in a self-produced extracellular matrix. This matrix is composed of polysaccharides, proteins and nucleic acids, mediating cell-to-cell and cell-to-surface interactions (Flemming & Wingender, 2010). Residing in the chronic infection stage, *P. aeruginosa* downregulates the expression of most acute virulence factors and thus becomes less virulent. On the other hand, these biofilm lifeforms are more resistant to antibiotic therapies and host immune responses, both through physical and genetic mechanisms (see 1.1.4). Finally, the global gene regulation in biofilm cells significantly differs compared to that of planktonic cells and is strongly controlled by quorum sensing (QS) (see 1.1.3).

1.1.3. The extensive regulatory network of *P. aeruginosa*

The *P. aeruginosa* PAO1 (the most studied strain) genome is 6.3 Mbp large and encodes 5.570 Open Reading Frames (ORF's), a number that approaches that of lower eukaryotes, like *Saccharomyces cerevisiae* (Stover *et al.*, 2000). Over time the *P. aeruginosa* genome has undergone elaborate rearrangements and has acquired many genes to adapt to specific habitats. To achieve this metabolic versatility its genome exhibits an extensive and dynamic regulatory repertoire (Mathee *et al.*, 2008).

Approximately 8% of the genes in the genome are predicted to code for regulatory proteins, although the function of many genes remains unknown (Winsor *et al.*, 2011).

A first important regulatory mechanism in *P. aeruginosa* is quorum sensing, which is used by many bacteria to respond to a new environment in a density-dependent manner, and thus regulates gene expression on a population level. In QS, bacteria express and secrete membrane-diffusable autoinducers (queromones). When a concentration threshold is reached, these autoinducers activate downstream transcription regulators, often promoting group survival (Stevens *et al.*, 2012). *P. aeruginosa* employs QS to control the expression of various virulence factors, such as motility, biofilm formation, extracellular proteases, the response to host immune signals, and also feed forward autoregulation of the autoinducer genes themselves (Williams & Camara, 2009). For this, *P. aeruginosa* mainly uses two types of QS pathways, each with their own autoinducers. The *rhl and las* systems, which are the representative systems of the first type of QS, use N-acyl-homoserine-lactones (AHL's) as autoinducers. Together they affect the expression of approximately 10% of the *P. aeruginosa* transcriptome (Schuster & Greenberg, 2006). The second type of QS pathways uses 2-alkyl-4-quinolones (AQ's) as autoinducer (Diggle *et al.*, 2007).

Another important circuit of cellular signaling is the two-component system (TCS). The archetypical TCS contains a membrane integrated sensory histidine kinase (HK) and a subsequent cytoplasmic response regulator (RR), both organized in a single operon (Rodrigue *et al.*, 2000). The periplasmatic N-terminal domain of the HK is a sensing domain which detects specific stimuli. Upon activation of this N-terminal sensing domain, the cytoplasmic C-terminal domain undergoes dimerization, followed by cross-phosphorylation at the conserved histidine residues. Next, the orthophosphate is translocated to an aspartate residue in the receiver domain of the RR, resulting in a conformational change and activation of its output domain. This output domain often binds DNA and modulates expression levels (Stock *et al.* 2000). In the *P. aeruginosa* genome, just under 10% of the genes encode regulatory proteins, of which a major subset are the genes encoding 64 HKs and 72 RRs, with 123 TCSs annotated in total (Rodrigue *et al.*, 2000; Chen *et al.*, 2004; Galperin, 2006; Gooderham & Hancock, 2009). This equips the bacterium with a sophisticated machinery to regulate diverse metabolic adaptations, virulence and antibiotic resistance systems. One important TCS is the GacSA system, which is involved in virulence regulatory pathways. This TCS plays a crucial role in quorum sensing (QS), secondary metabolites and the expression of several virulence factors. Furthermore TCSs also regulate the transition from an acute infection state to a chronic infection state and thus directly coordinate biofilm formation, by controlling the expression of the two regulatory RNAs RsmZ and RsmY (Reimmann *et al.*, 1997; Coleman *et al.,* 2003). Some other, well characterized TCS include the PhoP-PhoQ and PmrA-PmrB systems, that respond to low cation concentrations and mediate

resistance to polymyxin B and cationic antimicrobial peptides (Mcphee *et al.*, 2006; Macfarlane *et al.*, 2000).

1.1.4. *Pseudomonas aeruginosa*: a superbug driving the development of inventive new therapies

Due to its remarkable capacity to withstand antibiotics, *P. aeruginosa* has joined the ranks of 'superbugs'. This decreased susceptibility for antibiotics is the result of high intrinsic resistance (encoded in the genome) coupled to the fast development of acquired resistance (horizontal gene transfer of mobile elements and mutations). Finally, adaptive resistance mechanisms (differences in gene expression) further add to this pathogen's clinical resistance, often to an untreatable level (Breidenstein *et al.*, 2011). The most important mechanisms of resistance include active efflux of the antibiotic by efflux pumps, modification of the targets, impermeability of the cell membrane and enzymatic deactivation of the drug (Courvalin, 2008).

Wild type *P. aeruginosa* cells are less susceptible to most antibiotics than other Gram-negative bacteria because of the intrinsic low permeability of their outer membrane. This large exclusion limit is mainly due to the limited number of large OprF porins, the major porins in *P. aeruginosa*, and the smaller size of the OprD and OprB porins (Breidenstein *et al.*, 2011). Other important intrinsic secondary resistance mechanisms comprise the multidrug resistance efflux pumps, in particular the resistance nodulation-cell division (RND) systems MexAB-OpsM and MexXY-OprM. These pumps mediate the efficient efflux of many antibiotics, like fluoroquinolones, carbapenems, β-lactams and aminoglycosides (Stover *et al.*, 2000; Schweizer, 2003; Poole, 2011).

On top of its high intrinsic resistance, *P. aeruginosa* can become even more resistant through the acquisition of inheritable resistance traits, collectively known as acquired resistance. Antibiotic resistance genes can be encoded in plasmids, integrons, prophages, transposons and resistance islands, which are acquired by conjugation, transformation or transduction (Breidenstein *et al.*, 2011). New β-lactamases, which offer resistance against penicillins and cephalosporins, as well as carbapenemases and aminoglycoside modifying enzymes are often exchanged between *P aeruginosa* strains (Poirel *et al.*, 2010; Poole, 2005). Another way for *P. aeruginosa* to acquire resistance is through mutations. Mutation frequencies rise during stress conditions, such as the presence of DNA-damaging agents or during growth in a biofilm, leading to 'breakthrough' mutations which make *P. aeruginosa* harder to treat. Loss of expression of OprD and overexpression of efflux pumps are examples of mutations in regulatory genes or elements in *P. aeruginosa* (Breidenstein *et al.*, 2011; Poole, 2011). Furthermore, defects in the *mutS*/*mutL*/*mutU* mismatch repair system during chronic

infections, e.g. in the CF lung, lead to hypermutable cells, consequently with higher rates of acquired antimicrobial drug resistance (Oliver *et al.*, 2002; Kenna *et al.*, 2007).

The best studied form of adaptive resistance in *P. aeruginosa* is biofilm formation, which modulates expression of many genes and leads to effects on the cell envelope and upregulation of efflux pumps and enzymes. Although not yet fully understood, bacteria living in biofilms can be up to 100 or 1000 times more resistant to drugs than planktonic cells (Drenkard, 2003). At first it was believed the EPS matrix acts as a barrier to antibiotic penetration, but this was disproved for e.g. fluoroquinolones (Walters *et al.*, 2003; Olsen, 2015). Furthermore, slow growth rates inside the biofilm and altered metabolic activity confer protection against certain classes of antibiotics, like β-lactams and tetracycline (Tanaka *et al.*, 1999, Brooun *et al.*, 2000, Olsen, 2015). In addition, resistance against cationic antimicrobial peptides is conferred by large amounts of extracellular DNA in the biofilm matrix, which cause a cation limited environment. Moreover, 'persister' cells are believed to be important contributors to the persistence of biofilms. Finally, antibiotic resistance in biofilms might result from up- or downregulation of specific genes. For example, low oxygen levels in biofilms alter the composition of efflux pumps in *P. aeruginosa* (Olsen, 2015; Schaible *et al.*, 2012). Furthermore, a new efflux system, PA1874-1877, was discovered and proved to be upregulated in biofilm phenotypes (Zhang & Mah, 2008). Although extensive research is being conducted towards therapeutic anti-biofilm compounds, very few studies have made it to clinical trials. Garlic extract is the only compound that has been tested in a clinical trial, but without significant results (Rasamiravaka *et al.*, 2015).

The increasing Multi-drug resistance in pathogenic bacteria combined with the 'gap' in the discovery of new antibacterial therapies (see Figure 1) complicates effective treatment. To tackle this problem, different approaches are being investigated, from searching for new antibacterial targets, over reversing current resistance mechanisms to passive and active immunization (Jakobsen *et al.*, 2012; Yoshida *et. al.*, 2010; Horn *et al.*, 2010; Westritschnig *et al.*, 2013). Within the context of this dissertation, one interesting and rather unexploited strategy comprises RNA decay as a novel therapeutic target in bacteria. In bacteria, transcription and translation are coupled and the mRNA half-life is under 2 minutes. Furthermore, bacterial mRNA is not capped (5' 7-methylguanosine (m^7 G) cap) and rarely has a poly A (adenine) tail. In eukaryotic cells, on the other hand, the mRNA metabolic steps are compartmentalized, with a mRNA half-life of minutes to days, and the mRNA is 5' m^7 G-capped and 3' polyadenylated. These fundamental differences in RNA metabolism indicate that the molecular machinery mediating bacterial (pathogen) and eukaryotic (host) RNA degradation differs as well (Eidem *et al.*, 2012). The mRNA decay initiator machinery is a multi-protein complex termed the RNA degradosome (see 1.3). The main component of the RNA degradosome in

Gram-negative bacteria is RNase E, which acts as a scaffold for the other degradosome components and performs the initial endoribonucleolytic step in mRNA decay (Carpousis 2002). Furthermore, there is no significant amino acid homology between bacterial RNase E and human proteins. Finally, in eukaryotes RNases predominantly mediate RNA decay in an exonucleolytic way, while in bacterial RNA decay mainly involves an endonucleolytic cleavage by RNases. Considering these observations it is plausible that, based on natural RNase E inhibitors, a small molecule inhibitor against *Pseudomonas* RNase E could be designed, with no predicted toxicity to humans (Eidem *et al.*, 2012). To date, no inhibitory molecules based on natural inhibitor design are reported. However, virtual high throughput screens have led to small molecule inhibitors which bind at sites of the N-terminal catalytic half of RNase E in *E. coli* and *Mycobacterium tuberculosis* and successfully inhibit RNA decay (Kime *et al.*, 2015).

1.2. Bacteriophages of *P. aeruginosa*: focus on phiKZ giant phages

Bacteriophages comprise a very abundant group of organisms with a great diversity, populating a multitude of niches and hosts on earth. It is assumed that their global population exceeds 10^{30}, exceeding the bacterial population five- to tenfold (Hendrix, 2000). The phage genome, together with a (lipo-) protein coat or capsid, forms the phage particle. 96% of the classified bacteriophages are tailed phages with icosahedral or elongated heads, containing dsDNA, grouped in the order of the *Caudovirales*. However, phages with ssDNA, dsRNA and ssRNA genomes are reported as well (Maniloff & Ackermann, 1998).

Two types of reproduction cycles are used by bacterial viruses to multiply: the lysogenic and lytic infection cycle. The latter, which is of interest in this thesis, starts with the recognition of specific surface receptors by the phage tail fibers and attachment on the bacterial cell surface (see Figure 2). Next, the phage injects its genome into the host cell and transcription of the early phage genes is initiated. Most of these genes take part in the conversion of the host metabolism in order to achieve efficient phage reproduction. This host conversion is put in motion by phage-host protein-protein interactions (see 1.2.3). Subsequently, the phage genome is replicated and new phage particles are assembled inside the host. Once the 'burst size' is reached, the host cell lyses and the phages are released (Clokie *et al.,* 2011). Bacteriophages are termed strictly lytic when they only replicate by the lytic cell cycle, whereas temperate phages also undergo a lysogenic phase (Gallet *et al.*, 2012). During the lysogenic cycle the bacteriophage genome replicates with the host, either as a plasmid or incorporated into the host genome, without cell lysis (Clokie *et al.,* 2011).

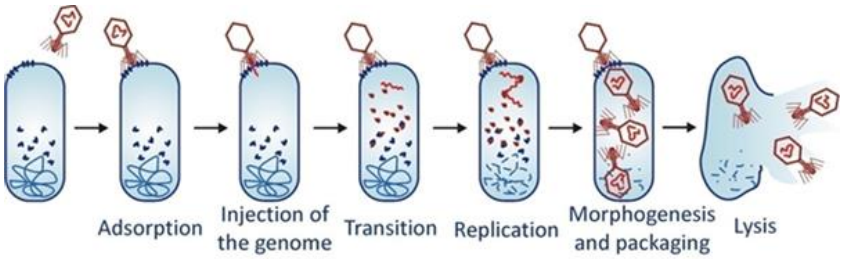

Figure 2: The lytic infection cycle of bacteriophages. The lytic cycle starts with absorption of the phage to the host cell surface. After transition of the host metabolism the phage genome is replicated and new phage particles are assembled. Finally these new phage particles are released by lysis of the host cell.

The C*audovirales* comprise three main bacteriophage families: the *Myoviridae*, containing long contractile tails, the *Podoviridae*, with short tails, and the *Siphoviridae*, with long, flexible tails (Maniloff & Ackermann, 1998). Each of these families are subdivided in several subfamilies and genera, of which some contain *Pseudomonas* infecting bacteriophages. Within one genus variation occurs, especially in the genes responsible for host-metabolism transition (early genes) and the tail fibers, which provide host specificity and are therefore crucial during co-evolution with the host (Ceyssens *et al.*, 2011). This variation is mediated by 'horizontal gene transfer', especially between related phages (Hendrix, 2002; Cornelissen *et al.*, 2012). The co-evolution between phage-resistant bacteria and counter-resistant phages also continues by the contribution of other mechanisms. For example the CRISPR-Cas system targets foreign DNA, like phage DNA, inside the bacterial cell. Bacteriophages on the other hand can escape the CRISPR-Cas system by acquiring point mutations in the DNA fragment which is recognized by this system. In addition, several bacteriophage anti-CRISPR-Cas proteins have been identified. In *Pseudomonas* infecting Mu-like phages for example, five protein families that inhibit type I-F CRISPR-Cas systems and four protein families that inhibit type I-E systems were identified (Maxwell, 2016). Another bacterial defense mechanism is a restriction-modification system that degrades unmethylated, foreign DNA. Bacteriophages can adapt to this system by incorporating modified bases in their DNA, making it unrecognizable for these restriction modification systems (Koskella & Brockhurst, 2014).

1.2.1. PhiKZ giant phages

PhiKZ is a giant, *Pseudomonas*-infecting phage, purified from sewage in Alma Ata, Kazachstan. It is the representative of the *Phikzlike-virus*, a set of giant phages within the family of the *Myoviridae* (Krylov *et al.*, 2007). The phiKZ dsDNA genome is linear, circularly permutated and terminally redundant. It is one of the largest bacteriophage genomes entirely sequenced today, with 280,334 basepairs, comprising of 369 predicted ORFs, which vary in size from 50 to 2237 amino acid residues. Apart from some enzymes involved in nucleotide metabolism, the phiKZ genome encodes no proteins which are homologous to *Pseudomonas aeruginosa* proteins (Mesyanzhinov *et al.*, 2002;

Ceyssens *et al.*, 2014). Furthermore, phiKZ is closely related only to the *Pseudomonas chlororaphis* phage 201phi2-1 (167 similar proteins) and to a lesser extend to EL (66 similar proteins) (Hertveldt *et al.*, 2005). These low DNA and protein homologies to most other bacteriophages point out that phiKZ bacteriophages form an evolutionarily distinct branch within the family of the *Myoviridae*.

The 145 nm diameter icosahedral head of the phiKZ virion is attached to a 200 nm long, contractile tail, followed by a large flat baseplate (see Figure 3A, 3B and 3C) (Fokine *et al.*, 2007). The bacteriophage head contains no less than 50 different structural proteins. At least 19 of these are cleaved during the maturation of the prohead, forming a major morphogenetic step in the assembly of the phiKZ capsid. Six of these structural capsid proteins are present in high abundance. Moreover, they are believed to be major components of the phiKZ inner body (IB), which is a conserved (e.g. 201phi2-1 and EL) and highly ordered, cylindrical protein complex inside the phage head (see Figure 3D and 3E) (Thomas *et al.*, 2012, Krylov *et al.*, 1984). Although the structure of the immense phiKZ IB is solved, the function, composition and role in infection remain elusive (Wu *et al.*, 2012). It was suggested, however, that tight spooling of the phiKZ genome around the IB may reduce the pressure the DNA would otherwise exert on the capsid shell. Another hypothesis claims the IB to be multifunctional, playing roles in DNA packaging, packaged genome structure and DNA ejection. Finally, the phiKZ IB may serve as a reservoir for proteins or enzymes initially injected into the host cell with the genomic DNA and helping in metabolic transition (Thomas *et al.*, 2012). After injection of the phage genome in the host cell the IB is not present in the phage head anymore, supporting the latter hypothesis (Krylov *et al.*, 1984).

In a recent study it was shown that phiKZ is still able to reproduce in the presence of high concentrations of rifampicin, which blocks transcription by bacterial RNA polymerases (RNAP). These results prove that phiKZ is not dependent on host transcription machinery to form progeny. A set of four β/β'-like virion-associated proteins (gp178, gp80, gp149 and gp180), that constitute a viral RNAP (vRNAP), were identified by bioinformatical analysis of the phiKZ genome, showing homology to the bacterial β and β' RNAP subunits (Ceyssens *et al.*, 2014; Thomas *et al.*, 2012; Lecoutere *et al.*, 2007). In contrast, a set of four additional proteins (gp123, gp71/73, gp74 and gp55) was identified as the product of early genes and therefore they constitute a non-viral RNAP (nvRNAP) (Thomas *et al.*, 2012). Furthermore, these proteins show similarities with bacterial β/β' RNAP subunits. Both RNAseq and primer extension experiments identified 28 short, conserved and AT-rich motifs as promotor sequences for vRNAP, which initiates transcription after injection into the host cell. This led to the hypothesis that early phage transcription does not require protein synthesis, as the injected rifampicin-resistant RNAP is sufficient for expression of the early genes. However, protein translation is needed for expression of middle and late genes, as was shown by inactivation of translation at

several time points post infection. It was suggested that the second set of nvRNAP proteins is responsible for transcription in these phases. A final peculiar feature of phiKZ infection lays in the abundance of phage mRNA in the host cell during infection. RNA sequencing (RNA seq.) experiments have shown that, comparing transcripts 10 and 35 minutes post infection, the accumulation of phage transcripts is associated with a decrease in abundance of bacterial transcripts. Remarkably, halfway through the phage infection cycle, no more than 1.5% of total, cellular mRNA is of bacterial origin (Ceyssens *et al.*, 2014).

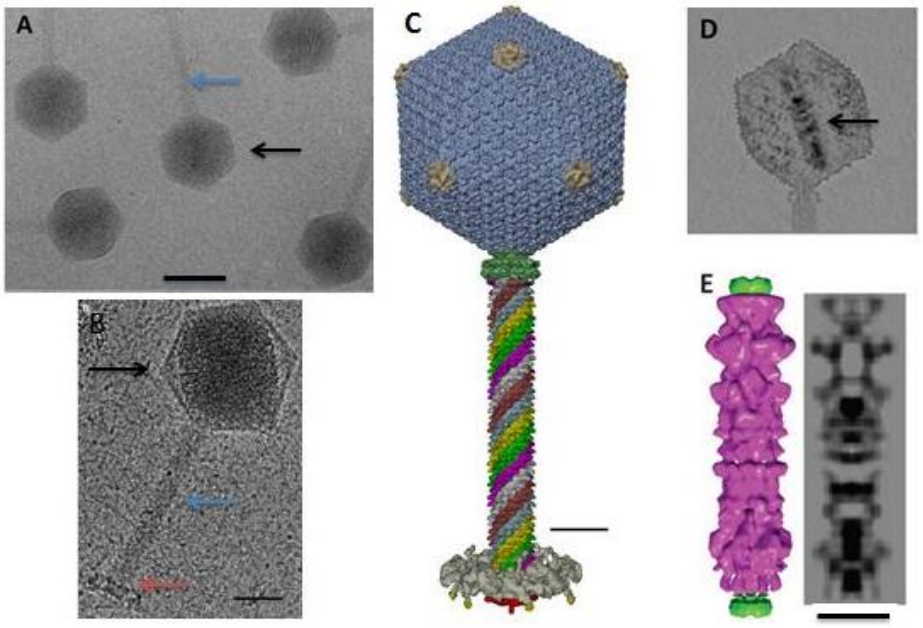

Figure 3: Cryo-EM images and three dimensional models of the phiKZ virion and inner body. A, B: The icosahedral heads and long tails are marked by black and blue arrows, respectively. The large, flat baseplate is marked by a red arrow. Scale bars correspond to 100 nm (A) and 50 nm (B). C: The major capsid protein is shown in blue, the six helices of the tail sheet are shown in white, brown, blue, yellow, green, and magenta and the baseplate is shown in grey. The scale bar corresponds to 30 nm. D: The immense Inner body forms a rod-shaped complex inside the phage head and is tilted relative to the portal axis. E: Low resolution structure of the inner body, in surface representation (magenta, left) and central gray-scale section (right) (adapted from Wu *et al.*, 2012 & Fokine *et al.*, 2007).

1.2.2. Bacteriophage-host protein-protein interactions

A crucial part of an efficient infection of the host cell by bacteriophages is the interaction between bacteriophage and bacterial proteins. The phage-encoded effector proteins either inhibit, activate or redirect the functionality of their host targets. From a bacteriophage point of view, these interactions serve to escape the multitude of bacterial defense mechanisms or to induce a transition of the host metabolism in order to ensure an efficient infection cycle. Primarily, early bacteriophage gene products affect a range of molecular pathways in the host cell, many of which are non-essential. Unfortunately, most of the (predicted) bacteriophage early proteins have no identified functionality yet, and therefore more research towards the biological elucidation of these early proteins is necessary. Understanding the molecular interactions between bacteriophage and host proteins may

unfold new antibacterial strategies and biotechnological applications (Roucourt & Lavigne, 2009). Especially when the phage effector proteins target regulatory hubs of the host bacterium, they become interesting for drug discovery and design. Hubs are proteins that play key roles in pathways. These key proteins are likely to interact with a multitude of other proteins involved in several pathways. All of these interactions can be depicted in a protein-protein interaction network. In these networks, proteins are presented as nodes whereas interactions are visualized by the internodal links (Walhout & Vidal, 2001). To date, the *Pseudomonas aeruginosa* PPI network is still far from complete, but several important hubs towards drug discovery have already been mapped, as illustrated in Figure 4. For example, the upper left and right modules and the bottom right module contain members of the *rps* and *rpl* gene family, which encode ribosomal proteins or play important roles in ribosomal assembly. Furthermore, the *Rpo* genes in the lower right module play major roles in transcription, as they encode RNA polymerase subunits, whereas *NusA* in the same module coordinates transcription termination (Zhang *et al.*, 2012).

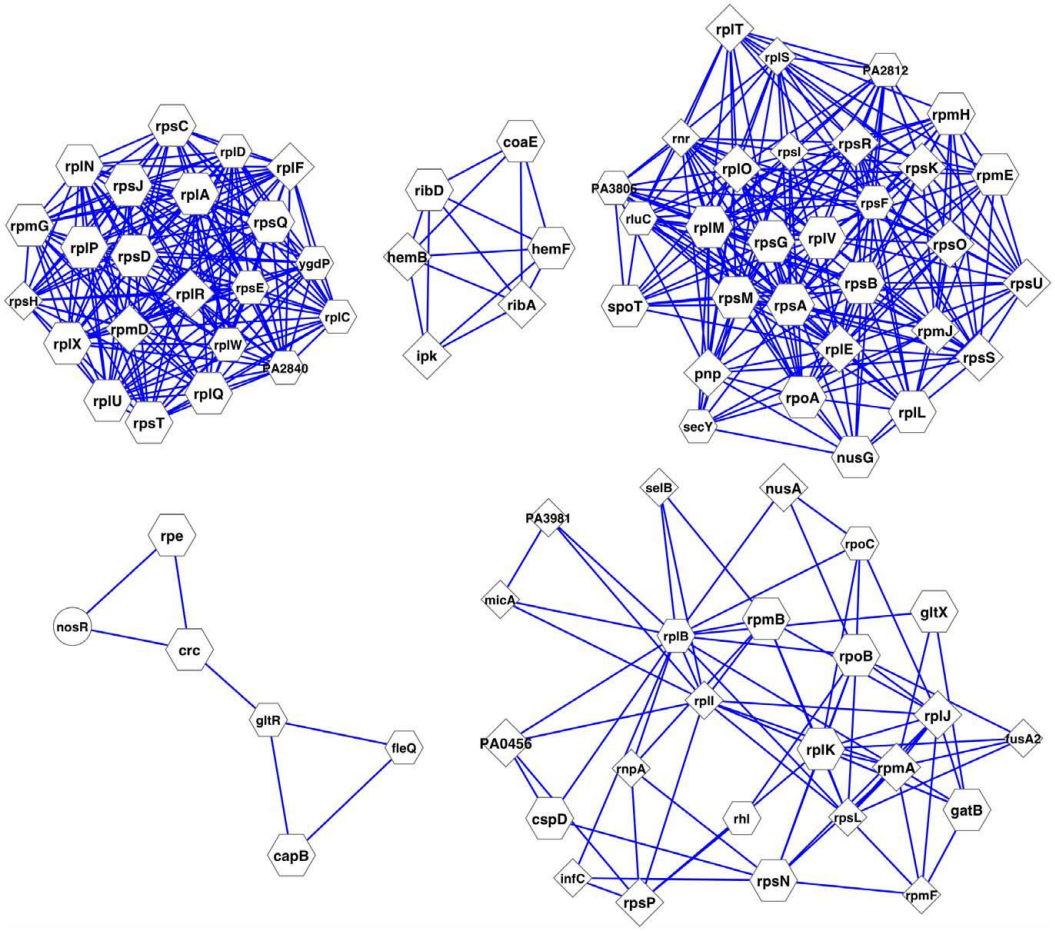

Figure 4: Five crucial modules in the *P. aeruginosa* interactome, containing potential drug targets. Large nodes represent essential proteins whereas small nodes represent non-essential proteins. In this figure triangular nodes depict hubs and hexagonal nodes depict hubs and bottleneck proteins in the Pseudomonas aeruginosa network. Most of the proteins in these modules are hubs, as indicated by their essentiality (adapted from Zhang *et al.*, 2012).

In this dissertation the remarkable interaction between a phage protein and the *P. aeruginosa* RNA degradosome is characterized (see 1.4). Therefore some general examples of phage-host protein-protein interactions also influencing RNA or DNA degradation or which show similarities to the interaction model and structures investigated in this dissertation are discussed in the following paragraphs.

The first example handles a bacteriophage T7-encoded protein kinase that targets the same interaction site as the protein studied in this dissertation. This T7 protein kinase is believed to stabilize T7 mRNAs during phage infection. T7 mRNAs are transcribed by the T7 RNA polymerase (RNAP) which is encoded by early T7 genes and performs transcription of the late bacteriophage genes. Amongst others, these genes encode proteins responsible for DNA replication and virion morphogenesis and replication. T7 RNAP mediates transcription more efficiently compared to bacterial RNAP, thereby outpacing the translating ribosomes (Iost *et al.*, 1992). This way T7 RNAP generates a long stretch of naked mRNA in its wake, which is particularly susceptible for degradation by the RNA degradosome. To compensate for this desynchronization of transcription and translation, a bacteriophage-encoded protein kinase (PK), which is a product of gene 0.7, stabilizes these mRNAs. It was suggested that these PKs do so by phosphorylation of both the C-terminal scaffolding domain of RNase E and RhIB, a degradosome associated RNA helicase (see 1.3). As the scaffolding domain of RNase E contains RNA binding domains (RBD), phosphorylation could interfere with RNA binding. However not all mRNAs are stabilized by this T7 PK. It was shown that 9S RNAs, for example, are still cleaved by RNase E when the T7 PK is expressed, suggesting an induced change of specificity of the RNase E scaffolding domain when phosphorylated by the T7 PK. The exact mechanism of mRNA stabilization by this T7 PK remains unknown to date (Marchand *et al.*, 2001).

The following set of examples all comprise phage encoded proteins that belong to a structural group called the DNA mimicry. Members of this group mimic double stranded DNA to bind their targets. Although structurally diverse, these proteins share common characteristics, such as side-chain carboxylates of glutamates and aspartates which are positioned in a way that they resemble the charge pattern of a DNA phosphate backbone (Putnam & Tainer, 2005). In this dissertation a similar hypothesis was formulated for the protein studied, based on preliminary structural data. The first phage-encoded member of the DNA mimicry discovered is Ugi, which is encoded by the *Bacillus subtilis* infecting phage phiPBS1/PBS2. Ugi efficiently inhibits the host uracil-DNA glycosylase (UDG) to achieve stable substitution of thymine by uracil in the PBS1/PBS2 ds genome. UDG plays an important role in the uracil mediated base-excision repair pathway. In particular, UDG removes Uracil residues from DNA (Lindahl *et al.*, 1977). These residues are one of the most frequent lesions in genomic DNA and are genotoxic. As its genome contains many uracil residues,

bacteriophage PBS1/PBS2 protects its DNA by encoding the B-DNA mimicking protein Ugi. This protein irreversibly binds UDG and shuts down the base-excision repair pathway by mimicking the negatively charged DNA sugar backbone (Putnam *et al.*, 1999). Another very similar inhibitor of the *B. subtilis* uracil-DNA glycosylase is the phi29 phage encoded protein p56, which also mimics the DNA sugar backbone (Baños-Sanz *et al.*, 2013).

The best representative of the DNA mimicry, however, is Ocr from phage T7. Ocr protects T7 genomic DNA, which contains unmethylated adenine residues, by inhibition of the type I restriction modification enzymes of the host. These restriction modification enzymes form a host defense mechanism against foreign DNA. Therefore Ocr is functionally similar to Ugi, which protects the PBS2 genomic DNA from the host Uracil Glycosylase. The 13 kDa Ocr monomer forms dimers in solution and has large negatively charged patches on its surface (Atanasiu *et al.*, 2001). The crystal structure of Ocr has revealed this protein's capability of mimicking approximately 20 base pairs of B-form DNA in order to hijack DNA binding sites of the type I restriction enzymes. The distribution of carboxyl groups of glutamates and aspartates on the dimer surface mimic the distribution of phosphate groups in B-DNA (see Figure 5). By binding and blocking the DNA binding sites on type I restriction enzymes, Ocr efficiently prevents cleavage of the T7 genome after infection (Walkinshaw *et al.*, 2002). A final example of DNA mimicking bacteriophage-encoded protein is λ-Gam, which inhibits the *E. coli* RecBCD machinery. Amongst other functions, RecBCD is responsible for the digestion of linear viral DNA during virus replication. Gam has been proven to bind RecBCD and thereby inhibit its helicase and nuclease activities. The shape and dimensions of Gam resemble Ocr of bacteriophage T7, and its surface is rich in acidic residues. Although the DNA mimicking traits are less obvious from the crystal structure of Gam, it was hypothesized that Gam could mimic the charges and shape of duplex DNA (Court *et al.*, 2007).

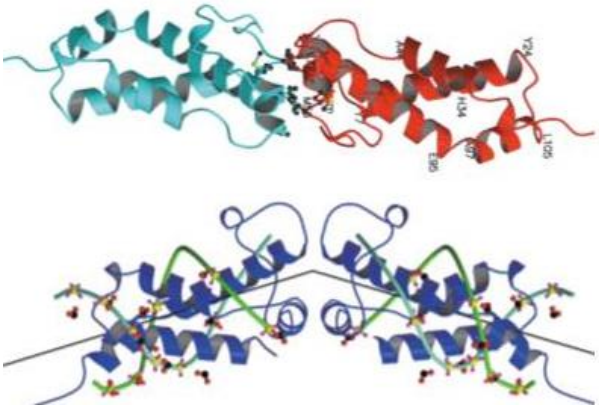

Figure 5: Crystal structure of Ocr and superposition of two B-DNA molecules on the Ocr dimer. Ocr forms a long dimer with four α helices per monomer (top). The phosphate groups of two 12 bp B-DNA duplexes were fitted onto 12 carboxyl groups of Ocr (bottom, adapted from Walkinshaw *et al.*, 2002).

Although phiKZ is a member of the giant phages and has many ORFs, few protein-protein interactions have been characterized so far. In this thesis the unique interaction between a phiKZ encoded protein and the *P. aeruginosa* RNA degradosome will be elucidated both functionally and structurally.

1.3. The RNA Degradosome, a multicomponent regulatory hub of post-transcriptional gene regulation

RNA turnover plays a major role in gene regulation and expression. Compared to rRNAs and tRNAs, mRNAs have limited and adjustable lifetimes. Their stability is, amongst others, dependent on environmental factors and growth phase (Dressaire *et al.*, 2013). mRNA decay is best studied in the Gram-negative *E. coli*, where turnover starts with the conversion of the 5' triphosphate end to a monophosphate by RppH (RNA pyrophosphohydrolase). Subsequently, an endoribonuclease cleaves the mRNA and hereby determines the rate of mRNA turnover. Then a 3'-5' exoribonuclease degrades the cleaved RNA to 2-4 nucleotide fragments, which are further reduced by the essential enzyme oligoribonuclease to form single nucleotides (Górna *et al.*, 2012). The main components responsible for these processes form a large multisubunit complex, the RNA degradosome (Górna *et al.*, 2010). Although the composition of the RNA degradosome is dependent upon growth phase and environmental conditions, the core complex comprises RNase E, a hydrolytic endonuclease, PNPase, a phosphorolytic exoribonuclease, RhIB, an ATP dependent helicase and a glycolytic enzyme, enolase (see Figure 6) (Górna *et al.,* 2012; Vanzo *et al.*, 1998; Carpousis, 2007). All components of this complex cooperate with each other during RNA turnover (Bandyra *et al.*, 2013).

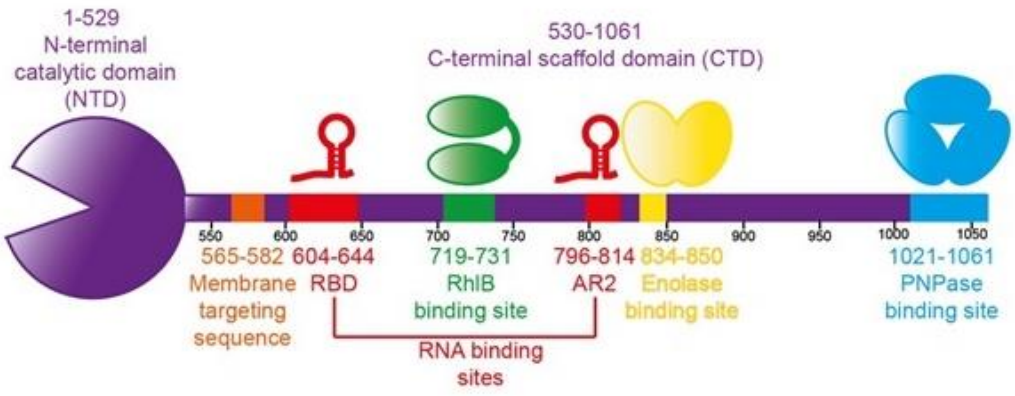

Figure 6: Schematic representation of the *E. coli* RNA degradosome. The N-terminal domain of RNase E is the catalytic domain, responsible for 5' degradation of the RNA substrate. The C-terminal domain of RNase E constitutes a structural scaffold for the assembly of the RNA degradosome, with the RNA helicase RhIB in green, the enolase in yellow and the exoribonuclease PNPase in blue. Binding RNA species are depicted as red hairpins (adapted from Bandyra *et al.*, 2013).

The RNA degradosome provides cells with a selective advantage, even though it is not essential for cell survival and cell proliferation (Vanzo *et al.*, 1998). Furthermore, the RNA degradosome composition is highly variable amongst bacteria and many degradosome like assemblies have been predicted in ϒ-proteobacteria. In *Pseudomonas syringae* for example, the degradosome contains RNase E, the RNA helicase RhIE and RNase R (Purusharth *et al.*, 2005). So far, the molecular complex of the *P. aeruginosa* RNA degradosome has not been elucidated. In the next paragraph the components of the *E. coli* RNA degradosome are briefly discussed.

1.3.1. Components and Function of the RNA degradosome

The main component in the RNA degradosome is the endoribonuclease RNase E. An N-terminal catalytic domain (NTD) and a C-terminal scaffold domain (CTD), which serves as a framework for assembly of all the components of the RNA degradosome, constitute a functional RNase E (see Figure 6). The major role of the catalytic NTD is cleavage of mRNA. However, the NTD of RNase E also stabilizes a homotetrameric complex of RNase E in a functional membrane bound RNA degradosome in *E. coli* (see Figure 8) (see 1.3.2). Crystal structures of the NTD of the *E. coli* RNase E distinguish a small domain and a large domain. The large domain contains two RNase H-like domains, a DNaseI-like domain, a S1-domain and a sensory domain (Callaghan *et al.*, 2005). The DNaseI-like domains interact with each other to form RNase E dimers. The interaction sites are stabilized by the Zn-link, which is a Zn ion covalently bound to cysteine residues. These RNase E dimers interact with one another to form a 'dimer of dimers', or an RNase E tetramer (see Figure 8) (Górna *et al.*, 2012). As the CTD of RNase E is natively unstructured, no crystal structure is available. Furthermore, this scaffold domain has a non-conserved amino acid sequence, enriched in basic residues. Although the CTD of RNase E is largely unstructured, some segments have a stable secondary structure and are involved in membrane localization as well as the interaction with enolase and PNPase. Finally, the scaffold domain contains two RNA binding sites RBD/AR1 and AR2, which are especially important in this dissertation. Both of these RNA binding sites are rich in arginine residues and are believed to form a coiled coil structure (Callaghan *et al.*, 2004).

Although the cleavage specificity of RNase E remains to be elucidated, it has been shown that single stranded RNA is preferably cleaved (Kaberdin, 2003). So far, two models of substrate recognition by RNase E have been elucidated. In the 5' sensing model, a primary 5' triphosphorylated RNA is dephosphorylated to a 5' monophosphorylated RNA by RppH, which is then recognized by the 5' sensor domain on the catalytic NTD of RNase E (Deana *et al.*, 2008, Garrey *et al.*, 2009). In the second mode, i.e. the 'direct/internal entry' mode, the secondary structure of the ribosome-free RNA determines cleavage, without a 5' recognition step. It was proposed that the C-terminal domain of

RNase E as well as its degradosome partners play a major role in RNA substrate presentation to the catalytic domain. Both AR2 and RBD on the CTD mediate the interaction between substrate and RNase E (see Figure 6) (Leroy *et al.*, 2002; Garrey *et al.*, 2009). However, the 5' end-dependent and independent pathways are not necessarily exclusive and may cooperate during RNA degradation. For example, the CTD of RNase E could present structured substrates to the catalytic domain, which recognizes the 5' end. The RNA degradosome is not only involved in mRNA decay but also in maturation of rRNA and tRNA. Although the RNA degradosome is believed to be non-essential for cell survival, RNase E mutants show a loss of viability. However, it is not clear whether this loss of viability is due to defective mRNA decay or due to impairment of rRNA and tRNA processing (Ow & Kushner, 2002; Carpousis, 2007). Since these last two maturation pathways are of less importance for this dissertation, they will not be discussed in detail.

The second subunit of the RNA degradosome is PNPase, which is a conserved 3' exoribonuclease. PNPase degrades ssRNA and releases nucleotides from the 3' end in a processive 3' to 5' degradation reaction. To cleave phosphodiester bonds, PNPase uses phosphate molecules during a phosphorylation reaction. The activity of PNPase is thus regulated by the availability of free phosphates in the cell. PNPase assembles into a homotrimer *in vivo*, with four domains per protomer. Two PH domains form the catalytic site which is responsible for polynucleotide cleavage and contains a Mg^{2+} ion (Symmons *et al.*, 2002). In addition, the PNPase protomer contains two RNA binding sites, KH and S1. The PNPase crystal structure revealed a ring-shaped hexameric conformation of the PH domains, forming a central channel of catalytic domains. Also, the KH and S1 domains are on the same face of the ring. As the active PNPase adopts a homotrimeric conformation it could bind three C-terminal RNase E scaffold domains, forming a 'closed complex' of three RNase E tetramers and four PNPases. However, another hypothesis stipulates that not all RNase E interaction sites on PNPase are occupied, yielding an 'open complex', where PNPase trimers form links between the CTDs of RNase E tetramers (see 1.3.2) (Marcaida *et al.*, 2006; Górna *et al.*, 2012).

A third component of the *E. coli* RNA degradosome is RhIB, an ATP-dependent RNA helicase, which is bound to the CTD of RNase E (see Figure 6). RhIB is a member of the DEAD-box helicases, which contain the D-E-A-D motif for ATP binding and hydrolysis (Cordin *et al.*, 2006). Binding of ATP triggers conformational changes and thereby creates a catalytic site for ATP hydrolysis, between two interconnected, RecA-like domains of RhIB. In addition, an RNA binding site is formed on each RhIB subunit, distal to the ATP binding site. *In vitro*, DEAD-box helicases have an RNA-dependent ATPase activity, whereas they also have an ATPase-dependent RNA unwinding activity. It was shown that ATP hydrolysis leads to additional structural changes, which probably infer the unwinding of the RNA substrate (Carpousis, 2007; Hardwick & Luisi, 2012). Other experiments have shown that ATP binding

is needed for unwinding RNA by DEAD-box helicases, whereas ATP hydrolysis is necessary for the release of ssRNA (Linder & Jankowsky, 2011). In addition to the RNA binding sites on each subunit, RhlB has a short basic C-terminal unstructured extension which binds RNA in an nonspecific way. RhlB has an unwinding capacity of less than two turns, which is slightly enhanced by binding of RhlB to RNase E, in between the two RNA binding sites of the RNase E scaffold domain (see Figure 7) (Chandran *et al.*, 2007).The protein-protein interactions between RhlB and RNase E stimulate the ATPase activity of the RhlB catalytic domain. Furthermore, the AR2 and RBD sites on the RNase E CTD participate in the RNA unwinding reaction. RhlB unwinds hairpins from the 3' end of RNA and thereby generates ssRNA. This is crucial for the PNPase mediated degradation of structured RNA by the degradosome (see Figure 7) (Khemici & Carpousis, 2003). Finally, it was suggested that the association of RhlB with the rest of the RNA degradosome determines the specificity of RNA decay. RhlB directly interacts with PNPase when RNase E is absent, further supporting the above hypothesis and proposing a mechanism of non-specific RNA decay (Carpousis, 2007; Kaberdin & Bläsi, 2013).

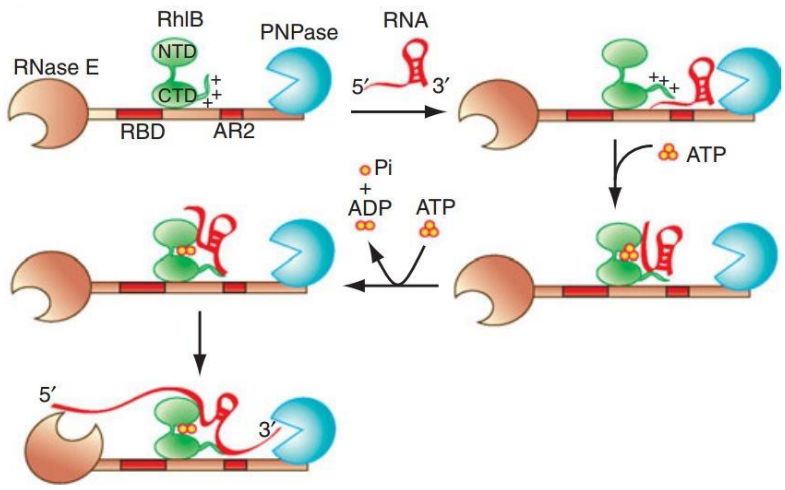

Figure 7: Coordination of structured RNA degradation through cooperation between the RNA helicase RhlB, the catalytic NTD of RNase E and the exoribonuclease PNPase of the RNA degradosome. RNA binds to RNase E at the RBD or AR2 sites or both (not shown). Binding and Hydrolysis of ATP by RhlB mediates the interaction of RNA with the RecA-like domains of RhlB during unwinding. The adjacent PNPase then cleaves the RNA through phosphorolysis. The catalytic NTD of RNase E cleaves the 5' end by hydrolysis (adapted from Górna *et al.*, 2012).

A final member of the *E. coli* degradosome is enolase, a glycolytic enzyme. This homodimeric enzyme is a phosphopyruvate dehydratase which catalyzes phosphoenolpyruvate formation from 2-phosphoglycerate (Kühnel & Luisi, 2001). So far, the exact role of enolase as a RNA degradosome component hasn't been determined. However, it was demonstrated that enolase plays a role in the stability of several mRNAs, especially those involved in pathways for energy generation (Bernstein *et al.*, 2004; Morita *et al.*, 2004). These observations indicate that enolase serves as a sensor for the energy levels of the cell (Carpousis, 2007).

1.3.2. A membrane localized quaternary RNA degradosome complex

As mentioned in the previous paragraph, the catalytic domain of RNase E stabilizes a homotetramer, which is organized as a dimer of dimers. In this conformation, the catalytic domains are connected through organometallic bonds with shared zinc ions. From the catalytic core, four non-catalytic and natively unstructured regions extend (see Figure 8). Each of these non-catalytic regions could interact with a RhIB monomer, a dimer of enolase and a PNPase trimer forming a discrete complex of 2000 kDa (Carpousis, 2007). Furthermore, in *E. coli* the RNase E is tethered to the cell membrane by an amphipathic α-helix of 21 residues, segment A, localized 30 to 45 residues to the C-terminal end of the catalytic domain (see Figure 8). Bioinformatics analyses have demonstrated that this amphipathic helix is conserved in β- and ϒ-proteobacteria (Khemici *et al.*, 2008).

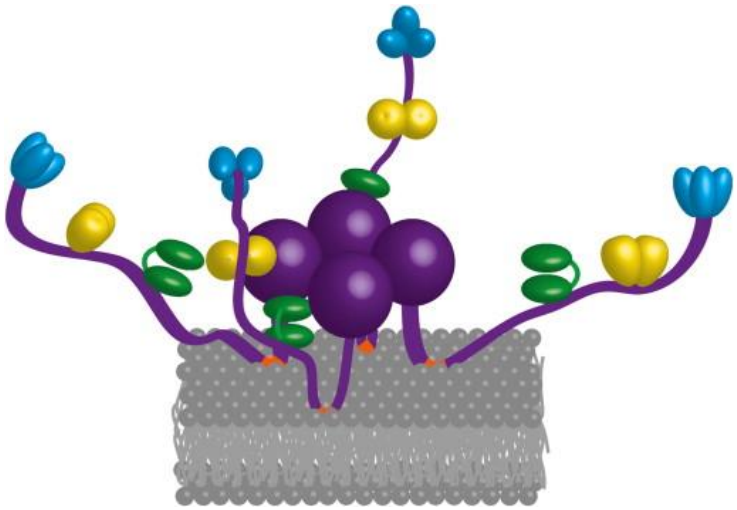

Figure 8: Quaternary structure and membrane localisation of the *E. coli* RNA degradosome. Schematic representation of the association of a RNase E tetramer with the inner side of the cytoplasmic membrane. Four amphipathic α-helices (orange) are embedded in the lipid bilayer (gray). Each purple sphere is an RNase E catalytic domain. Green, Yellow and blue are the RhIB bilobal monomer, the enolase dimer and the PNPase trimer respectively (Bandyra *et al.*, 2013).

In general, the subcellular compartmentalization of enzymes often influences the access to substrates. It was demonstrated that membrane association of RNase E is required for normal growth, which indicates that it impacts RNase E activity (Khemici *et al.*, 2008). However, the exact mechanism and purpose of degradosome assembly and membrane localization are not well understood. In addition, no unambiguous molecular weight has been determined for the RNA degradosome so far, which suggests that the complex is heterogeneous and that an equilibrium between different size complexes might exist. For example, if each PNPase trimer manages to interact with three non-catalytic RNase E domains, a 4000 kDa complex would be formed, which is about twice as large as an 80S ribosome. In the latter case, all possible protein-protein interactions would be filled, forming the 'closed complex', as mentioned in the previous section (see Figure 9) (Carpousis, 2007; Górna *et al.*, 2012). In addition, *in vivo* fluorescence microscopy experiments

suggest that the RNA degradosome co-localizes in a filamentous structure, spiraling along the interior cell surface as an 'open network' (see Figure 9). In the corresponding model not all PNPase protomer domains are bound to the RNase E scaffold domain. This filamentous hypothesis has been very controversial, partly because the researchers suggested that the RNA degradosome would be associated with the bacterial cytoskeleton (Taghbalout & Rothfield, 2007, 2008). However, these data do not prove that the RNA degradosome polymerizes. Furthermore, the possibility that discrete RNA degradosome patches follow a spiraling track on the inner membrane without polymerization is equally plausible (Górna *et al.*, 2012).

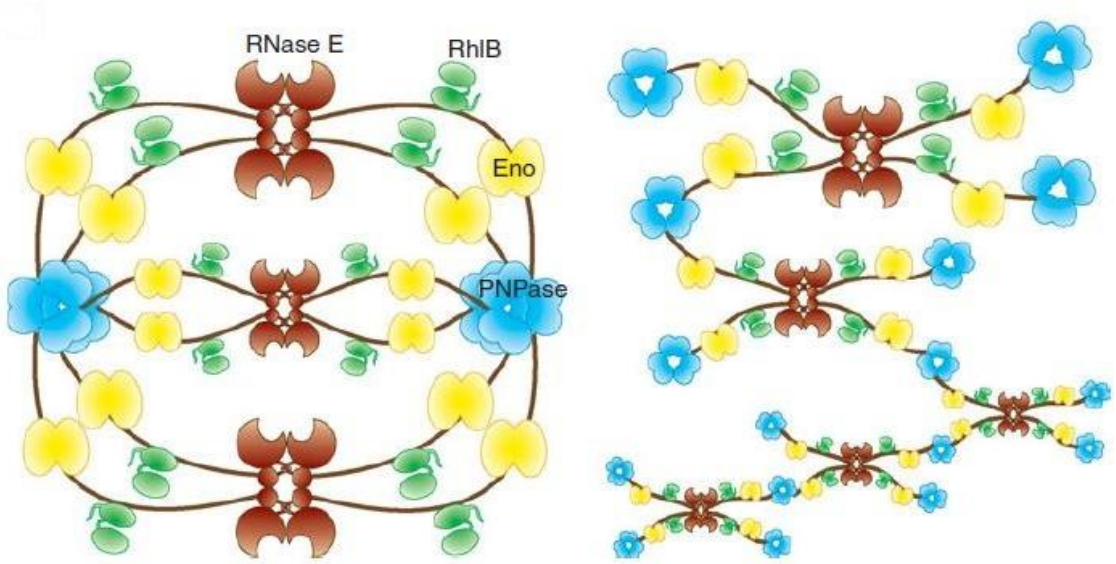

Figure 9: RNA degradosome assembly models. Left: The RNA degradosome assembles into a 'closed complex', with all potential binding sites satisfied. In this model a minimal RNA degradosome comprises three RNase E tetramers and four PNPase trimers. Right: The RNA degradosome assembles in an 'open network'. PNPase trimers link RNase E tetramers into an extensive network. Brown, yellow, blue and green are RNase E tetramers, enolase dimers, PNPase trimers and RhlB monomers respectively (adapted from Górna *et al.*, 2012).

1.3.3. RNA decay: A complex and strictly regulated process

Both the specificity and activity of the RNA degradosome are strongly regulated. As explained in the previous paragraphs, the secondary structure of RNA plays an important role in the recognition of RNA by the RNase E scaffolding domain. Furthermore, the stem loops in RNA substrates need to be removed by RhlB for the 3' exoribonuclease to truncate the RNA species. Remarkably, RNase E performs auto-regulatory control on its expression by cleaving any excess of RNase E mRNA, *rne*. This mRNA forms a stem-loop in the 5' untranslated region, which is recognized by RNase E (Schuck *et al.*, 2009). In addition, two regulatory factors (RraA and RraB, 'Regulators of RNase activity') have been found to control RNase E activity. These proteins both bind to the C-terminal scaffold domain of RNase E and inhibit its activity upon overexpression, influencing the abundance of several mRNAs either cooperatively or exclusively. RraA occurs as a trimer and binds to both RNA binding sites on

the CTD of RNase E, AR2 and RBD. Moreover, RraA was found to bind the C-terminal tail of RhIB. RraB on the other hand, interacts with a single 33 amino acid stretch on the CTD of RNase E (Gao *et al.*, 2006).

Alternatively, the RNA degradosome activity is directly controlled by ribosomes. It is well known that naked mRNA is more accessible by the RNA degradosome than mRNA coated with ribosomes (Wagner, 2009). Alternatively, the two RNA binding sites on the C-terminal scaffold domain of RNase E and the C-terminal tail of RhIB can bind to 70S ribosomes, diminishing the processing activity of RNase E. Degradation of unstructured RNAs, however, doesn't require binding to the RNA binding sites and remains unaffected. In this model the degradosome 'rests' on ribosomes, rendering it in an inactive state (Tsai *et al.*, 2012).

Small non-coding RNAs (sRNA) are crucial regulators of gene expression through a mechanism which is called riboregulation (Bandyra *et al.*, 2013). These sRNAs are 50 to 300 nucleotides long and function as translational activators or inhibitors by targeting mRNAs through a certain degree of complementarity (De Lay *et al.*, 2013). After binding, translation is inhibited, rapidly followed by transcript destabilization and finally degradation. Hybridization of the sRNA to its target is promoted by Hfq, a ring shaped hexameric protein. Although the mechanism is not very well understood, it is possible that Hfq introduces changes in the sRNA secondary structure or guides the sRNA into close proximity to its target (Vogel & Luisi, 2011). Either way, co-immunoprecipitation studies have shown that RNase E and Hfq interact during RNA degradation. However, the defined interaction site contains both the RhIB binding site and the AR2 RNA binding site, and thus so far it is not clear whether the interaction between Hfq and RNase E is mediated by sRNA or not (Ikeda *et al.*, 2011).

Since the RNA degradosome is a regulatory hub of RNA degradation one would expect bacteriophages have developed several strategies to protect their mRNA by altering the activity of this key machinery. However, only a few such mechanisms have been elucidated so far. The most important example is discussed in section 1.2.2. In this example coliphage T7 encodes a protein, gp 0.7, of which the N-terminal part inhibits the 'direct entry' degradation pathway by phosphorylation of the CTD of RNase E (Marchand *et al.*, 2008). This mechanism ensures only catalytic amounts of gp0.7 are sufficient to shut down all cellular RNase E (Mackie, 2013).

In addition, coliphage T4 has been found to encode a factor that changes the specificity of RNase E, thereby protecting its own mRNA. Very little is known about this factor or the way it interacts with RNase E (Ueno & Yonesaki, 2001). In this dissertation the recently discovered interaction between a phiKZ encoded protein and the *P. aeruginosa* RNA degradosome is further elucidated in a functional

and biological way. In the next section, an introduction will be given on the discovery of this protein as well as on previous research.

1.4. Gp37 hijacks the RNA degradosome in order to protect its own mRNA.

To assess the degradosome composition in *P. aeruginosa* and the changes in response to environmental factors, i.e. phage infection in this case, a pull down assay of RNase E was performed, followed by mass spectrometry analysis. For all tested P. *aeruginosa* strains PNPase was found to interact with RNase E. Furthermore, depending on the strain the DEAD-box proteins RhIE, DeaD or RhIB, or a combination thereof, were co-purified as well. However, no enolase was detected. Following infection of *P. aeruginosa* with giant phage phiKZ, a single phage protein, gp37, was found to interact with RNase E. Remarkably, this phage protein has no sequence homology with any known protein in the databases today. This indicates that phiKZ bacteriophages branched of early during evolution. Subsequently, it has been shown that phiKZ expresses Gp37 in order to alter the host degradosome activity and ultimately protect the newly transcribed phage mRNA (Van den Bossche *et al.*, in submission). Indeed, gp37 is highly transcribed during early infection (after 10 minutes) and belongs to the 10% most abundantly expressed genes of phiKZ (Ceyssens *et al.*, 2014).

1.4.1. Structural elucidation of gp37

Gp37 has a mass of 31.7 kDa and forms dimers in solution. To elucidate the molecular structure, gp37 was crystalized and the crystal structure was solved to a resolution of 2.28 Å. Two gp37 protomers were identified per asymmetric unit, forming an open clamp-like homodimer, resembling a partially opened scroll (see Figure 10) (Van den Bossche *et al.*, in submission). The C-termini of both monomers interact to form the dimer interface. Furthermore, gp37 has a unique fold, showing no significant similarities to other known protein crystal structures.

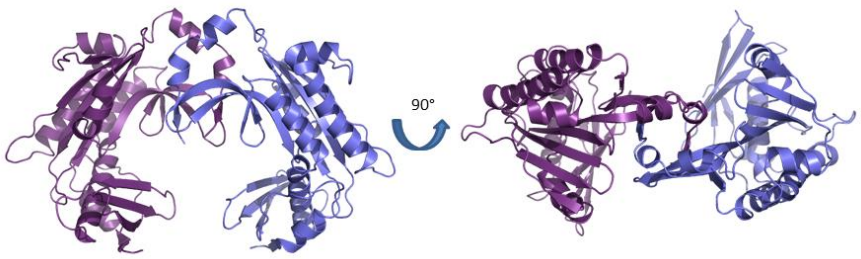

Figure 10: Crystal structure of a gp37 dimer. Predicted interaction sites with the target cluster in the central groove and the outer edge of the dimer.

Since no similar folds were found, potential interaction sites with the target were predicted with Metapocket (Huang, 2009). Most candidate amino acids were aligning along the central grooved concave face and the outer edges of the dimer (see 4.1.3) (Van den Bossche, 2015).

1.4.2. Gp37 interacts with the RNA binding sites of RNase E

Extensive bacterial two-hybrid and subsequent mobility shift assays were used to identify the RNase E interaction sites for gp37. These analyses demonstrated that gp37 binds to a 20 amino acid stretch (756-775) of the C-terminal scaffold domain of RNase E. In addition, a second 25 amino acid stretch (583-607) was found to interact with gp37, albeit with a lower affinity. Both interactions are direct protein-protein interactions and therefore gp37 was renamed to 'Degradosome interacting protein' or 'Dip' (Van den Bossche *et al.*, in submission). Moreover, Dip is the first identified viral protein to inhibit degradosome activity via a direct interaction. Therefore, Dip can be regarded as a functional homologue of the bacterial proteins RraA and RraB, which bind specific regions of the CTD of RNase E and inhibit its activity in *E. coli* (see 1.3.3) (Górna *et al.*, 2010).

Both interaction sites on the RNase E scaffold domain align well to the known RNA binding sites of the C-terminal RNase E scaffold domain in *E. coli* (RBD and AR2) and are rich in arginine residues (see 1.3.1). Additional pull down assays have demonstrated that Dip interacts with both *E. coli* and *Caulobacter crescentus* RNase E, which suggests that the target sites of Dip are conserved in RNase E from distant bacterial species. Furthermore, Dip was shown to compete with and even displace RNA from the AR2 RNA binding site on RNase E. These results suggest that Dip targets both conserved RNA binding sites on the CTD of RNase E, which is further investigated in this thesis. Also, Dip inhibits the RNA degradosome activity towards long RNAs *in vitro*, independent of the cleavage pathway used ('direct entry' or '5' dependent' pathway). When tested for cleavage of a short RNA fragment (27-mer), the inhibitory effect of Dip was less pronounced both for the *E coli* and *P. aeruginosa* RNase E. The current hypothesis is that Dip inhibits the processing of long structured RNAs by binding to the RNA binding sites on RNase E, whereas small RNA substrates are directly degraded by the catalytic domain of RNase E (Van den Bossche *et al.*, in submission). This way, Dip would act somewhat similar to bacteriophage T7, which prevent degradation of its transcripts by phosphorylation of the scaffold domain of RNase E in *E. coli* (Marchand *et al.*, 2001).

In vivo, *P. aeruginosa* cells tend to change morphology from a wild type rod shape to a curled phenotype when Dip is overexpressed. In addition, qRT-PCR experiments demonstrated an increase in RNA stability in the presence of Dip (Van den Bossche *et al.*, in submission). Remarkably, RNA seq. analyses during phiKZ infections in *P. aeruginosa* revealed that 35 minutes after the start of infection 98.5% of non-rRNA and non-tRNA could be mapped to the phiKZ genome. Overall, the cellular RNA

amount increased over fivefold during infection (Ceyssens *et al.*, 2014). One hypothesis states that Dip alters the degradosome specificity towards host RNA in order to protect its own RNA, rather than inhibition of the degradosome activity. Another hypothesis states that the degradosome is regulated timewise rather than by specificity. In this case specific phiKZ proteins could be involved in the decay of host mRNA, and Dip would serve to stabilize the phiKZ mRNA in a subsequent phase of infection. Both gp43 and gp155 of phiKZ, for example, are homologous to members of the RNase R family and could catalyze degradation of host mRNA (Van den Bossche, 2015; Mesyanzhinov *et al.*, 2002; Majorek *et al.*, 2014).

Finally, modelling experiments were initiated to identify the RNase E [756-775] peptide binding site on the Dip surface. The docking program DOT (Robert *et al.*, 2013) was used to screen the Dip surface for optimal target binding. In the lowest energy complex, the 20 amino acids peptide is predicted to bind to a large negatively charged patch on the outer Dip surface. In parallel, Dip was co-crystalized with this 20 amino acid segment. Dip appeared to oligomerize in a ring shaped hexamer, which was observed through crystallographic symmetry (see 4.1.2). Extra electron density was found at the acidic pocket of each Dip monomer in the hexamer, which is in agreement with the best docking model. Based on this observation, we set out in this dissertation to further characterize the interaction between Dip and the RNase E scaffold domain.

2. Research goals and outline

70% of the predicted bacteriophage genes have no known function. This gap between gene prediction and functional annotation, which is still expanding, forms a major opportunity for the discovery of new antibacterial targets and strategies, as well as the development of new biotechnological tools inspired by biomolecular mechanisms. In order to live up to these goals, a fundamental understanding of these mechanisms is crucial. In this dissertation, a very promising phiKZ-based strategy to shut down the *P. aeruginosa* RNA degradosome, i.e. hijacking of the RNA binding sites by Dip, is further elucidated both structurally and functionally. For the structural part of this thesis, the proposed RNase E interaction site on the Dip surface will be examined. Furthermore, the stoichiometry and general shape of Dip interacting with different target constructs will be assessed. Moreover, the initial steps taken towards a high resolution cryo-EM dataset of Dip in complex with its target will be discussed. For the functional part, the persistence of Dip in the cell during later stages of phage infection will be tested. These findings will add to a profound understanding of the role of Dip during phage infection and the mechanism and stoichiometry of the interaction between Dip and its target. Closing this thesis, the gathered knowledge will be extrapolated towards possible applications both therapeutically and as a biotechnological tool for fundamental research.

The results of this work are divided in two main parts, according to the type of research that has been performed. The structural part will be discussed in three closely related sections. In the first section, **''Dip hijacks both RNA binding sites on RNase E via a negatively charged patch on its outer surface"**, the target-interaction site on Dip is determined by structural and bioinformatics analyzes and confirmed by mutagenesis and crystallographic experiments. The molecular weight and stoichiometry of a complex of Dip and the CTD of *P. aeruginosa* are investigated using different techniques in the next section, **"Investigating the interaction model of Dip and the RNA degradosome"**. Finally, in the third section, **''Dip dimers could oligomerize to mimic duplex RNA and hijack the RNA degradosome"**, the solution structure for Dip is compared to the crystal structure. In addition the interaction model of Dip and RNase E is further elucidated. For this SEC-SAXS (Size-exclusion Chromatography Small-angle X-ray scattering) and electron microscopy have been used. The functional part of this dissertation comprises one section. In this section, "**Dip is persistent during phiKZ infection**", polyclonal antibodies against Dip are produced and used in western blot experiments to investigate the persistence of Dip during late bacteriophage infection stages. Finally, general conclusions and future perspectives are summarized and discussed.

3. Materials and methods

3.1. Growth media, Bacterial strains and bacteriophages

3.1.1. Growth media

For *E. coli* and *P. aeruginosa*, standard growth protocols were performed in Lysogeny broth (LB, 1 % (w/v) Bacto tryptone (lab M, Lancashire, UK), 1 % (w/v) NaCl (Acros Organics, Geel, Belgium), 0.5 % (w/v) yeast extract (Lab M)). For solid growth medium 1.5% (w/v) agar (Lab M) was added and for soft agar 0.4% (w/v) or 0.7% (w/v) agar was added. When required, the medium was enriched with 100 µg/ml ampicillin (Sigma Aldrich, St. Louis, MO, US), 30 µg/ml Chloramphenicol (Merck Millipore, Billerica, MA, US), 15 µg/ml tetracyclin (Sigma Aldrich) or 1 mM isopropyl-β-D-1-thiogalactopyranoside (IPTG, Thermo Scientific, Waltham, MA, US).

3.1.2. Bacterial strains and transformations

Four *E. coli* strains were utilized in this dissertation (see Table 1): *E. coli* TOP10 (Life Technologies) and *E. coli* DH5α (Thermo Scientific) were used for vector cloning, *E. coli* BL21 (DE3) (Life Technologies) for heterologous expression of RNase E peptides and *E.coli* BL21 (DE3) pLysS (Life Technologies) for heterologous expression of Dip. Chemical competent cells (rubidium chloride method, stored at -80 °C) were utilized for transformation, which was performed with a heat shock (42°C) during 30 seconds (Hanahan, 1983).

Table 1: Summary of the *E. coli genotypes used in this dissertation.*

***E. coli* strain**	**Genotype**
TOP10	F^- mcrA Δ(mrr-hsdRMS-mcrBC) ϕ80lacZΔM15 ΔlacX74 nupG recA1 araD139 Δ(ara-leu)7697 galE15 galK16 rpsL(Str^R) endA1 λ^-
DH5α	F^- phi80*lac*ZΔM15 Δ(*lac*ZYA-*arg*F) U169 *rec*A1 *end*A1 *hsd*R17 (rk^-, mk^+) *pho*A*sup*E44 λ^- *thi*$^-$1 *gyr*A96 *rel*A1
BL21 (DE3)	F^- ompT gal dcm lon $hsdS_B(r_B^- m_B^-)$ λ(DE3 [lacI lacUV5-T7 gene 1 ind1 sam7 nin5])
BL21 (DE3) pLysS	F^- ompT gal dcm lon $hsdS_B(r_B^- m_B^-)$ λ(DE3) pLysS(cm^R)

All phage infections and manipulations in *P. aeruginosa* were performed in *P. aeruginosa* PAO1 (Stover *et al.*, 2000). All plasmids were electroporated to electro-competent *P. aeruginosa* cells using 1.5 mm gap electroporation cuvettes (Bio-Rad, Hercules, CA, US) and a gene pulser II (Bio-Rad) set at 2.5 kV, 25 µF and 200 Ω (Choi *et al.*, 2006).

3.1.3. Bacteriophages and manipulations

The bacteriophage used in this dissertation, bacteriophage phiKZ, is discussed in '1.2.1 phiKZ giant phages'. Phage amplification was performed in *P. aeruginosa* PAO1 cells by standard soft agar overlay and subsequent PEG 8000 precipitation (Ceyssens *et al.*, 2008b). The phages were stored in phage buffer (10 mM Tris pH7.5 (Sigma Aldrich), 10 mM $MgSO_4$, 150 mM NaCl) and the 'phage titer' was determined by plating a dilution series of the phage using standard soft agar overlay and determination of the 'plaque forming units' (pfu) per ml.

3.2. DNA cloning and manipulations

3.2.1. Polymerase chain reaction

DNA fragments for cloning were amplified by PCR. The PCR mix contained 0.4 µM of each primer (see Table 2) (Integrated DNA Technology, Coralville, IA, US), 0.2 mM of each deoxyribonucleotide triphosphate (dNTP, Thermo Scientific), 2.5 U *pfu* DNA polymerase (Thermo Scientific), *pfu* buffer (with Mg_2SO_4) (Thermo Fisher) and 10 ng of DNA template. PCR was performed in a T3000 Thermocycler (Biometra, Göttingen, DE) with 30 or 35 amplification cycles. For KAPA PCR, 1 U KAPA HiFi polymerase (Kapa Biosystems, Boston, MA, US) was mixed with KAPA hotstart ReadyMix (Kapa Biosystems), 0.2 µM of each primer and 10 ng of DNA. Primer annealing temperatures were adjusted to the primer melting temperatures and extension time was adjusted to the amplicon length and polymerase processivity.

Colony PCR was used to analyze cloning experiments. Individual colonies were picked after transformation and grown in 100 µl LB with a corresponding antibiotic at 37° C for 2h. PCR reactions were performed in 50 µl volume with 5 µl of these cultures as a DNA template, 0.2 mM of each dNTP, 0.3 µM of each primer, DreamTaq Green buffer and 2.5 U DreamTaq DNA polymerase (Thermo Scientific).

Table 2: Primers for cloning, used in this dissertation. Restriction sites are underlined.

Vector	DNA (fragment)	Forward	Reverse
pEXP5-NT/TOPO	Vector	TAATACGACTCACTATAGGG	ATCCGGATATAGTTCCTCCTTTC
	phiKZ_gp37_D137/8A	GAATTTATGCCAGGTGTTCATGTTGCTGCTATCAGTGA TAAACTAATCAAGTCGT	ACGACTTGATTAGTTTATCACTGATAGCA GCAACATGAACACCTGGCATAAATTC
	phiKZ_gp37_E214/22A	GTATATTTTAGTTTTGCAGGATGCCATCCAGATGTTGA GGCAGTTCTATTTACCATTAAG	CTTAATGGTAAATAGAACTGCCTCAACATC TGGATGGCATCCTGCAAAACTAAAATATA C
pUC18_mini-Tn7T-Lac-GW	Vector	CGGTTCTGGCAAATATTCTGA	GGAGGGGTGGAAATGGAGTT
	phiKZ_gp37	GCGCTGCAGATGACTCAATTTAACATC	CCGCTCGAGAAAATTAAATAGTACACC
	phiKZ_gp37_strp	GCGCTGCAGATGACTCAATTTAACATC	ATACTCGAGTTATTTTTCGAACTGCGGGT GGCTCCAAGCGCTAAAATTAAATAGTACA CC
pME_6032	Vector	ATGGCTGTGCAGGTCGTA	TCCCGCACGATGATCGT
	RBS_100_as	GCGCTCGAGGTGTATTATTTTTAATAAATG	CAGCCATGGGAGATATCCTCTAATTTATG
	RBS_200_as	GCGCTCGAGGTGTATTATTTTTAATAAATG	GAACCATGGACTTGACTGCGGTTTAAAAG
	RNE_583_835_strp	ATAGAATTCATGGCCGAGCGCCAAACCCGCCAG	TAGGTACCTTATTTTTCGAACTGCGGGTG GCTCCAAGCGCTATCGCTTGCCGTGGTTTC
	SacI_KpnI_cut	CCTACTGCAGCTGAACACTAGTATCGGTAC	CGATACTAGTGTTCAGCTGCAGTAGGAGC T

3.2.2. Mutagenesis PCR

Mutagenesis PCR was used to generate site-specific mutations in Dip. The PCR mix contained *pfu* reaction buffer (Agilent Technologies, Santa Clara, US), 10 ng of DNA template (pEXP5-NT/TOPO, see 3.2.5), 0.2 mM of each dNTP, 10 µM of each primer (Sigma Aldrich) (see Table 2), 1 mM DMSO (dimethylsulfoxide) and 2.5 U *pfu* Turbo DNA polymerase (Agilent Technologies). Primer annealing temperatures were adjusted to primer melting temperatures and the extension time was 4 minutes. Subsequently DpnI (Thermo Scientific) was added to digest dam methylated wild type plasmid at 37°C (2h). Finally, mutagenized plasmids were transformed to *E. coli* DH5α, using standard heat shock transformation (see 3.1.2).

3.2.3. DNA purification

The GeneJet PCR Purification Kit (Thermo Scientific) was used to purify PCR products and bacterial genomic DNA was purified with the GeneJet Genomic DNA purification Kit (Thermo Scientific). For these kits, the company's instructions were followed. DNA concentrations were measured with a NanoDrop ND-1000 spectrophotometer (Nano Technologies, Wilmington, DE). For plasmid DNA, the

GeneJet Plasmid Miniprep Kit (Thermo Scientific) was used, following the manufacturer's instructions.

3.2.4. DNA manipulations

To assess the purity and size of the DNA fragments, DNA separation by agarose gel electrophoresis was used. 6x Loading dye (40% (w/v) sucrose (Acros Organics), 0.1 % (w/v) bromophenol blue (Sigma Aldrich)) was added to the samples before loading them on a 1% (w/v) agarose (Sigma Aldrich) gel in TAE electrophoresis buffer (40 mM Tris, 500 mM sodium acetate (Acros Organics), 50 mM ethylenediaminetetraacetic acid (EDTA, Acros Organics), pH 7.2). The samples were run in a 150 V electric field and the gel was stained with ethidium bromide (Life Technologies). For size determination, a λ/PstI ladder (Thermo Scientific) was used. DNA bands were visualized by UV illumination.

3.2.5. Cloning and sequencing analysis

DNA fragments were amplified with primers containing overhangs with specific restriction sites (see Tables 2 and 3). Next, both the destination vector and DNA fragment were incubated with the corresponding restriction endonucleases (Thermo Scientific) and an appropriate buffer was added according to the company's instructions. Subsequently, the DNA was purified (see 3.2.3) and the linear vectors were dephosphorylated with FastAP (thermosensitive alkaline phosphatase, Thermo Scientific) by incubation at 37° C for 10 minutes. After enzyme inactivation, the DNA fragments were ligated to the vector using T4 DNA ligase (Thermo Scientific) and T4 DNA ligase buffer (Thermo Scientific). A tenfold excess of the insert DNA was used for ligation. After inactivation (10 minutes at 65°C) of the T4 DNA ligase, the recircularized plasmids were transformed to *E. coli* TOP10 cells (see 3.1.2).

Table 3: Restriction endonucleases used in this dissertation.

Vector	DNA (fragment)	Restriction endonuclease
pUC18_mini-Tn7T-Lac-GW	phiKZ_gp37	PstI (F), xhoI (R)
	phiKZ_gp37_strp	PstI (F), xhoI (R)
pME_6032	RBS_100_as	XhoI (F), NcoI (R)
	RBS_200_as	XhoI (F), NcoI (R)
	RNE_583_835_strp	EcoRI (F), XhoI (R)
	SacI_KpnI_cut	SacI (F), PstI (vec), SpeI (vec), KpnI (R)

In this dissertation, two *E. coli* vectors were used. Dip was fused to a His-tag using the pEXP5-NT/TOPO vector (Life Technologies). *P. aeruginosa* RNA degradosome fragments were fused to a GST-tag (N-terminal) in a pGEX-6p1 vector (GE life sciences) (available in the lab of prof. Ben Luisi). In addition, two *P. aeruginosa* vectors were used. Dip antisense transcripts and paired termini were cloned in a pME6032 vector, as well as a C-terminal RNase E fragment containing both RNA binding sites (residues 583-835). Dip was fused to GFP in a pUC18 mini vector. DNA sequencing samples were prepared with 400ng of template and 2.5 µM of forward and reverse primers. DNA sequence analyses were performed by GATC Biotech AG (Konstanz, Germany).

3.3. Protein/peptide expression and purification

3.3.1. Dip expression and purification

E. coli BL21 (DE3) pLysS (Life Technologies) was used for heterologous expression of wild type and mutant Dip with an N-terminal His-tag. After transformation of the pEXP5-NT/TOPO expression plasmid (see 3.2.5), *E. coli* cells were grown at 37°C in 1L 2xLB medium, supplemented with 100 µg/ml ampicillin (Amresco®, VWR International Ltd, Solon, Ohio, VS) and 34 µg/ml chloramphenicol (Sigma Aldrich). When an OD_{600nm} of 0.3 was reached, the cells were induced with 1 mM IPTG and grown for another 6h at 37 °C or overnight at 16 °C. Subsequently, the cells were pelleted by centrifugation, resuspended in nickel load buffer (50 mM imidazole (Acros Organics), 200 mM NaCl, 20 mM Tris pH 7.5 (Sigma Aldrich)) and lysed by sonication or high pressure cell rupture (EmulsiFlex-C5, Avestin, Mannheim, Germany). After centrifugation, the supernatant was filtered with a 0.45 µm filter and Dip was purified with an Äkta pure chromatography system (GE healthcare) using a HisTrap FF column (GE Healthcare). After loading the filtered supernatant (3 ml/min) the columns were washed with 15 ml of nickel load buffer (3 ml/min) and eluted with elution buffer (500 mM imidazole, 200 mM NaCl, 20 mM Tris pH 7.5). A second purification step was performed by size-exclusion chromatography, using a Superdex 200 16/600 column (GE life sciences) according to the manufacturers protocol and with an optimized running buffer (200 mM NaCl, 20 mM Tris pH 7.5 and 1 mM DTT). The purified protein was concentrated by ultracentrifugation and used directly for (co-)crystallization and SEC- SAXS experiments (see 3.6 and 3.7), or 10% glycerol was supplemented for storage at -80°C.

3.3.2. RNase E peptides: expression and purification

E. coli BL21 (DE3) was used to express fragments of the CTD of RNase E (RNase E fragments 583-636, 583-835, 756-775 and 756-901) fused to an N-terminal GST-tag. After transformation of the

pGEX-6p1 expression vectors, cells were grown at 37°C in 1L 2xLB medium, supplemented with 100 µg/ml ampicillin. When an OD_{600nm} of 0.3 was reached, the cells were induced with 1 mM IPTG and grown for another 2h at 37 °C. Subsequently, the cells were pelleted by centrifugation, resuspended in 15 ml purification buffer (20 mM Tris pH 7.5, 200 mM NaCl, 5 mM EDTA) and lysed by sonication or high pressure cell rupture. After centrifugation, the supernatant was filtered with a 0.45 µm filter and the RNase E fragments were purified with glutathione affinity chromatography, followed by heparin affinity chromatography on an Äkta Pure chromatography system (GE Healthcare). After glutathione affinity chromatography, the GST tag was cleaved overnight with 3C protease (Thermo Scientific). The peptides were directly used for co-purification, crystallography and SEC-SAXS experiments or 10% glycerol was supplemented for storage at -80 °C.

For co-crystallization (see 3.6), SEC-SAXS (see 3.7), SEC-MALS and AUC experiments (see 3.5), Dip was co-purified with RNase E (CTD) peptides (residues 756-775, 583-636 and 583-835) using a Superdex 200 16/600 column (GE life sciences) according to the manufacturer's protocols.

3.3.3. SDS-PAGE and quality control

The composition and purity of purified protein/peptide samples were assessed by Sodium dodecyl sulphate-polyacrylamide gel electrophoresis (SDS-PAGE). The samples were then dissolved in 4x loading buffer (200mM Tris pH 6.8, 8 mM EDTA, 40 % (v/v) glycerol, 4 % (w/v) SDS, 0.4% (w/v) bromophenol blue) and loaded on a 10 % or 12 % (v/v) 37.5:1 acrylamide/bis-acrylamide (Bio-Rad) gel (made in Tris/SDS buffer (1.5 mM Tris pH 8.8, 0.4% (w/v) SDS (Janssen Chemika) with 0.01% (v/v) APS (ammonium persulfate, Sigma Aldrich) and 0.001 % (v/v) TEMED (N,N,N',N' tetramethylethylene diamine, Sigma Aldrich)), depending on the molecular weight of the proteins/peptides. Short RNase E fragments were run on 8%-12% NuPage Bis-Tris precast gradient gels (Thermo Scientific). A Tris/glycine buffer (25mM Tris pH 8.3, 192 mM Glycine (Acros Organics), 0.1 % (w/v) SDS) was used to run the gels in. An electric field of 150 V was applied. Finally, the gels were coomassie stained with GelCode Blue Safe (Thermo Scientific) or with Imperial Protein Stain (Thermo Scientific) if a higher sensitivity was needed. As a reference the pre-stained protein ladder 'PageRuler' (Thermo Scientific) or a 'Mark12 standard' (Thermo Scientific) was used. Concentrations of the corresponding protein samples were measured with a NanoDrop ND-1000 spectrophotometer.

3.3.4. Western Blot analysis

Dip was purified extensively and samples of 5 mg/ml (150 µM) were sent to Pharmabs (KULeuven, Leuven, BE) for the production of polyclonal antibodies in 2 rabbits. A 550 ml *P. aeruginosa* culture was grown to an OD_{600} of 0.3 before infection with phiKZ bacteriophages at a multiplicity of infection

of 5. Next, 30 ml of *P. aeruginosa* culture was collected every 3 minutes post phiKZ infection and phage infection was halted by shaking the subcultures in an ice bath for 10 minutes. The cells were lysed by sonication and subjected to SDS-PAGE (see 3.3.3). Subsequently, proteins were transferred to a nitrocellulose membrane (Hybond-C Extra, GE Healthcare), which was then blocked with PBST buffer (PBS + 0.1 % (v/v) Tween, pH 7.5) containing 5% (w/v) powder milk (Nestlé Belgium NV, Brussels, BE) at T_{room} for one hour. Subsequently, the membrane was incubated with a 1/5000 dilution (in PBST buffer, 0.1% (w/v) powder milk) of the polyclonal anti-Dip antibodies for one hour at T_{room}. After three washing steps (3 min each) with PBST buffer, the membrane was incubated with a 1/5000 dilution of Anti-Rabbit IgG (H+L) antibodies conjugated to Horse Radish Peroxidase (HRP, Promega Cooperation) for one hour at T_{room}. Readout was carried out by enhanced chemiluminescence (GE healthcare).

3.4. Interaction techniques

3.4.1. Electrophoretic Mobility shift assay (EMSA)

EMSAs were used to assess interactions between Dip (both wild type and mutants) and several RNase E peptides (residues 583-636, 583-835 and 756-901) as well as interactions between RNase E fragments and different RNA substrates (9S RNA, 27-mer RNA and 13-mer RNA, all available at the Lab of prof. Ben Luisi, Cambridge, UK), in the presence and absence of Dip. Dip was diluted and mixed with a dilution of an RNA fragment and/or a dilution of an RNA degradosome fragment in 20 mM Tris pH7.5 and 200 mM of NaCl. After a 10 min incubation period at T_R, Loading dye (0.2 % (w/v) bromophenol blue, 300 mM DTT and 50% (w/v) glycerol) was added and the samples were loaded on a 10% native polyacrylamide gel (acrylamide/Bis-acrylamide (30%/0.8% w/v) 0.375M Tris pH 8.8, 10 % (w/v) APS and 0.001% TEMED) and run in running buffer (25 mM Tris, 250 mM Glycine) with an applied electric field of 150 V. Sybr gold (Invitrogen) was used to stain the gel for RNA visualization, whereas proteins were visualized by Coomassie staining.

3.5. Analytical ultracentrifugation (AUC) and Size-exclusion Chromatography Multi-Angle Light Scattering (SEC-MALS)

Absorbance-based sedimentation velocity experiments (analytical ultracentrifugation, AUC) were used to estimate the mass and interaction stoichiometry of a complex of Dip and RNase E (residues 583-835). These experiments were performed using a Beckman model XL-I analytical ultracentrifuge (Beckman Coulter) using a 4-hole An-60 Ti rotor. 400 µl of protein complex (1 mg/ml) was loaded in double-sector sapphire cells and 400 µl of reference (20 mM Tris pH 7.5, 200 mM NaCl). Solvent

density and viscosity and the partial specific volume of the proteins were calculated with SEDNTERP (Laue *et al.*, 1992). Measurements were performed at 20°C with a rotor speed of 20,124 RCF (50,000 rpm). Absorbance data was collected at a wavelength of 280 nm. To determine the optimal radial positions for the measurements, initial scans were carried out at 724.5 RCF (3,000 rpm). SEDFIT was used to fit sedimentation velocities to a continuous molar mass [c(M)] by means of Lamm equation modelling (Schuck, 2000).

For SEC-MALS, All samples were purified by affinity chromatography and size-exclusion chromatography before loading them on a HPLC MALS (Wyatt technologies, Santa Barbara, US). HPLC columns were equilibrated overnight with the appropriate buffer. MALS data was processed in ASTRA (Wyatt technologies).

3.6. Crystallography

Both wild type and one Dip mutant were expressed and purified for (co-)crystallization experiments (see 3.3.1). The best diffracting crystals for wild type Dip were produced in a condition of 0.7 M NaCl, 0.1 M MES pH 6.0, 0.1 M KH_2PO_4, 0.1 M NaH2PO4 and 0.2 M sodium thiocyanate, at 4 °C. This is in agreement with previous successful crystallization conditions for Dip, except for the temperature (Van den Bossche *et al.*, in submission). The best diffracting crystals for the Dip mutant were produced in a condition of 0.5 M NaCl, 0.1 M MES pH 6.0, 0.1 M KH_2PO_4, 0.1 M NaH_2PO_4, 0.2 M sodium thiocyanate and 1 mM GSH, 1mM GSSG, at 4 °C. Datasets were collected at ESRF (Grenoble, France) and Diamond light source (Didcot, UK) and used to solve the crystal structures of wild type and mutant Dip. Diffraction-images were indexed and integrated in IMosflm (Battye *et al.*, 2011). Datasets were scaled and merged with Aimless (Evans & Murshudov, 2013). Initial models were built by molecular replacement in PhaserMR (McCoy *et al.*, 2007), and completed and improved by manual model building in Coot (Emsley & Lohkamp, 2010) and iteratively using Refmac5 (Murshudov *et al.*, 1997).

Crystal structures of Dip in complex with an RNA binding peptide from RNase E (residues 756-775) were completed and refined manually in Coot and iteratively with Refmac5 (the crystal structure of this complex was solved before the onset of this dissertation). Candidate Dip residues responsible for target binding were chosen from this crystal structure and mutagenized (see 3.2.2). After co-purification of Dip with the same RNase E recognition peptide, the complex was co-crystalized again. Furthermore, attempts were made to co-crystalize Dip with longer C-terminal RNase E fragments (residues 583-636 and 583-835). In addition, several C-terminal RNase E fragments (residues 583-835, 756-901, 756-901 + GST-tag) were used for crystallization screens.

3.7. Size-exclusion Chromatography Small-angle X-ray Scattering (SEC-SAXS)

Although X-ray crystallography offers structural information with unparalleled atomic resolution, it is restricted to describing macromolecules which have adopted low energy states in crystal lattices. SEC-SAXS offers additional information on conformation, shape, macromolecular folding and assembly state in solution. However, a resolution range of only 50 Å to 10 Å can be achieved with small-angle X-ray scattering. Despite the lower resolution, there are no size limitations, which are inherent to NMR analyzes and electron microscopy. In both SAXS and crystallography the sample is placed in a highly collimated X-ray beam and the scattered X-rays are measured by an X-ray detector. In SAXS, however, the sample is not a crystal but a highly concentrated and monodisperse solution of the protein of interest. As in crystallography, the angle of any scattered position with the direct beam is 2θ, and the higher the scattering angle, the better the resolution (see Figure 11). In crystallography, both directional and positional information is given by the Patterson autocorrelation function. This function contains cross peaks in a u,v plane for every interatomic distance within a crystal. In SAXS, interatomic distances, but not directions, within each scattering unit are resolved in the pair-distribution autocorrelation function, which is the Patterson function-equivalent for SAXS. Thus, in the pair-distribution autocorrelation function, all equivalent interatomic distances add together (see Figure 11) (Putnam *et al.*, 2007). A recent advancement to facilitate quality assessment is to use size-exclusion chromatography immediately before collecting scattering data (SEC-SAXS). As such, aggregation of the protein sample is minimized and the reliability of the scattering data is improved (Watanabe & Inoko, 2009, 2011; Malaby *et al.* 2015)).

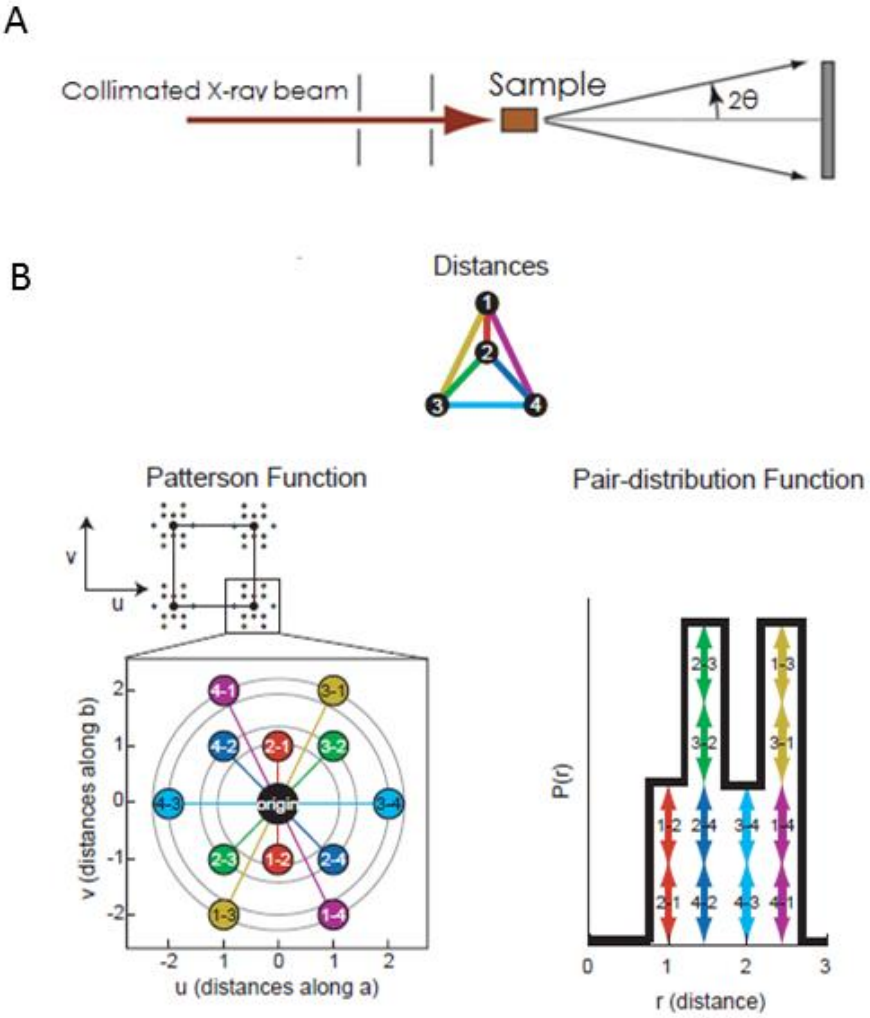

Figure 11: Schematic representation of a SAXS and crystallography experimental setup and output. A: The sample is irradiated with a highly collimated X-ray beam and the scattered X-rays are detected by an X-ray detector. B: Comparison between the Patterson autocorrelation function in X-ray crystallography and the pair-distribution autocorrelation function for SAXS for a theoretical two-dimensional molecule of four atoms. The cross peaks, one for every interatomic distance, in the u,v plane of the Patterson function (left) contain both positional and directional information about the atoms in the crystal. The pair-distribution function for SAXS retains distances but not directions within each scattering unit (right) (adapted from Putnam *et al.*, 2007).

Dip was expressed and purified in a storage buffer of 0.2 M NaCl, 20 mM Tris pH 7.5, 5% glycerol and 1 mM DTT. Subsequently, Dip was concentrated to a concentration of 17 mg/ml (510 µM) or 50 mg/ml (1.5 mM) and flash frozen (in liquid nitrogen) for SEC-SAXS measurements. SEC-SAXS measurements were performed at diamond light source (beamline 21) and SOLEIL synchrotron (Saint-Aubin, France). Size-exclusion chromatography (SEC) was performed immediately before data collection to ensure monodispersity of the sample. An Agilent 1200 HPLC system with 4.6 ml KW-402 and -404 columns (Shodex) was used for SEC. Data collection was triggered when a threshold peak height was reached during elution. In Table 4 all programs used for data processing, as well as a short description are given.

Table 4: List of programs used for processing SAXS data.

Program	Description	Reference
Primus	Manipulations with experimental 1D SAXS data	Konarev *et al.*, 2003
GNOM	Indirect Fourier transform program to evaluate the particle distribution function	Svergun, 1992
CRYSOL	Calculation of X-Ray scattering profiles from known high resolution structures	Svergun *et al.*, 1995
FoXS	Fast SAXS profile computation with Debye formula	Schneidman-Duhovny *et al.*, 2013
SReflex	Flexible refinement of high-resolution models combining SAXS and NMA	Panjkovich & Svergun, 2016
SASREF	Rigid body modeling of multisubunit complexes	Petoukhov & Svergun, 2005
GASBOR	*Ab initio* reconstruction of a protein structure by a chain-like ensemble of dummy residues	Svergun *et al.*, 2001
DAMMIF	Rapid *ab initio* shape determination by simulated annealing using a single phase dummy atom model	Franke & Svergun, 2009
Damsel	Compares a set of models, finds the most probable one and outliers	Volkov & Svergun, 2003
Damsup	Aligns all models with the most probable one	Volkov & Svergun, 2003
Damaver	Averages the aligned models and computes probability map	Volkov & Svergun, 2003
Damfilt	Filters an averaged model from the probability map at a given cut-off volume	Volkov & Svergun, 2003
Damstart	Generates an input file with fixed core for DAMMIN, starting from the averaged model	Volkov & Svergun, 2003
DAMMIN	*Ab initio* shape determination using a dummy atom model	Svergun, 1999
SUPALM	Superposition of 3D structures on one another using spherical harmonics representations	Konarev *et al.*, 2006

3.8. Electron Microscopy (EM)

Preliminary screens for cryo-EM were performed on a regular EM to assess particle size, shape, spacing, monodispersity and aggregation. Dip was co-purified with the *E. coli* ternary complex (available at the lab of professor Ben Luisi, Cambridge, UK) with an Äkta pure chromatography system (GE healthcare), using a Superdex 200 16/600 column (GE life sciences). As the stoichiometry of this complex was not known, molar concentrations were based on stoichiometry estimates from AUC experiments (see 3.5) and samples were concentrated to 34.78 µM (5 mg/ml). Glow discharged carbon coated copper grids (Cambridge Advanced Imaging Centre, University of Cambridge, UK) were prepared using several dilutions and staining times. Grids were screened with a 200 kV Tecnai G2 transmission electron microscope (Cambridge Advanced Imaging Centre, University of Cambridge, UK).

4. Results and discussion

4.1. Dip hijacks both RNA binding sites on RNase E via a negatively charged patch on its outer surface

4.1.1. Both RNA binding sites on RNase E are targeted by Dip

Extensive bacterial two-hybrid and mobility shift assays have identified RNase E [756-775], which co-localizes with the AR2 RNA binding site, as a target site for Dip. Moreover, mobility shift assays indicate that Dip competes with RNA for binding this RNA binding site. In addition, a second target site, RNase E [583-636], was identified, albeit with a lower affinity. This second interaction site aligned well with the RBD RNA binding site, which suggests that Dip hijacks the second RNA binding site on the RNase E scaffold domain as well (Van den Bossche *et al.*, in submission). An additional mobility shift assay was used to asses RNA binding to RNase E [583-636] in the presence of Dip. Therefore, Dip and RNase E were purified by affinity chromatography and size-exclusion chromatography (see 4.1.2). These assays indicate that there is a competitive binding of 9S RNA and Dip to RNase E [583-636] (see Figure 12). An incubation time of 10 minutes was used, before Dip was added, to allow interaction of the RNase E fragment with the 9S RNA. To bind the RNase E fragment, Dip would have to displace the 9S RNA. As the incubation concentration increases, 9S RNA is gradually displaced from RNase E [583-636]. A 2:1 excess of Dip is sufficient to capture all RNA binding sites and displace all RNA.

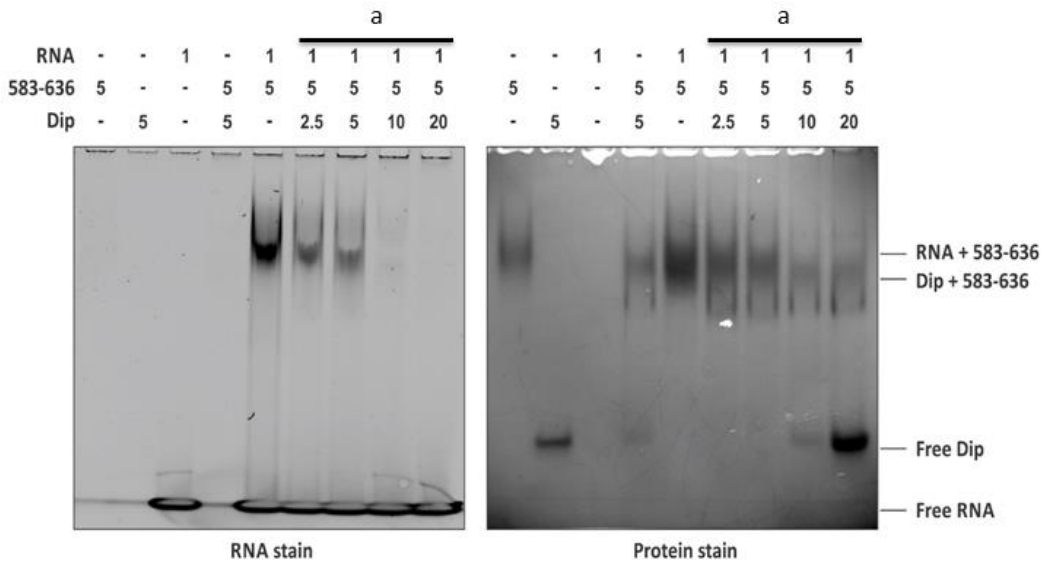

Figure 12: Dip competes with the binding of 9S RNA to RNase E [583-636]. Mobility shift assay of 9S RNA, RNase E [583-835] and Dip. After running the samples on a 8 % native acrylamide gel, RNA was visualized under UV (SYBR gold RNA stain was used) (left). Subsequently, the gels were stained with coomassie (protein stain) (right). The 'a' sections indicate the samples that were incubated with increasing amounts of Dip (after adding RNA and mixing). Concentrations are given in µM (adapted from Van den Bossche *et al.*, in submission).

Together with the previous findings, these results show that Dip specifically binds to both RNA binding sites (AR2 and RBD) on the RNase E scaffold domain and thereby prevents structured RNA from binding (see Figure 13). Thus, Dip impedes degradation of these RNA species in a direct manner, protecting phiKZ transcripts. As such, Dip aids bacteriophage proliferation and amplification in the host cell.

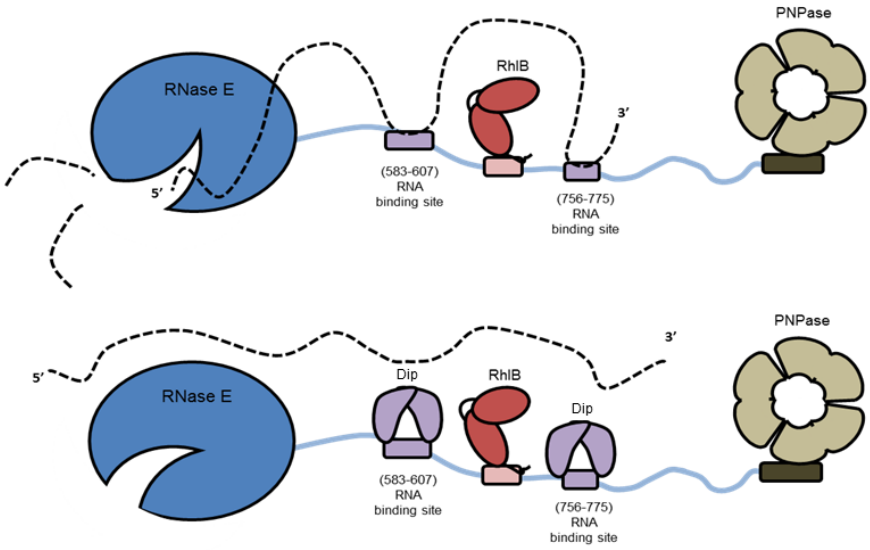

Figure 13: Displacement of structured RNA from the RNA binding sites on RNase E by Dip. Top: In the absence of Dip, mRNA is bound by both RNA binding sites on the scaffold domain of RNase E and degraded by the catalytic domain. Bottom: When Dip is present, both RNA dinding sites are hijacked and mRNA is no longer bound to RNase E and degraded (adapted from Van den Bossche *et al.,* in submission).

4.1.2. Co-crystallization experiments and bioinformatics analysis reveal a possible RNase E binding site on the outer Dip surface

To further elucidate the interaction between Dip and RNase E, a complex of Dip and a synthetic RNase E fragment (residues 756-775) was co-crystalized. Hexagonal crystals of Dip were obtained and the crystal structure was solved to a resolution of 2.7 Å by molecular replacement. Through crystallographic symmetry, a ring-like hexamer of Dip monomers was formed (see Figure 14 A). Discontinuous density was observed in an acidic pocket on the surface of each Dip monomer and eight residues of RNase E [756-775] were modelled into this density. Moreover, this possible RNase E binding site was in accordance with the predicted binding site by using the docking program DOT (see 1.4.2) (Van den Bossche *et al.*, in submission). At the onset of this dissertation, this crystal structure was manually refined in Coot (Emsley & Lohkamp, 2010) using real space refinement and model geometry refinement, as well as alternative rotamer fitting. In addition, manual fitting of the residues to the electron density was performed. The number of Ramachandran outliers was reduced from 116 (7.55 % of all residues) to 28 (1.83% of all residues). Finally, iterative cycles of refinement were performed with Refmac5 (Murshudov *et al.*, 1997) (see Table 5). When DOT was previously

used to predict the RNase E binding sites on the Dip dimer (see 1.4.2), the peptide was modelled as an α-helix. However, no such secondary structure was observed in the refined crystal structure of Dip and RNase E [756-775] (see Figure 14).

In addition, when no crystallographic symmetry is used a condensed helix-like hexamer of Dip is observed in the crystallographic unit cell. In this conformation, six RNase E [756-775] peptides are bound to the outer surface of the helical Dip oligomer (see Figure 14 B, C). This alternative oligomeric assembly is equally plausible, as the H32 space group allows for a continuous helical formation of the contents in the crystallographic asymmetric unit.

Table 5: Relevant diffraction and refinement parameters of the Dip + RNase E [756-775] crystals.

Resolution range (Å)	72.16-2.7
Space group	H32 (R32:H)
Unit cell	136.8/136.8/91 - 90/90/120
R-work	0.2383 (0.2923)
R-free	0.3011 (0.3289)
Ramachandran favored (%)	89.06
Ramachandran outliers (%)	3.21

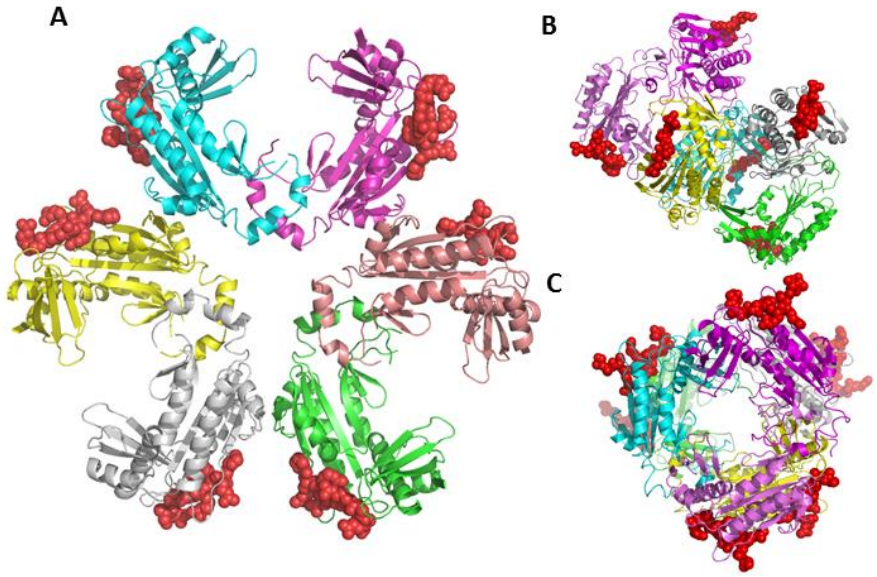

Figure 14: Crystal structures of Dip in complex with RNase E [756-775]. A: Crystallographic symmetry revealed a ring like hexamer of Dip monomers. The RNase E peptides are bound to the outer surface of each Dip dimer. B and C: Side- and top view of an alternative helical Dip assembly in the crystallographic unit cell. RNase E peptides are bound to the outer edges of the condensed Dip Helix. Dip monomers are in blue, yellow, grey, green, pink and purple. The RNase E residues are represented by red spheres.

The crystals of Dip in complex with RNase E [756-775] were obtained by co-purifying and co-crystalizing Dip with a synthetic RNase E [756-775] peptide. In this dissertation, attempts were made to co-crystalize Dip with a heterologously expressed RNase E [756-775] peptide from *E. coli*.

The peptide was purified using glutathione affinity chromatography and heparin affinity chromatography. In parallel, Dip was purified using affinity chromatography and size-exclusion chromatography. Subsequently, Dip and RNase E [756-775] were co-purified using size-exclusion chromatography (see Figure 15 A). An additive screen was set up at 4°C for the condition of 0.3 M NaCl, 0.1 M MES pH 6.0, 0.1 M KH_2PO_4, 0.1 M NaH_2PO_4 and 0.2 M sodium thiocyanate, in correspondence with the conditions that produce the previous hexagonal crystals. Hexagonal crystals were obtained after 14 days for the 1 mM GSH + 1mM GSSG additive (reduced and oxidized L-glutathione) (see Figure 15 B). Additional hexagonal crystals were observed after one month when 0.1 potassium sodium tartrate tetrahydrate was used as an additive (data not shown).

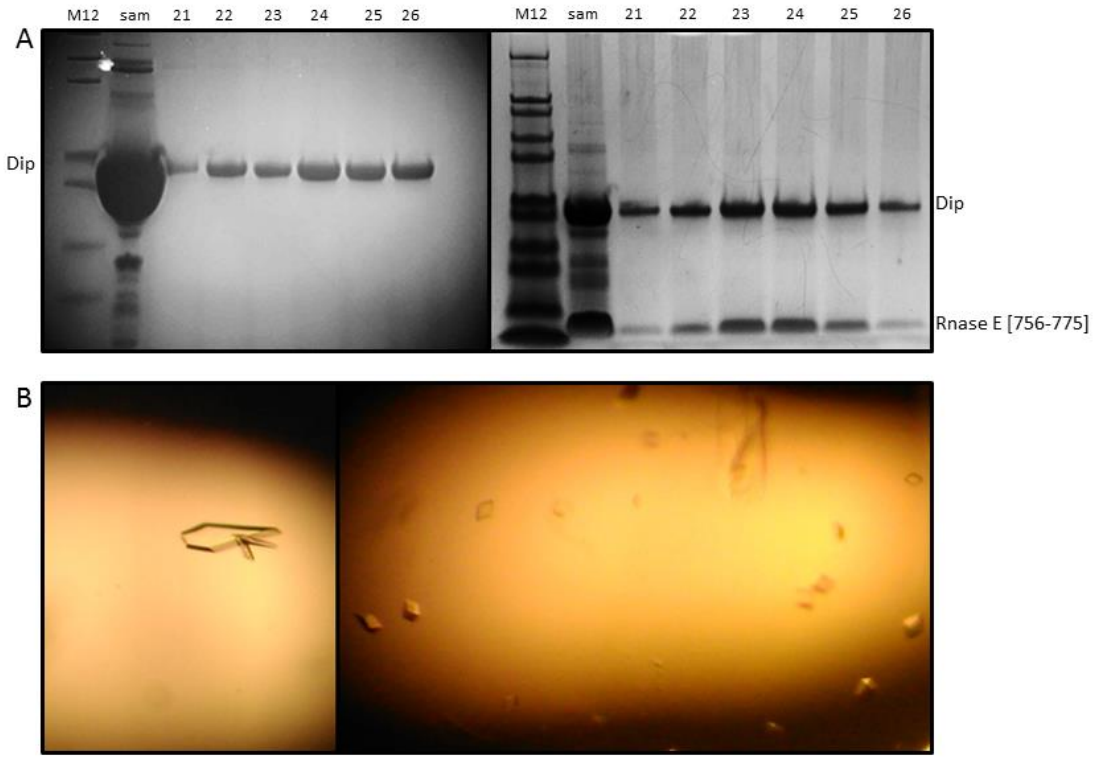

Figure 15: Co-crystallization and co-purification of Dip and RNase E [756-775]. A: SDS-PAGE gels of Dip after size-exclusion chromatography (left) and of co-purified Dip and RNase E [756-775] after size-exclusion chromatography. Elution fractions are presented above each gel. M12, molecular weight ladder, sam, injected sample. B: Hexagonal crystals of Dip + RNase E [756-775] were formed at 4°C in 0.3 M NaCl, 1 mM GSH, 1mM GSSG, 0.1 M MES pH 6.0, 0.1 M KH_2PO_4, 0.1 M NaH_2PO_4 and 0.2 M sodium thiocyanate. Rhomboid-like crystals were grown in 0.5 M NaCl, 1 mM GSH, 1 mM GSSG; 0.1 M MES pH 6.0, .1 M KH_2PO_4, 0.1 M NaH_2PO_4 and 0.2 M sodium thiocyanate.

Unfortunately, all obtained crystals were small and no full dataset could be collected on a standard synchrotron X-ray beamline. However, some of crystals were screened using a standard beamline and the same space group and unit cell dimensions as for Dip co-crystalized with synthetic RNase E [756-775] were observed, even though the best resolution achieved was only 5.5 Å. These results indicate that Dip co-crystalizes with both synthetic and heterologously expressed RNase E [756-775] and that the same crystal structure should be expected for both complexes. Higher resolution datasets could be obtained in the future by exposing these crystals to a focused

X-ray beam. Finally, optimization screens were set up in 24-well plates for the 1 mM GSH-GSSG additive, in order to obtain larger crystals. Even though no hexagonal crystals were observed, a new rhomboid-shaped crystal had formed at 4°C in a buffer of 0.5M NaCl, 1 mM GSH, 1mM GSSG, 0.1 M MES pH 6.0, 0.1 M KH_2PO_4, 0.1 M NaH_2PO_4 and 0.2 M sodium thiocyanate (see Figure 15 B). Unfortunately, attempts to capture this crystal for data collection failed.

4.1.3. Site-directed mutagenesis experiments confirm the predicted interaction site

From the crystal structure of Dip bound to RNase E [756-775], four Dip residues were identified as binding candidates for RNase E [756-775], based on their orientation, charge and distance from the target peptide: Asp137, Asp138, Glu214 and Glu222 (see Figure 16). To validate the RNase E binding site, each of these residues was substituted, in pairs, for alanine using site directed mutagenesis PCR. In one mutant, both D137 and D138 were substituted for alanine. In the second mutant, E214 and E222 were substituted for alanine. An additional mutant was made with all four residues substituted for alanine. Mobility shift assays were used to assess the binding of the mutants to two RNase E target fragments (residues 583-636 and 756-901), each containing one of two RNA binding sites. Therefore, each mutant was mixed with the RNase E target fragments and incubated for 10 minutes before loading them on an 8 % native acrylamide gel.

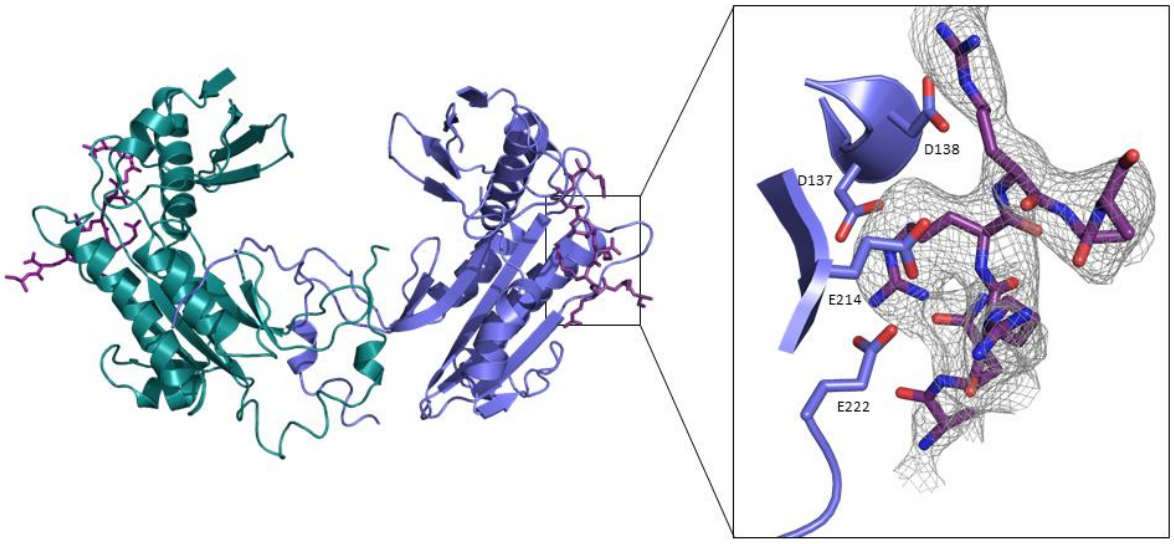

Figure 16: RNase E interacts with the outer surface of the Dip clamp. Left: one Dip dimer was selected from the Dip hexamer in the crystallographic unit cell, together with the binding RNase E peptides. Right: four Dip residues (D137, D138, E214 and E222) were chosen as possible binding candidates for RNase E and substituted for alanine. Dip protomers are depicted in blue and cyan, RNase E residues are depicted in purple (left). The electron density for the RNase E peptide is represented as a grey mesh (right) (adapted from Van den Bossche *et al.*, in submission).

In a first electrophoretic mobility shift assay all three mutants were tested for their binding capacity to RNase E [756-901], which contains the AR2 RNA binding site. Therefore, RNase E [756-901] was expressed in *E. coli* and purified by affinity purification (see appendix 1). The interaction between

wild type Dip and RNase E [756-901] was used as a reference (see Figure 17). A clear shift occurs when wild type Dip interacts with RNase E [756-901]. All mutants have lower affinity for the RNase E target compared to wild type Dip. The D137/137A Dip mutant (Dip 137/138) has lower affinity for RNase E [756-901] than the wild type Dip, although there is still some interaction. The E214/222A Dip mutant (Dip-214/222), on the other hand, has no affinity for RNase E [756-901], as there is no shift at all. The double mutant has very low affinity for RNase E [756-901], but might be unstable, since some degradation is observed in both lanes containing this double mutant (see Figure 17).

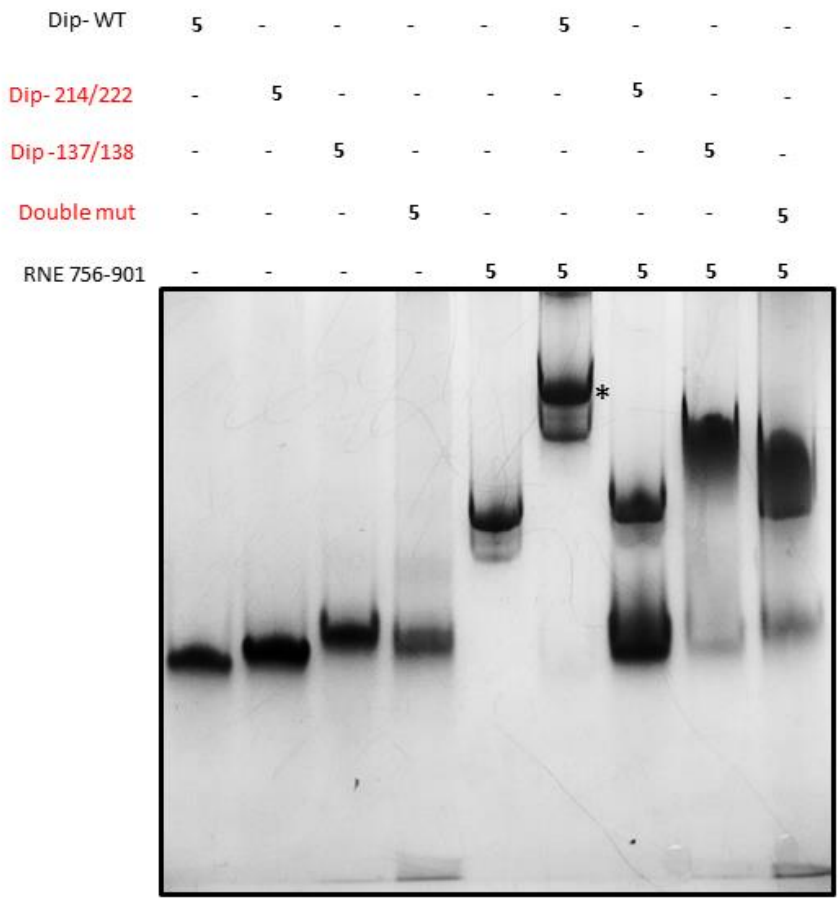

Figure 17: Electrophoretic mobility shift assay for all three mutants of Dip and RNase E [756-901]. The first four lanes contain wild type Dip and all three mutants, respectively. The fifth lane contains the RNase E target. A clear shift is observed when wild type Dip is mixed with the RNase E target (lane six, *). No shift is observed when Dip-214/222 is mixed with the RNase E peptide (lane 7). Small shifts are observed when the D137/138A Dip mutant and the double mutant are mixed with RNase E [756-901]. Concentrations are presented in μM.

To further elucidate and validate the interaction behavior of Dip-214/222, an additional EMSA was performed (see Figure 18). Both wild type Dip and Dip-214/222 were mixed with RNase E [756-901], which contains the AR2 RNA binding site, and RNase E [583-636], which contains the RBD RNA binding site. All samples were incubated for 10 minutes and loaded on an 8 % native acrylamide gel. This additional EMSA indicates that Dip-214/222 has no affinity for the RBD RNA binding site, not even when a 16:1 excess of RNase E [583-636] is added to the mixture. In addition, the Dip mutant

does not bind RNase E [756-901], even when a 4:1 excess of the RNase E fragment is added. These results indicate that a double mutation of Glu214 and Glu222 to alanine is sufficient to abolish the interaction between Dip and both RNA binding sites on RNase E, when assessed by mobility shift assays.

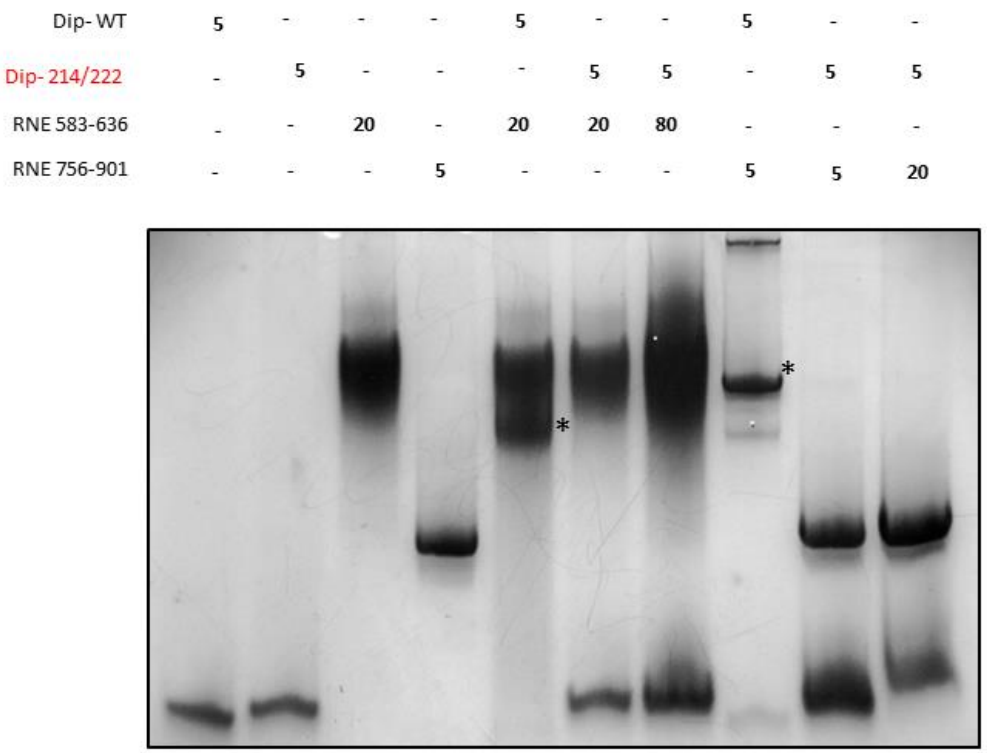

Figure 18: Electrophoretic mobility shift assay of Dip-214/222 and both RNase E [756-907] and RNase E [583-636]. The first four lanes contain wild type Dip, Dip-214/222, RNase E [583-636] and RNase E [756-901], respectively. A clear shift is observed when wild type Dip is mixed with both RNase E targets (lanes 5 and 8, respectively, *). Dip-214/222 has no affinity for RNase E [756-901] and RNase E [583-835] (lanes 6, 7, 9 and 10). Concentrations are presented in µM.

4.1.4. Crystallization experiments validate and elucidate the interaction mechanism

In the previous paragraph, EMSA's were used to validate the predicted binding site on the outer surface of the Dip dimers. To elucidate the interaction mechanism and to verify that the protein fold is still intact in Dip-214/222, crystallization experiments were set up. Like wild type Dip, Dip-214/222 crystalized within 24 hours, when using similar buffer conditions. However, adding 1 mM of DTT and decreasing the crystallization temperature to 4 °C seem to increase the crystal size. Even though the overall hexagonal shape of the Dip-214/222 crystals corresponds to the wild type Dip crystals, the Dip-214/222 crystals have intermittent and cracked edges, whereas wild type crystals have smooth edges (see Figure 19 C-D). A double substitution of Glu214 and Glu222 to alanine seems to be sufficient to introduce significant changes in the crystals.

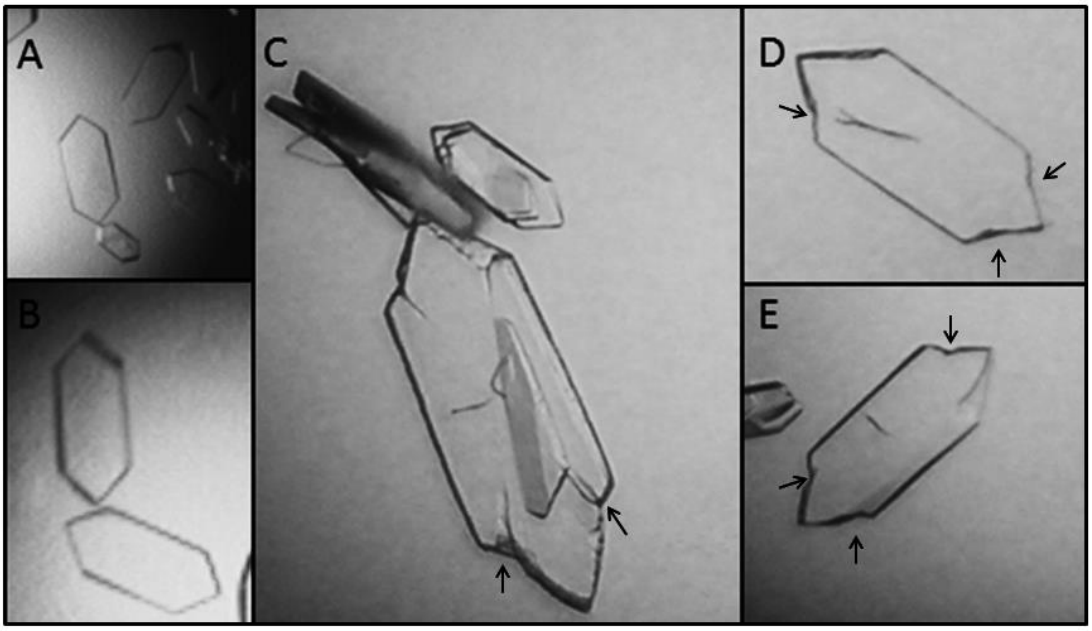

Figure 19: Dip-214/222 crystals have intermittent and cracked edges. A,B: All edges of the hexagonal wild type Dip crystals are equal. C, D, E: The short edges of the Dip-214/222 crystals are intermittent and cracked, as indicated by black arrows.

Datasets were collected for crystals from seven optimized conditions (data not shown). The best diffraction quality was obtained for a Dip-214/222 crystal grown in a buffer of 0.5M NaCl, 1mM GSSG, 1mM GSH, 0.1 M MES pH6.0, 0.1 M NaH_2PO_4, 0.1 M KH_2PO_4 and 0.2 M sodium thiocyanate. After indexing and integration of the raw diffraction-images in IMosflm, the dataset was merged and scaled in Aimless. Finally, the wild type Dip crystal structure was used for molecular replacement in PhaserMR and the crystal structure was solved to a resolution of 2.33 Å. Manual refinement was performed in coot and Refmac5 was used for iterative refinement (see Table 6).

Table 6: Diffraction and refinement statistics for the Dip 214/222 crystal.

Resolution range (Å)	47.29-2.33
Space group	P1 21 1
Unit cell	72.25/64.43/88.41 - 90.00/107.67/90.00
Rmerge (outer shell)	0.241
Rmeas (outer shell)	0.341
Mean I/sd(I) (outer shell)	2.5
Mn (I) half-set correlation CC(1/2) (outer shell)	0.839
Multiplicity (outer shell)	2.2
R-work	0.2334 (0.2787)
R-free	0.2598 (0.2753)
Ramachandran favoured (%)	96.44
Ramachandran outliers (%)	0

The Dip-214/222 crystal structure aligns well to the wild type Dip crystal structure in PYMOL, with a root mean squared deviation (RMSD) of 0.229 nm (see Figure 20 A). However, when the crystal structure of wild type Dip is fitted to the electron density map of Dip-214/222 in Coot, a deficiency in electron density is designated for Glu214 and Glu222, as expected (see Figure 20).

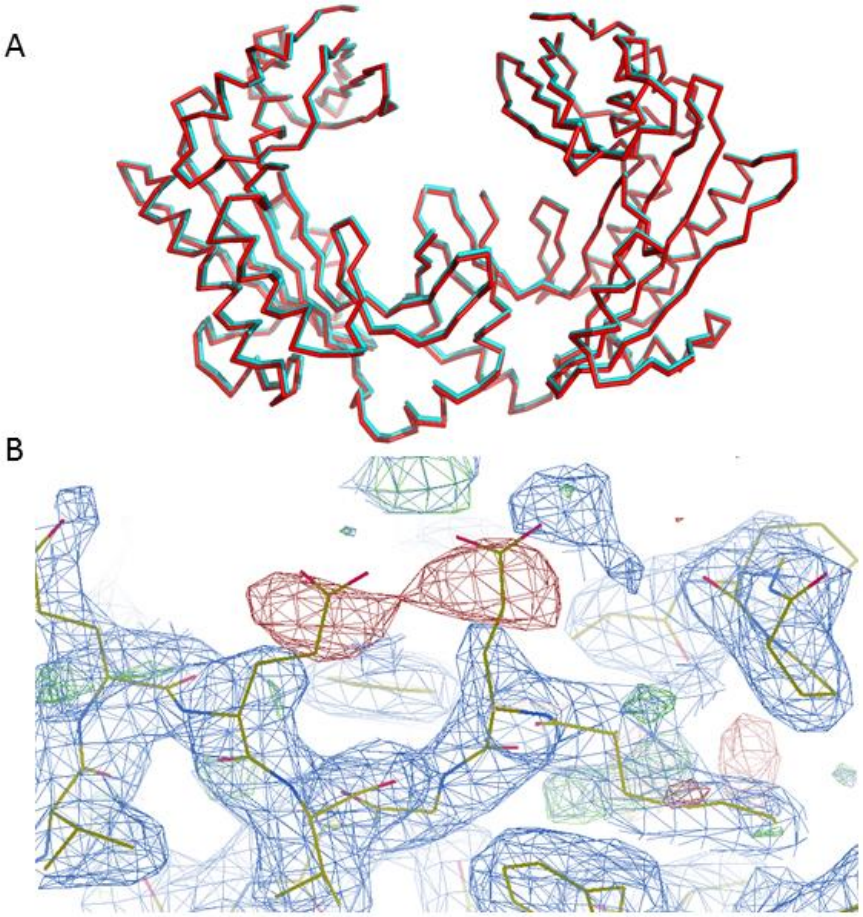

Figure 20: Comparison of Wild type Dip and Dip-214/222 crystal structures. A: Wild type Dip (cyan) and Dip-214/222 (red) align well in PYMOL, with an RMSD of 0.229 nm. No obvious differences in crystal structure were observed between wild type and mutant Dip. B: A difference map of Dip-214/222 electron densities (blue) designates two missing density blobs (red) for Glu214 and Glu222.

To elucidate the interaction mechanism, electrostatic surface potentials of both wild type Dip and Dip-214/222 were calculated with the electrostatic surface extension in coot and the APBS extension in PYMOL (see Figure 21). Wild type Dip has a large acidic patch on its outer surface which co-localizes with the RNase E binding site. Since the RNA binding sites in RNase E, AR2 and RBD, are rich in arginine residues, it is probable that these RNA binding sites dock into the acidic pockets formed by glutamate and aspartate residues on the Dip dimers. This hypothesis is further confirmed when taking into account the electrostatic surface potential of Dip-214/222, where the acidic pocket is disrupted due to the substitution of Glu214 and Glu222 for alanine.

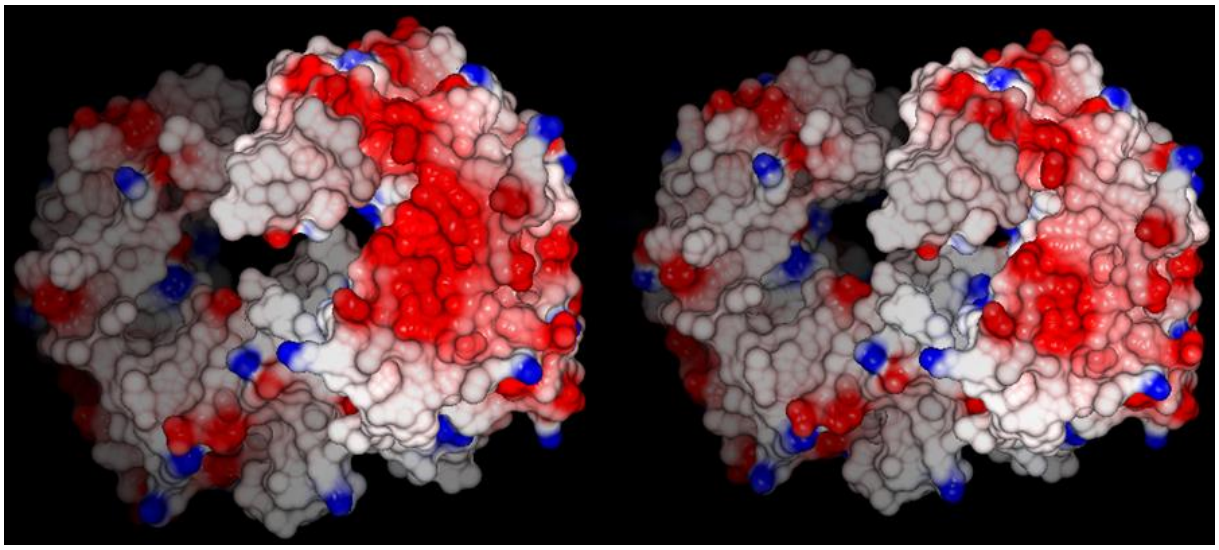

Figure 21: Electrostatic surface representation of wild type Dip and Dip-214/222. Wild type Dip has a large acidic patch on the outer surface of each Dip monomer in the Dip dimer (red), forming and acidic pocket for the RNA binding sites on RNase E (left). In Dip-214/222 however, these negatively charged patches are disrupted due to the double mutation of Glu214 and Glu222 to alanine (right).

The results presented in this section validate and further elucidate the predicted RNase E binding sites by the docking program DOT (see 1.4.2) and the Dip + RNase E [756-775] crystal structure. The arginine rich RNA binding sites on the C-terminal scaffold domain of RNase E bind the acidic patches on the outer surface of the Dip dimer. This way, Dip hijacks both RNA binding sites and thereby prevents long, structured RNAs from binding and being degraded. Even though the interaction mechanism between Dip and RNase E has now been elucidated, the question as to why Dip forms clamp-like dimers remains to be solved. Initially, bio informatics analyses using Metapocket predicted that RNase E would bind the groove of the clamp-like dimer (Van den Bossche, 2015), but the above mutagenesis-, crystallization- and interactomics experiments have disproven this hypothesis. Since each Dip dimer contains two RNase E binding sites on its surface, several binding and stoichiometry models can be proposed. First, one Dip dimer might bind one RNA binding site on the C-terminal scaffold domain of RNase E, leaving one acidic patch unbound. Alternatively, one Dip dimer might bind two RNA binding sites in close proximity to each other in the degradosome, at the same time. Moreover, it is plausible that one single Dip dimer binds to two separate RNase E protomers, especially since RNase E is a tetrameric enzyme (see 1.3.1). Finally, the binding of Dip may actively bring the two RNA binding sites on one RNase E scaffold domain together. In the following two sections the interaction stoichiometry and –model of Dip and the RNase E scaffold domain are further elucidated.

4.2. Investigating the interaction model of Dip and the RNA degradosome

To elucidate the interaction stoichiometry between Dip and the C-terminal scaffold domain of RNase E, RNase E [583-835] was purified by affinity purification and co-purified with Dip by

size-exclusion chromatography. Subsequently, the samples were concentrated to a concentration of 1 mg/ml and subjected to absorbance-based analytical ultracentrifugation to estimate the molar mass of the Dip + RNase E [583-835] complex. In addition, size-exclusion chromatography-multi angle light scattering (SEC-MALS) was used to accurately determine the molar mass of Dip, RNase E [583-835] and Dip + RNase E [583-835].

4.2.1. AUC experiments point towards a mix of two interaction models

The input parameters for data processing and the output parameters are presented in Table 7. The partial specific volume of the protein complex, solvent density and viscosity were calculated using SEDNTERP. To compensate for aggregation and degradation in the sample, molecular weight boundaries were set to 10 kDa and 300 kDa.

Table 7: Input and output parameters for sedimentation velocity measurements.

Input parameters		**Output parameters**	
Partial specific volume (cm^3/g)	0.725	**Frictional ratio**	1.462
Solvent density (g/cm^3)	1.003	**MW first peak (kDa)**	94.179
Solvent viscosity (m^2/s)	0.0101	**MW second peak (kDa)**	182.461

The continuous distribution plot of the calculated molecular mass is presented in Figure 22. Since the rotor temperature was 20°C, some degradation and aggregation were expected. The molecular weight peaks around 10 kDa and 300 kDa correspond to degradation and aggregation, respectively, of the protein species. After integration, a molar mass of 94.2 kDa was calculated for the most abundant protein complex (see Figure 22). This molar mass suggests a complex formed by one Dip dimer and one RNase E [583-835] fragment. Since this RNase E fragment contains both the RBD and AR2 RNA binding site, these data suggest that Dip is able to bind both RNA binding sites within one RNase E scaffold domain, retaining these in close proximity to each other. Such a complex has a predicted molecular weight of 95.2 kDa, which is in accordance with the measurements presented here. However, a second comprehensible peak could be integrated, yielding a molar mass of 182.5 kDa. Even though this complex is less predominant in the sample, the calculated molar mass for this complex is within the 10 % error range of a complex of 2 Dip dimers and two separate RNase E [583-835] fragments, which has a predicted molar mass of 190.4 kDa. These additional data suggest that Dip forms dimers in order to bind two separate RNase E scaffold domains within one RNase E tetramer in the host cell (see Figure 22).

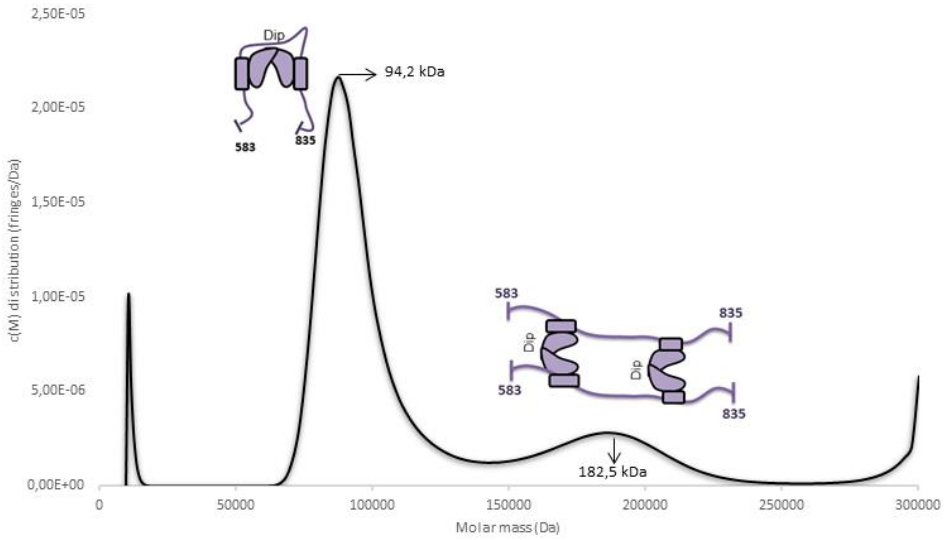

Figure 22: Calculated continuous molecular mass distribution based on the sedimentation velocity of the Dip + RNase E [583-835] concentration boundaries. The most predominant complex in this sample is formed by one Dip dimer which binds both RNA binding sites in one RNase E scaffold domain, with an estimated molar mass of 94.2 kDa. In addition, two Dip dimers could bind two separate RNase E scaffold domains, with an estimated molar mass of 182.5 kDa . Both interaction models are schematically presented in the inset pictures.

The presented AUC results point towards a mixture of two reasonable interaction models between Dip and RNase E. The 1:1 (one Dip dimer binds one RNase E scaffold domain) interaction model seems to be the most predominant one in these samples. Since the RNase E scaffold domain is predicted to be unstructured, it is possible that Dip manages to infer a significant conformational change of the RNase E scaffold domain by binding both RNA binding sites. The frictional ratio, which is a rigorous indication for particle shape, is 1.46 for these measurements (see Table 7). Since a perfect sphere has frictional ratio of 1 , the frictional ratio estimated here suggests a somewhat spherical complex. This indicates that Dip actively folds the scaffold domain by binding both interaction sites, rather than binding only one RNA binding site, which would result in a more elongated complex and a higher frictional ratio. However, molar mass estimates based on size-exclusion chromatograms suggest a complex of at least 180 kDa (data not shown). It is possible that the 2:2 interaction model (two Dip dimers bind two RNase E scaffold domains) is more predominant than indicated by these results. As the experiments were carried out at 20°C, a possible explanation could be that the complex is unstable at room temperature, and dissociates by the centrifugal force. The fact that the continuous molar mass distribution does not drop to zero in between both peaks, supports this hypothesis. Furthermore, the interaction between Dip and the RNA degradosome might be highly transient, which would explain a rather unstable interaction.

4.2.2. SEC-MALS suggest a 2:2 Dip + RNase E [583-835] interaction model

To further elucidate the interaction stoichiometry between Dip and he RNA degradosome, multi-angle scattering was used in combination with size-exclusion chromatography. Therefore, Dip

was purified by affinity chromatography and size-exclusion chromatography and RNase E [583-835] was purified using affinity chromatography. Subsequently Dip and RNase E [583-835] were co-purified using size-exclusion chromatography, and concentrated to 5 mg/ml. SEC-MALS measurements were performed for Dip, RNase E [583-835] and the Dip + RNase E [583-835] complex.

In a first step, Dip was subjected to SEC-MALS to confirm the dimer conformation, as previously measured by AUC. A molar mass of 58.67 ± 0.345 % kDa was calculated from three chromatograms (differential refractive index (DRI), ultra violet (UV) and light scattering (LS)), with high monodispersity across the elution peak (data not shown). Whereas the molar mass of Dip was estimated to be 66.1 kDa based on AUC measurements (Van den Bossche *et al.*, in submission), the SEC-MALS estimate is significantly lower. Degradation of Dip is the most probable cause for this difference, since the sample had been thawed several times for crystallization and SAXS experiments. However, the SEC-MALS estimate for the molar mass confirms the dimeric state of Dip irrevocably.

Next, SEC-MALS was used to estimate the molecular mass of Dip + RNase E [583-835]. Initially a molar mass of 230 ± 2.01% kDa was measured for a fresh sample of Dip + RNase E [583-835] at 5 mg/ml (data not shown). However, as the monodispersity of the sample and the quality of the measurements were poor, a second run was performed, using a one month old sample at 5 mg/ml (see Figure 23 A). As observed in AUC experiments, two complexes were separated during size-exclusion chromatography. For the most predominant complex a molar mass of 110 ± 0.603 % kDa was measured from three chromatograms (DRI, UV and LS) with an acceptable monodispersity across the elution peak. However, since no reasonable interaction model can be linked to this molar mass, it probably results from extensive degradation or dissociation of the complex. For the second complex, a molar mass of 183.3 ± 0.641 % kDa was measured from three chromatograms (DRI, UV and LS) with an acceptable monodispersity across the elution peak (see Figure 23 A). This molar mass corresponds well to a 2:2 interaction model between Dip and RNase E [583-835], with two Dip dimers binding four RNA binding sites on two separate RNase E scaffold domains. Although the observed monodispersity of the samples was acceptable, the samples should be of better quality if one wants to fully use the possibilities inherent to SEC-MALS measurements to accurately determine the molar mass of this protein complex.

Since RNase E forms homotetramer complexes (see 1.3.2) and since both AUC and SEC-MALS suggest a 2:2 interaction model between Dip RNase E [583-835], a possible homodimerisation of RNase E [583-835] was assessed. A first rigorous molecular mass estimate of 60 kDa was obtained by size-exclusion chromatography, suggesting that the RNase E scaffold domain forms dimers, which are then bound by two Dip dimers. Subsequently, SEC-MALS was used for an RNase E [583-835] sample

at 5 mg/ml to assess this dimerization hypothesis (see Figure 23 B). A molecular weight of 33.18 ± 1.462% kDa was measured from three chromatograms (DRI, UV and LS) with an acceptable monodispersity across the elution peak (see Figure 23 B). These measurements disprove the dimerization hypothesis for the RNase E scaffold domain, as the predicted molar mass for the RNase E peptide was 31 kDa.

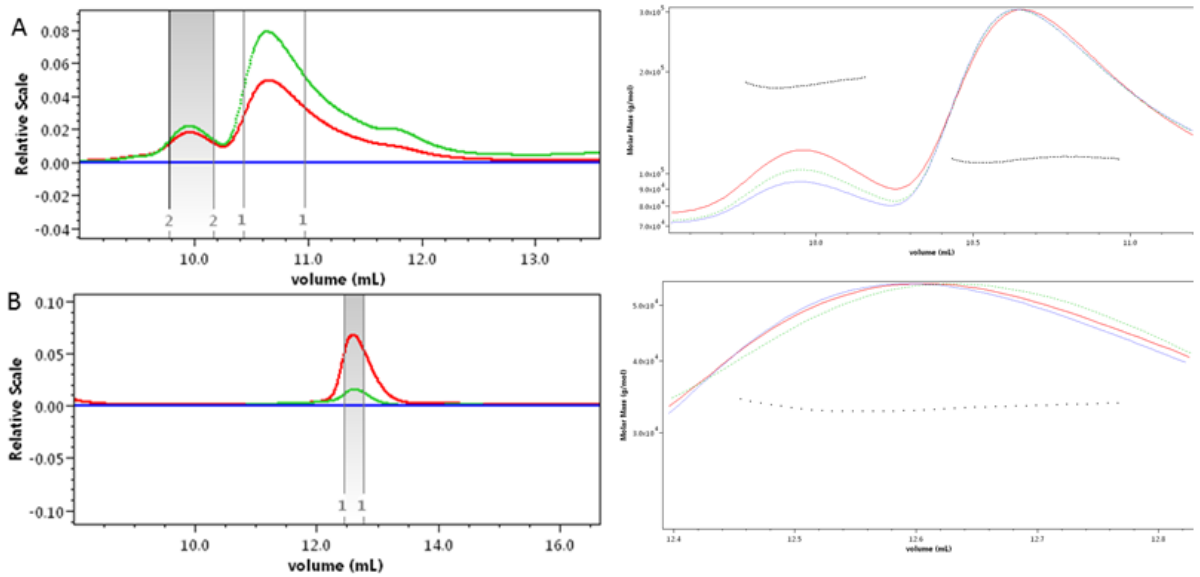

Figure 23: Size-exclusion chromatograms and SEC-MALS measurements for Dip + RNase E [583-835] and RNase E [583-835]. A: SEC-MALS measurements for Dip + RNase E [583-835]. Two main peaks were observed during size-exclusion chromatography and calculation borders for molar mass determination were defined for both peaks, based on their shape (left). After rescaling and alignment of the chromatograms, the molar masses were determined as 110 ± 0.603 % kDa and 183.3 ± 0.641 % kDa for peak one and two, respectively (right). B: SEC-MALS measurements for RNase E [583-835]. A single peak was observed during size-exclusion chromatography and calculation borders were defined based on the peak shape (left). After rescaling and alignment of the chromatograms, the molar mass of RNase E [583-835] was determined as 33.18 ± 1.462% kDa (right). Red, Blue and green curves are light scattering, differential refractive index and ultra violet measurements respectively. Black dotted lines are molar mass profiles across the SEC peaks.

4.3. Dip dimers could oligomerize to mimic duplex RNA and hijack the RNA degradosome

In this section small-angle x-ray scattering experiments were set up to elucidate the conformational flexibility of Dip and compare its structural behavior in solution with the crystal structure. In addition, SAXS datasets were collected for the Dip + RNase E [583-835] complex to obtain a first glimpse of its shape in solution, as well as further elucidate the interaction stoichiometry between Dip and RNase E. Finally, attempts were made to dock a refined Dip crystal structure or assembled Dip construct into low resolution SAXS envelopes of both Dip and Dip + RNase E [583-835].

4.3.1. SAXS models for Dip introduce a plot twist to the story

Even though crystallography is used to obtain detailed structural information for mechanistic analysis, proteins are forced to adopt a low energy conformation within crystal lattices. Therefore, it

is difficult to draw conclusions on a protein fold in solution when only considering crystal structures. A popular approach to cope with this problem is to gather additional structural information by using small-angle X-ray scattering data, since SAXS is a very powerful complementary method to high-resolution techniques. One of the main reasons for the growing popularity of SAXS is that there is no need for well diffracting crystals of the protein (complex) of interest. However, much less appreciated is the fact that scattering data can be collected and processed for any sample, regardless of its quality. Therefore, critical evaluation of the datasets is crucial to devise strong hypotheses from raw scattering profiles and the 3D models that are built from these data. A recent advancement to facilitate quality assessment is to use size-exclusion chromatography immediately before collecting scattering data (SEC-SAXS). As such, aggregation of the protein sample is minimized and the reliability of the scattering data is improved. However, since the resolution of the scattering data is dependent on sample concentration, higher input concentrations are needed to obtain datasets of optimal resolution.

In this section we set out to collect SAXS data for two Dip samples and compare the structural parameters and 3D *ab initio* models with the Dip crystal structure. In addition, the Dip crystal structure is adjusted both manually and with the ATSAS package to improve the fit between the crystal structure and the SAXS models.

4.3.1.1. Sample preparation, data collection and quality assessment

The most important advantage of (SEC-)SAXS over crystallography is its accessibility when it comes to sample preparation, since no crystals are needed. However, monodispersity, purity and high concentration of the sample are crucial to gain reliable and qualitative information from scattering profiles. Therefore, Dip was purified using affinity chromatography and size-exclusion chromatography. Subsequently, sample monodispersity and purity were confirmed using SDS-PAGE (see Figure 15 A). A running buffer of 200 mM NaCl, 20 mM Tris pH 7.5, 1 mM DTT (to avoid disulfide aggregation and minimize radiation damage) and 5% (v/v) glycerol was used for size-exclusion chromatography. Finally, the Dip samples were concentrated to 510 µM (17 mg/ml) and 1.5 mM (50 mg/ml).

To enable buffer subtraction, scattering data of the Dip buffer was collected during column equilibration. During data collection, the radius of gyration (R_g, the root-mean-squared distance of all elemental scattering volumes from their center of mass, weighted by their scattering densities) was monitored across the SEC elution peak as a first quality control (see Figure 24). No obvious aggregation or contamination was observed across the elution peak, which points to a highly

monodisperse and pure sample. Buffer subtraction and data reduction were carried out according to the standard protocol at the beamlines before data processing and are not further discussed here.

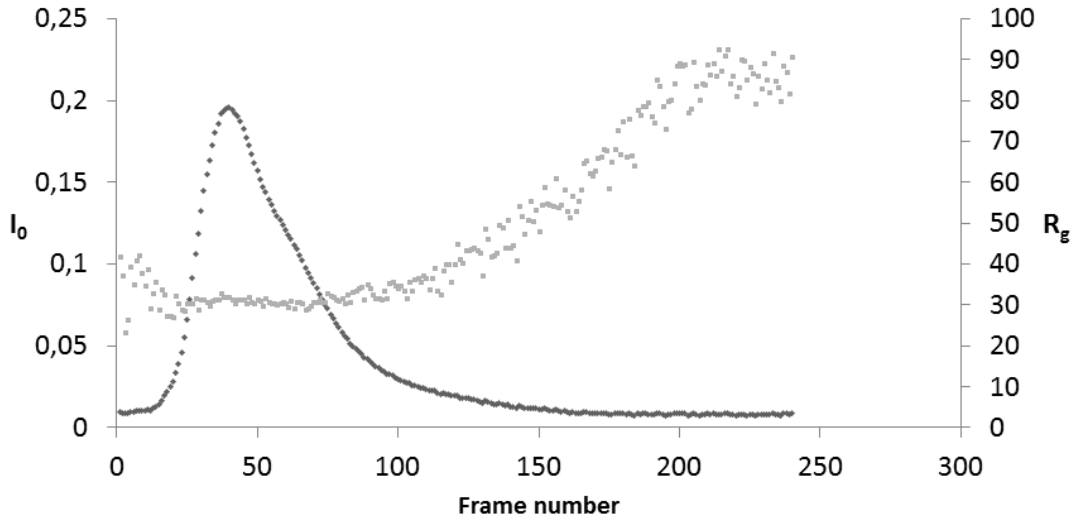

Figure 24: Automated real-time SEC-SAXS data plot for Dip, showing the elution peak and R_g across the elution peak. The elution profile is showing a single peak with a consistent R_g, even though the peak is slightly asymmetric. $I_{0,}$ from Guinier fitting, is shown in black and R_g is shown in grey. The scattering frame number is presented on the x-axis.

4.3.1.2. Initial processing and data validation for Dip

In this section, two SEC-SAXS datasets for Dip will be processed in parallel, with all necessary quality controls. The name Dip17 refers to the lower concentration (17 mg/ml) Dip sample/dataset, whereas Dip50 will be used to refer to the high concentration (50 mg/ml) sample/dataset. The starting point for processing any SEC-SAXS dataset is a 1D curve, where the scatter intensity (I(s)) is a function of the scattering angles (2θ), which is called the scattering profile. The most convenient way to do this, is to plot the logarithm of I versus s, which is a function of half the scattering angle (see Figure 25). From these plots, no noticeable aggregation or inter-particle interference of Dip is observed in the lowest resolution regions (lowest s regions).

Next, a Guinier analysis (ln(I) vs s^2) of the scattering data at very small scattering angles is performed in PRIMUS to further asses particle aggregation and inter-particle interference and to determine R_g (see Figure 26). Both samples obey Guiniers law, as there are no obvious serial 'smiling' or 'frowning' deviations from the line of best fit and the sR_g values do not exceed the value of 1.3 (Feigin & Svergun, 1987; Jacques & Trewhella, 2010). The R_g and I_0, the extrapolated intensity of scattered X-rays through zero angle, which increases with the concentration of the sample and the molar mass of the particle, are presented in Figure 26. The fidelities of the Guinier fits were 0.98 and 0.97 for the Dip17 and Dip50 samples, respectively.

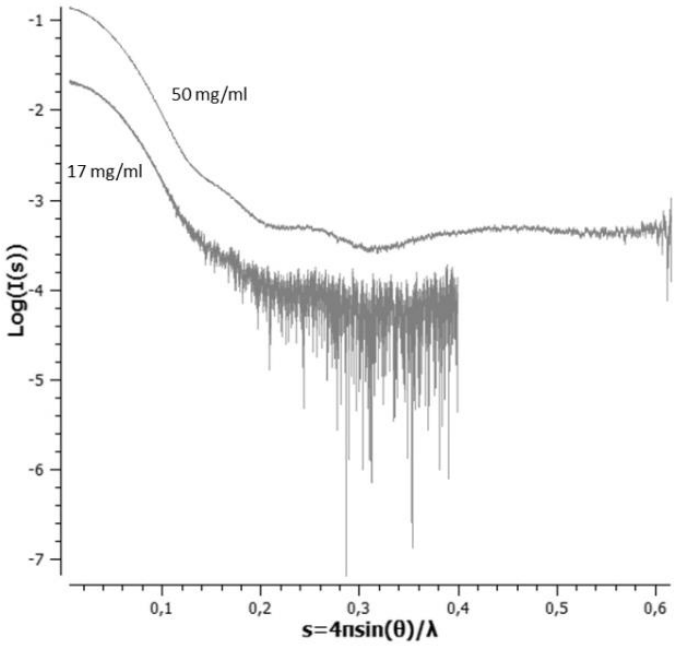

Figure 25: Intensity of the scattered X-rays as a function of the scattering angle for Dip. S is a function of λ, the wavelength of the incident radiation, and θ, half the angle between the incident and scattered X-rays. Higher s regions on the x-axis correspond to higher resolution data (as in crystallography) and thus a lower signal to noise ratios. The concentrations of the injected samples for SEC are presented with the corresponding intensity curves.

Subsequently, the pair distance distribution function, which is a distribution function (P(r)) of all interatomic distances (r) within one Dip dimer, was calculated for both samples with GNOM. This distribution function is the Fourier transform of the scattering profile (see Figure 25). Furthermore, as mentioned in section 3.7, the P(r) function is the radially averaged equivalent of the Patterson function in crystallography. Accordingly, estimates for the longest linear distance over a Dip dimer, D_{max}, were made (see Figure 26) (Jacques & Trewhella, 2010). For both P(r) functions, the plot approaches zero in a smooth, concave way at D_{max}, which indicates that there is no obvious aggregation or inter-particle interference and that the chosen D_{max} approximates the real D_{max}. Furthermore, the R_g and I_0 estimates from the pair distribution function correspond well to those from the Guinier fit. These estimates are more reliable than the Guinier estimates, since all scattering data is taken into account. As aggregation mostly affects the lowest resolution regions (low s values), this agreement of independent R_g and I_0 estimates suggest that there is no aggregation in the Dip samples. As expected from the crystal structure, the Dip dimers seem to be rather globular, as indicated by the single peaks in the distribution function and the rather short tails at D_{max}, which further indicates that Dip does not have multiple flexibly tethered domains. From the calculated Porod volume, which is an averaged value for the particle volume, rigorous molecular weight ranges were estimated. The expected molar mass of 63.2 kDa for one Dip dimer is well within range of the estimates for both datasets (see Figure 26).

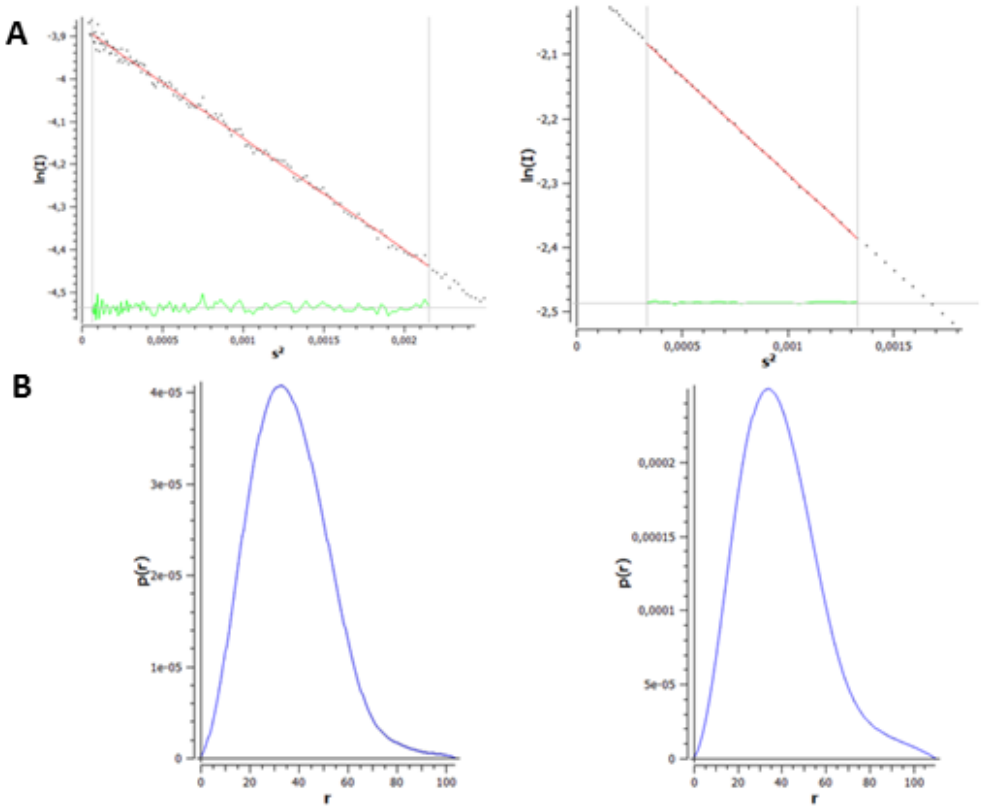

C

Sample	Dip17	Dip50
Concentration (mg/ml)	17	50
I_0 (Guinier)	0.021	0.14
I_0 (P(r))	0.02	0.14
R_g (Å, Guinier)	28.01	30.21
R_g (Å, P(r))	28.19	30.73
D_{max} (Å)	104	110
MW range (kDa)	54.2-63.5	59.5-68.0

Figure 26: Overview of Guinier approximation, pair distribution function and structural parameters. A: The Guinier approximation for both the Dip17 (left) and Dip50 (right) datasets are highly linear and show no signs of aggregation or inter-particle interference. B: Pair distribution functions of the Dip17 (left) and Dip50 (right) datasets suggest globular particles, as expected from the Dip crystal structure. C: Summary of structural parameters for both datasets. I_0: scatter intensity at zero angle; R_g: radius of gyration; D_{max}, longest linear distance over a Dip dimer.

Surprisingly, there is a slight difference in the calculated R_g and D_{max} values for both samples. Even though the Guinier plot for the Dip50 sample is almost perfectly linear and the P(r) behaves properly, the somewhat higher R_g and D_{max} values might indicate some subtle multimerization of Dip in this sample. After all, not only had the sample been thawed previously, a concentration of 50 mg/ml is exceptionally high and aggregation could be expected as soon as DTT oxidizes in the buffer. Alternatively, the observed variation could be due to inherent structural flexibility of the Dip dimer,

which complicates proper R_g and D_{max} estimations (Jacques & Trewhella, 2010). Finally, buffer over subtraction before processing could cause subtle differences in R_g and D_{max}. However, given the high quality of the elution profile for the Dip50 sample and the rather small deviations in R_g and I_0, only small errors in *ab initio* models are expected. Nevertheless, the Dip17 dataset will be used for modelling efforts primarily.

To confirm the folded state of the Dip samples and to obtain information about the dynamic state of Dip, as well as its flexibility, a Kratky plot ($I(s)*s^2$ vs s) was generated (see Figure 27). Both datasets have a clear peak in the low s region, which is specific to fully folded, globular proteins. Since the Kratky curve is not descending to zero after the peak, flexible regions might be present in the Dip dimer. However, the Kratky plot for the Dip17 sample approaches that of an ideally spherical particle, as the tail is close to zero.

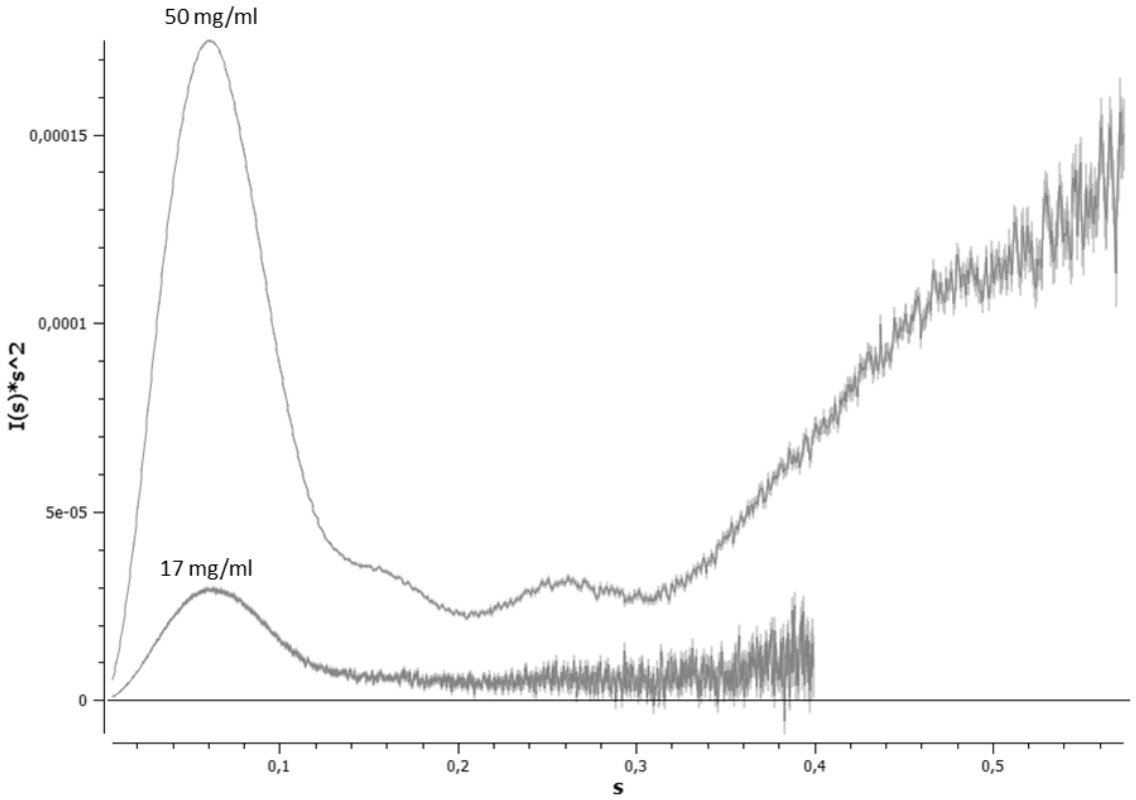

Figure 27: Kratky plots for both Dip datasets. I(s)*s^2 (y- axis) is plotted as a function of s (x-axis).The peaks in the low s regions indicate that Dip is predominantly structured and globular in both samples. Since the Kratky curves don't descend to zero after the peak, some flexible regions might be present in the Dip dimers.

4.3.1.3. How to make the Dip crystal structure fit the SAXS data: different approaches with similar outcomes

As mentioned before, SAXS is a powerful technique when used to refine high resolution data. The R_g of the Dip crystal structure is 28.64 Å, as inferred from the theoretical scattering profile generated in CRYSOL, which is slightly higher than 28.19 Å, as calculated for the Dip17 dataset. Next, CRYSOL was used to fit the theoretical scattering profile for the crystal structure of Dip to the experimental

scattering profile of the Dip17 sample. In parallel, a theoretical scattering profile was calculated and fitted to experimental profile with the much faster FoXS server (see Table 8). The fits were unexpectedly poor, which points towards significant structural differences between the crystal structure and the solution structure of Dip. From now on, 'apo Dip' will be used to refer to the initial crystal structure of Dip.

To find possible structural rearrangements of the Dip structure, a normal mode analysis was performed on Dip with the Bio3D extension in R (Grant *et al.*, 2006) (see Figure 28). As suggested by this normal mode analysis, Dip can adopt more 'open' or more 'closed' conformations, with the dimer interface serving as a hinge. In addition, previous structural analysis of the dimeric Dip structure in DynDom, suggest residues V133 and Y238 act as potential mechanical hinges, which allow for rotation of one monomer in relation to the other (Van den Bossche, 2015).

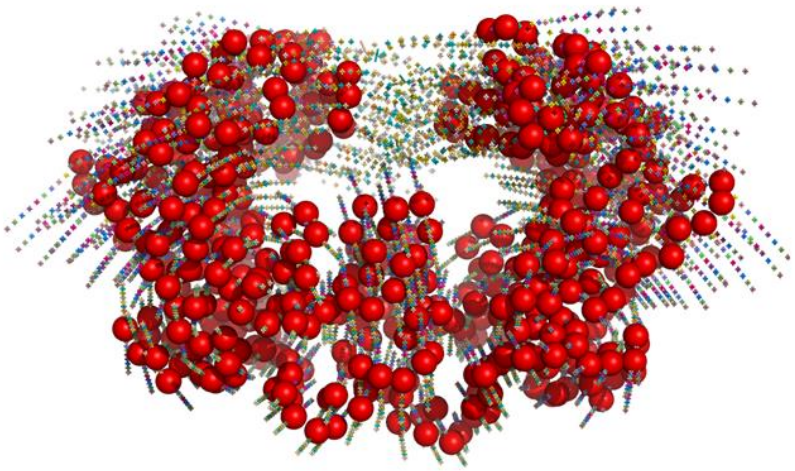

Figure 28: Normal mode analysis of the Dimeric Dip structure using Bio3D. Dip has both open and closed conformations, as indicated by the colored triangular dots. The apo structure of Dip is presented in red spheres.

To generate an adjusted Dip dimer which would better fit the scattering data, i.e. better fit the solution structure for Dip, an iterative approach of manual adjustments in PYMOL was used. First, 5° rotations of one monomer in relation to the other were imposed about the predicted mechanical hinge, and this over a range of 180° degrees. Each conformer was fitted to the experimental scattering data using FoXS and CRYSOL. The best improvement of fit is observed for a rotation of 60° (Dipα, see Table 8). In a second iterative round of refinement, the Dipα structure was compacted over a fixed axis, conform the normal mode analysis. The best fit (Dipβ, see Table 8) was subjected to a final round of refining, by compacting the structure over a second fixed axis, conform the normal mode analysis (DipϒY, see Table 8). This way the goodness of fit between the crystal structure and the solution structure improved 5.19x according to CRYSOL and 2.15x according to FoXS (see Figure 29). In Parallel, Dr. Nathan Cowieson (Diamond lightsource) performed the same procedure independently. The resulting Dip dimer has a very similar shape as DipϒY but with an inter-monomer

angle of only 35° and was less compacted (data not shown). The resulting goodness of fit values (χ^2=2.38 in FoXS and χ^2=1.88 in CRYSOL), however, are similar to those for DipϒY (see Table 8).

Table 8: Goodness of fit scores (χ^2) for theoretical scattering profiles against the experimental scattering profile of Dip, before and after structural refinement.

Dip conformer	CRYSOL	FoXS	R_g
Apo Dip	16.05	3.10	28.64
Dipα	8.32	2.47	28.04
Dipβ	5.69	1.84	27.80
DipϒY	3.09	1.44	27.51
AdjDip	1.87	1.90	27.01

Although the results presented in Table 8 have a significantly improved goodness of fit to the scattering data, the method is not scientifically justified. During the manual iterative refinement process no steric clashes were taken into account, which raises questions on the validity of the results. Therefore, SReflex was used to iteratively refine the Dip crystal structure against the scattering data. Sreflex performs iterative normal mode analysis on specific subdomains to generate pools of Dip conformers, while minimalizing steric clashes and limiting structural breaks. The libraries of conformers were then screened against the SAXS data with CRYSOL, after which the best fits, with minimal steric clashes, were selected. From this sub-library of conformers a series of structures was chosen manually (with a goodness of fit ranging from χ^2=1.79 to χ^2=2.98) and evaluated in PYMOL for structural breaks. Surprisingly, all conformers suggested by SReflex have a twisted and compacted dimeric structure, similar to the manually refined structures. Based on the goodness of fit and the number of steric clashes, one adjusted Dip (AdjDip) was chosen as a best realistic fit (see Figure 29). For this structure, a χ^2 of 1.87 against the scattering data and only two steric clashes were reported, whereas a χ^2 of 1.90 is calculated with FoXS (see Table 8). Furthermore, the 'twist' among the individual monomers seems to be smaller than initially thought, with an inter-monomer angle of approximately 40°. Either way, the fit of AdjDip against the scattering data for Dip has improved 6.7x according to CRYSOL and 1.7x according to FoXS. Therefore it is plausible that a twisted dimeric structure of Dip is a realistic representation of its solution structure. This hypothesis is further strengthened by independent rigid body modeling efforts against the Dip17 scattering profile, which is briefly presented in appendix 2.

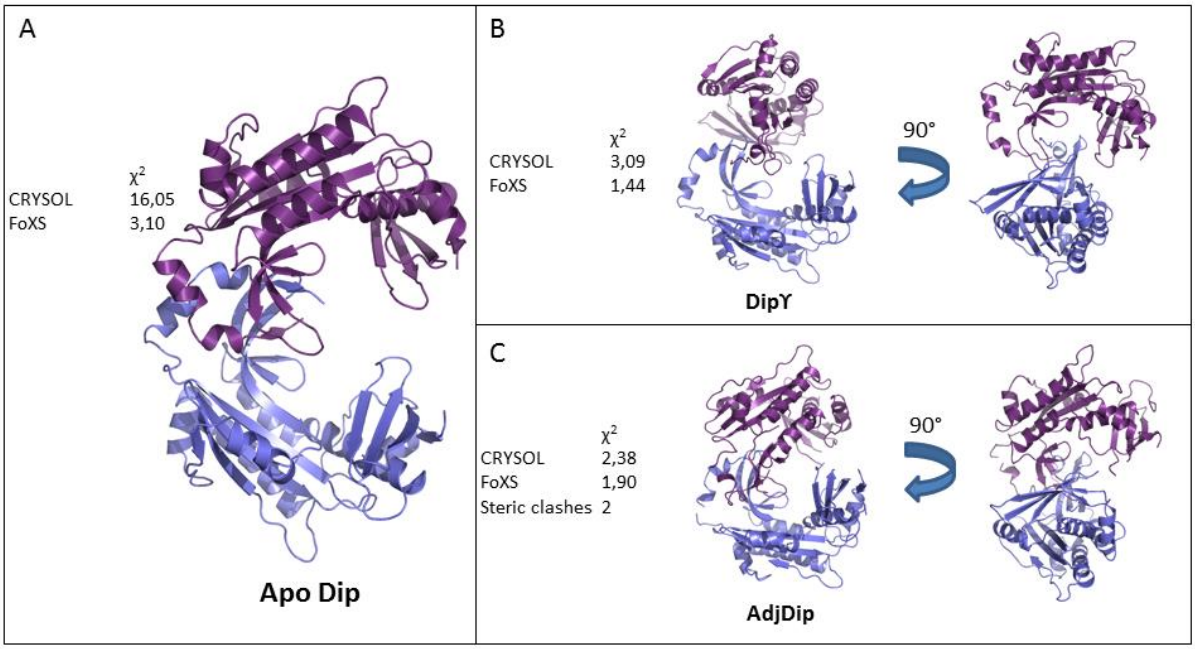

Figure 29: Schematic overview of apo Dip and the best fitting Dip conformers, generated either manually or with SReflex. A: The apo structure of Dip does not correspond with the solution structure of Dip, as suggested by both CRYSOL and FoXS. B: The iteratively refined DipϒY conformer, based on normal mode analysis and a predicted mechanical hinge, fits the scattering data much better than the apo Dip structure, as suggested by both CRYSOL and FoXS. C: SReflex was used to generate a realistic conformer which represents the solution structure of Dip with significant confidence, as suggested by both CRYSOL and FoXS.

4.3.1.4. The twisted and compacted Dip can be docked into SAXS envelopes

To test the validity of the proposed Dip conformer AdjDip, low resolution *ab initio* models were built based on the scattering data for both Dip samples. Initially, DAMMIF was utilized to generate sets of 15 *ab initio* models for the Dip17 dataset, starting from the raw SAXS profiles and the parameters defined in Figure 26. Subsequently, the DAMAVER program suite was employed to align all *ab initio* models and choose the most typical one (Damsel), then align all *ab initio* models with the most typical one (Damsup), average these aligned models and compute a probability map for each dummy residue (Damaver) and finally filter an averaged model from this probability map (Damfilt) (see Table 4). Next, these averaged models were converted to low resolution envelopes in PYMOL for docking simulations with SUPALM. SUPALM invokes a spherical harmonics representation to superimpose one 3D structure onto another. As such apo Dip, DipϒY and AdjDip were docked into these envelopes and the fit was evaluated by means of a normalized integral cross-term coefficient, NCT, which tends to 1 for ideally superimposed objects. In addition, Damstart (DAMAVER program suite) was used to generate an input model with a fixed core from the averaged Damfilt model. DAMMIN was then employed to generate a refined model, starting from this input model. Additional docking simulations were performed with these refined DAMMIN models, but no improvement of superimposition was observed, so these results will not be discussed here.

In parallel, low resolution models based on both Dip datasets were generated with GASBOR, which incorporates scattering data from higher s regions, and thus higher resolution regions. Instead of presenting an extended overview of all models built with GASBOR, DAMMIF and DAMMIN, a selection of the best models are presented and superimposed with apo Dip and mainly AdjDip (see Figure 30). For all DAMMIF models, the scattering profile was trimmed to $s=8/R_g$, one of the few well known thumb rules for *ab initio* modeling. As discussed before, the Dip17 scattering data served as a starting point for the *ab initio* model building. However, additional GASBOR models were built with the Dip50 dataset, since the high resolution region for this dataset is subject to very little noise.

In the first instance, Damfilt models with twofold symmetry were built for the Dip17 dataset, according to the protocol presented in the previous paragraph. Next, apo Dip was docked in these Damfilt models, resulting in a best fit of NCT=0.868 (data not shown). Even though apo Dip did not fit the scattering data according to calculations with CRYSOL (χ^2=16.05) and FoXS (χ^2=3.10) (see Figure 26), a rather high NCT value was calculated. Since DAMMIF models, and thus Damfilt models as well, only consider the lowest resolution regions (which correspond to the longest distances within a Dip particle) no clamp-like structure could be distinguished in these Damfilt models (see Figure 30 A). To assess the adjustments imposed on the apo Dip crystal structure by SReflex, AdjDip was superimposed on the same *ab initio* model. With a calculated NCT of 0.891, there is only a small improvement of the superimposition compared to the superimposition with apo Dip (see Figure 30 A). Since no clamp-like conformation can be recognized in the Damfilt model, little difference should be expected between the apo Dip and AdjDip fits, since both of these are globular proteins. Both fits are of good quality, as suggested by the NCT values. In Figure 30 A however, the superimposition of AdjDip in the Damfilt envelope does not appear optimal, despite the good NCT value, as the AdjDip structure protrudes the Damfilt envelope at several places. These results suggest that it is hard to distinguish between the 'right' and 'wrong' Dip conformers when solely using DAMMIF/Damfilt models for Dip. Therefore, several GASBOR models with twofold symmetry were built based on the Dip17 dataset and evaluated visually as well as based on their goodness of fit, χ^2, against the raw scattering data. As GASBOR tries to incorporate high resolution scattering data in the model, both long and short intra-particle distances are modelled during the annealing process. Furthermore, GASBOR reckons with protein behavior during simulation steps. In most GASBOR models a clear dimeric and twisted clamp-like conformation is distinguishable (data not shown).

The apo Dip crystal structure was superimposed to best GASBOR envelope in terms of goodness of fit to the scattering data (χ^2=1.54). As the resolution of this *ab initio* model is better, the superimposition with apo Dip is of lower quality, with NCT=0.810 (see Figure 30 B). In parallel, AdjDip was superimposed to the same GASBOR envelope, with NCT= 0.932 (see Figure 30 C). From these

results it is clear that AdjDip is a better representation of the solution structure than apo Dip, as its fit to the GASBOR envelope is better both visually and in terms of NCT values.

During quality assessment of the Dip50 scattering data, signs of multimerization artefacts in the corresponding sample were observed (see 4.3.1.2). Therefore, higher error rates will be introduced during *ab initio* model building. However, as presented in Figure 25, the scattering profile for the Dip50 sample reaches out to s=0.6 $Å^{-1}$ without tremendous decrease in signal to noise ratios. Since s=0.6 $Å^{-1}$ is the theoretical maximum for SAXS experiments, and corresponds to a resolution of approximately 10 Å, GASBOR models were generated for this scattering profile as well. Unfortunately, the χ^2 values, which represent how well the GASBOR models fit the scattering profile, for these *ab initio* models ranged from 50 to 100, which might be a direct consequence of multimerization artefacts. Alternatively, GASBOR might have difficulties to accurately model the highest resolution data. Despite the poor fits of the *ab initio* models to the scattering data, most models display a clear twisted dimeric shape. In addition, since some aggregation was present in the sample, the average size of one Dip dimer tends to be overestimated during *ab initio* modelling. However, in GASBOR the number of dummy residues was fixed at 512, which corresponds to one Dip dimer. Therefore GASBOR might have difficulties when annealing these dummy residues in a model which is too small according to the scattering data. The best GASBOR model, which had a χ^2 of 56.7, was chosen for docking simulations.

Subsequently, SReflex was used to adjust the apo Dip structure according to the Dip50 scattering profile by performing extensive normal mode analysis and minimizing the steric clashes. The resulting structures were all twisted Dip dimers, but were less compact compared to AdjDip (see Figure 30 D). To assess the validity of these structures, CRYSOL was employed to calculate a theoretical scattering profile and fit this profile to the experimental Dip17 scattering profile. Despite the subtle aggregation observed for the Dip50 scattering profile, a best χ^2 value of 3.9 was calculated, which is significantly better than for apo Dip, with χ^2=16.05. Moreover, this adjusted Dip dimer, AdjDip2, has no steric clashes. Next, AdjDip2 was superimposed to the GASBOR envelope in SUPALM, with NCT=0.893 (See Figure 30 D). In parallel, apo Dip was superimposed to the same envelope with NCT= 0.803 (data not shown). As expected, the GASBOR envelope is somewhat oversized with respect to AdjDip2. Even though the GASBOR *ab initio* model had poor χ^2 values, the superimposition of AdjDip2 is of decent quality, both visually and according to the NCT value. Especially the pincers of AdjDip2 seem to accurately fit the GASBOR envelope.

The *ab initio* modelling efforts and superimposition simulations, together with the structural refinements imposed by SReflex, strongly suggest that the hypothetical twisted and compact Dip

dimer is a valid representation of the solution structure. However, since Dip forms rather flexible dimeric conformations (see Figure 27), structural rearrangements could occur when binding the RNase E scaffold domain. Moreover, the implications of the hypothesized solution structure towards possible oligomerization when binding its target are uncertain. In the next section SEC-SAXS is used to further elucidate this oligomerization state as well as the interaction model between Dip and the RNase E scaffold domain.

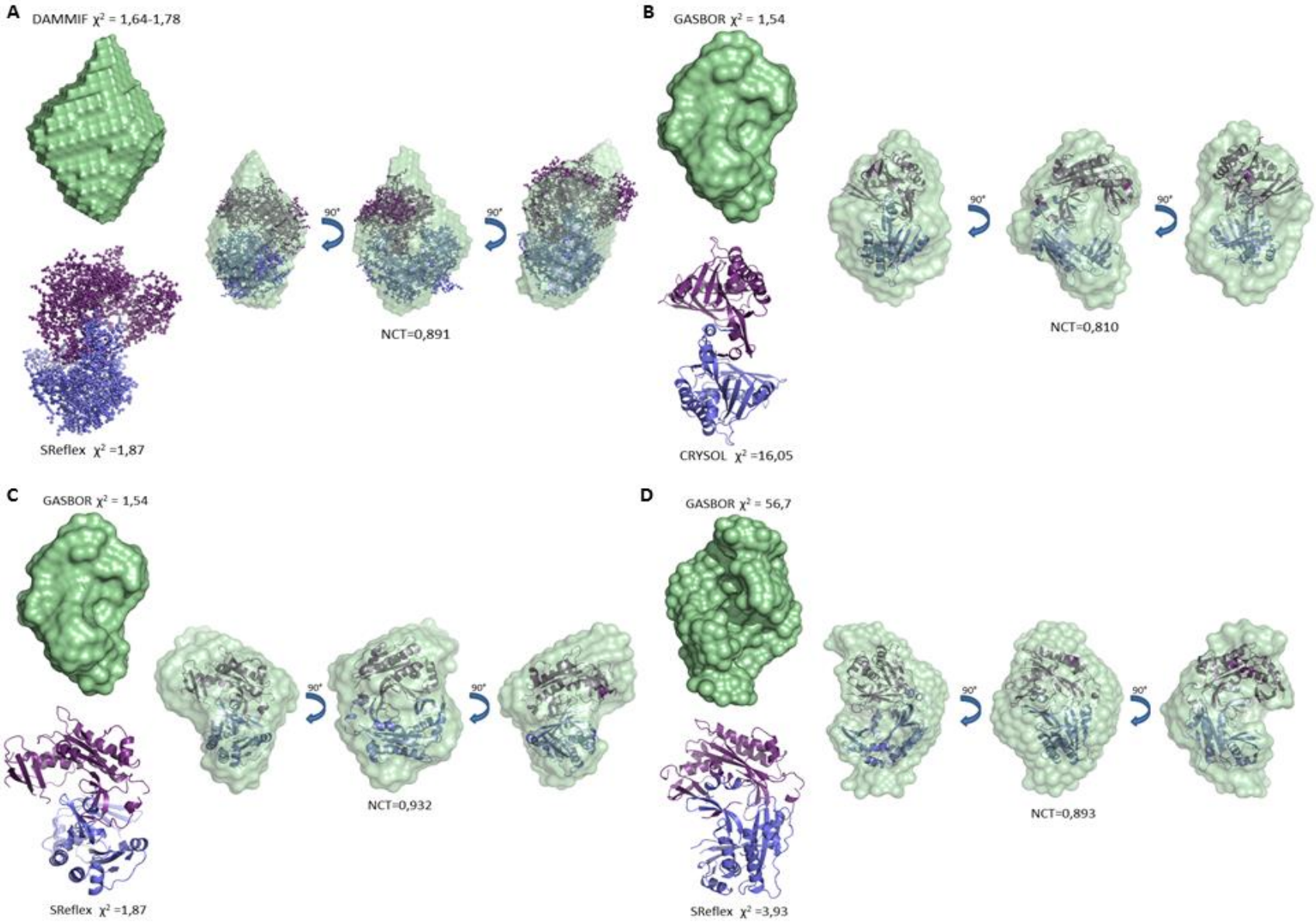

Figure 30: Overview of *ab initio* modelling efforts and superimposition simulations. A: *Ab initio* modeling based on the Dip17 scattering profile with DAMMIF and the DAMAVER program suite and subsequent superimposition of AdjDip. AdjDip is represented in as dummy beads for docking into Damfilt envelopes. B: *Ab initio* modeling based on the Dip17 scattering profile with GASBOR and subsequent superimposition of apo Dip. C: The same GASBOR model as in B was used for superimposition of AdjDip. D: *Ab initio* modeling based on the Dip50 scattering profile with GASBOR and subsequent superimposition of AdjDip2. For each of four sections in this figure, the *ab initio* model is presented upper left together with the χ^2 value for its fit to the scattering data. Likewise, the adjusted crystal structure is presented bottom left, together with the χ^2 value for the fit of the theoretical scatter profile to the experimental scatter profile, as calculated by CRYSOL. All Dip structures are presented with the dimer ridge up front. The superimposition of the Dip conformers are presented from left to right in each section, together with the NCT value.

4.3.2. SAXS measurements support a higher order and helical Dip complex when bound to RNase E: a first member of the bacteriophage-encoded RNA mimicry?

Following the molar mass estimates based on AUC and SEC-MALS measurements (see 4.2.2) extensive co-crystallization screens were set up for co-purified complexes of Dip + RNase E [583-835] and Dip + RNase E [583-636]. Although it was hoped to obtain high resolution insights in the interaction model between Dip and RNase E, no concrete results were obtained from these crystallization trials. Since many crystals of Dip alone were obtained, it is plausible that the assemblies are highly transient and that Dip crystalizes as soon as the complexes dissociate. Therefore, they will not be discussed here, but a brief overview of the co-purification, the obtained crystals and the crystallization conditions is given in appendix 3. In this paragraph, SEC-SAXS is used to further elucidate the interaction model between Dip and RNase E and to obtain a low resolution model for this complex.

4.3.2.1. Sample preparation, data collection and quality assessment

Dip was co-purified with RNase E [583-835] by affinity chromatography and size-exclusion chromatography. The purity of the samples was assessed by SDS-PAGE (see appendix 3). An optimized buffer of 200 mM NaCl, 20 mM Tris pH 7.5, 1 mM DTT and 5% (v/v) glycerol was used for all purification steps. Finally, the Dip + RNase E [583-835] samples were concentrated to 10 mg/ml, since precipitation occurred for higher concentrations. Two of these samples were used at two different synchrotrons (Diamond lightsource and Soleil) for SEC-SAXS data collection.

R_g was monitored across the SEC elution peak, during data collection, as a first quality control (data not shown). No obvious aggregation or contamination was observed across the elution peak, which points to a highly monodisperse and pure sample. Buffer subtraction and data reduction were carried out according to the standard protocol at the beamlines, before data processing, and are not further discussed here.

4.3.2.2. Initial processing and data validation for Dip + RNase E [583-835]

In this section two SEC-SAXS datasets for Dip + RNase E [583-835] will be processed in parallel with all necessary quality controls. The samples and corresponding scattering data will be addressed as DipR1, for the first Dip + RNase E [583-835] sample (Diamond lightsource) and DipR2, for the second Dip + RNase E [583-835] sample (Soleil) (see Figure 31). The scattering profiles for both DipR1 and DipR2 are presented in Figure 31. From these profiles, no noticeable aggregation or inter-particle interference of Dip is observed in the lowest resolution regions. However, the overall scatter

intensity for DipR2 is significantly higher than for DipR1, whereas the sample concentration is the same. Since these data were collected at two different synchrotrons with different beam intensities, it is plausible that the scaling of the overall scattering plot is different. Moreover, different columns were used for SEC prior to X-ray irradiation, which results in different dilution rates.

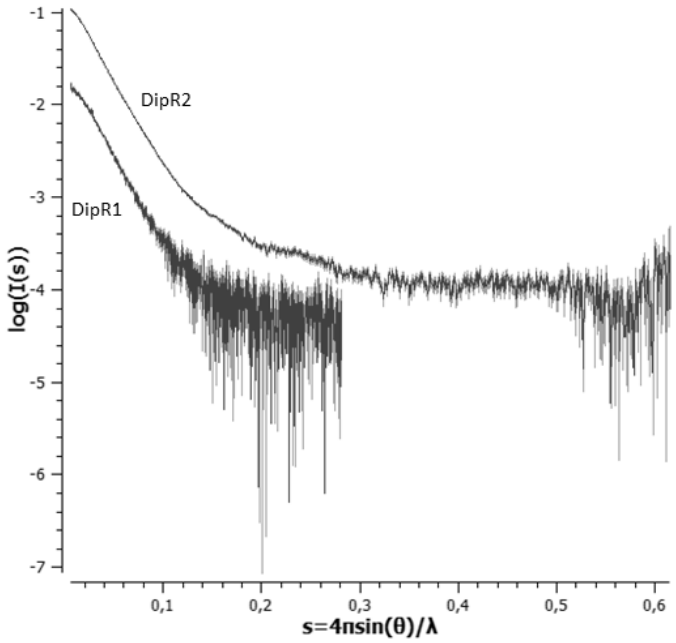

Figure 31: Intensity of the scattered X-rays as a function of the scattering angle for DipR1 and DipR2. S is a function of λ, the wavelength of the incident radiation, and θ, half the angle between the incident and scattered X-rays. Higher s regions correspond to higher resolution data (as in crystallography) and lower signal to noise ratios. Both datasets were collected from samples with a concentration of 10 mg/ml.

Guinier analyses were used to assess particle aggregation and inter-particle interference for both samples. Neither of both datasets show signs of severe aggregation, since a good linearity is observed at the lowest scattering angles (see appendix 4). Moreover, the sR_g limits are well in range. R_g and I_0 values are presented in Figure 32. The fidelities of the Guinier fits were 0.93 and 0.88 for the DipR1 and DipR2 samples, respectively. Subsequently, the pair distance distribution function (P(r)) of both scattering profiles was calculated with GNOM. Accordingly D_{max} was estimated. For both P(r) functions, the plot approaches zero in a smooth, concave way at D_{max}, which indicates that there is no obvious aggregation or inter-particle interference. However the pair distribution function for the DipR1 scattering profiles has a rather bumpy tail, which points towards elongated, multi-domain particles. Furthermore, the R_g and I_0 estimates from the pair distribution function are significantly higher than those estimated by the Guinier fit (see Figure 32). Again, since GNOM takes into account the whole scattering profile for its calculations, these estimates are more reliable than the Guinier estimates. From the calculated Porod volume, rigorous molecular weight ranges were estimated (see Figure 32). These molar mass ranges are similar, although they are both above the molar mass for a 2:2 complex 190.4 kDa, as predicted by AUC and SEC-MALS. This could be due to subtle aggregation

in both samples. Alternatively, a yet unknown interaction model may be predominant in these samples. In any case, the molar mass for the 1:1 interaction model between Dip and RNase E, which was suggested by AUC in section 4.2.1, is far below these molar mass ranges.

As was the case in paragraph 4.3.1.2, the R_g and D_{max} values are higher for the DipR2 dataset, which might indicate that there is some subtle aggregation in the corresponding sample. This sample, however, was old and had been thawed before. Furthermore, most of the DTT in the buffer might be oxidized. The aggregation will cause errors, albeit small, during *ab initio* modelling. Therefore, the DipR1 will be used for *ab initio* modelling primarily.

A

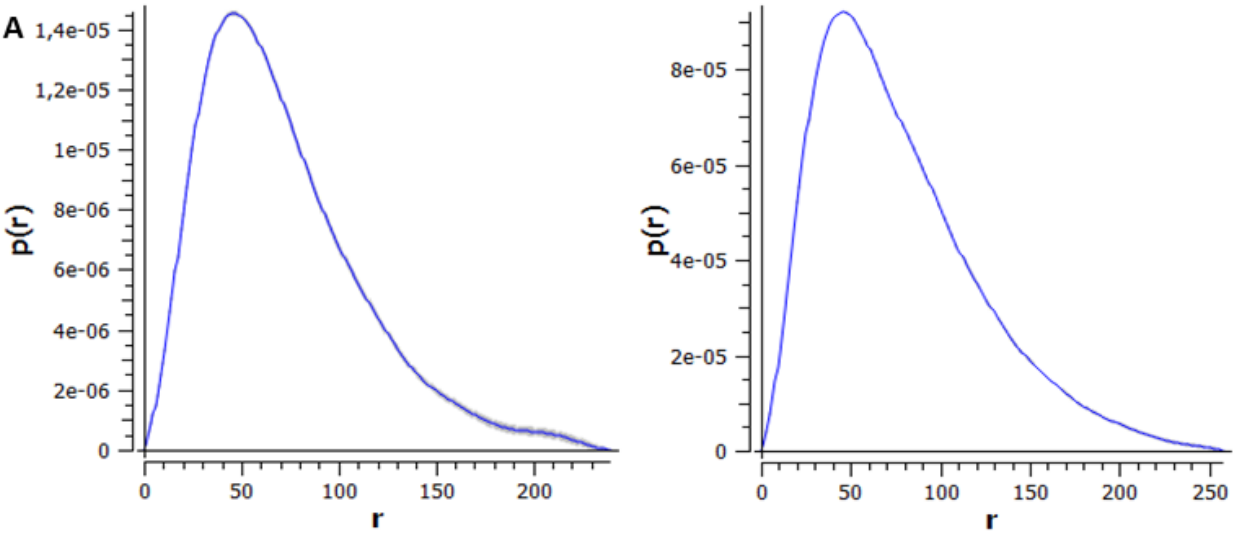

B

Sample	DipR1	DipR2
Concentration (mg/ml)	10	10
I_0 (Guinier)	0.015	0.11
I_0 (P(r))	0.02	0.11
R_g (Å, Guinier)	54.01	59.23
R_g (Å, P(r))	58.15	62.72
D_{max} (Å)	245	258
MW range (kDa)	195.9-220.1	198.9-225.4

Figure 32: Overview of the distribution function and structural parameters. A: Pair distribution functions for the DipR1 (left) and DipR2 (right) datasets suggest elongated, multi domain particles. B: Summary of structural parameters for both datasets. Estimates for I_0 and R_g from the pair distribution function are more reliable, since all data is taken into account.

A Kratky plot was used to confirm the folded state of the DipR samples and to obtain information about the dynamic state and flexibility of the Dip + RNase E [583-835] complex (see Figure 32). Both datasets have a peak in the low s region, which suggests the complex is mainly folded. However, since the Kratky curve is not descending to zero after the peak, some flexible or unstructured regions might be present in the complex.

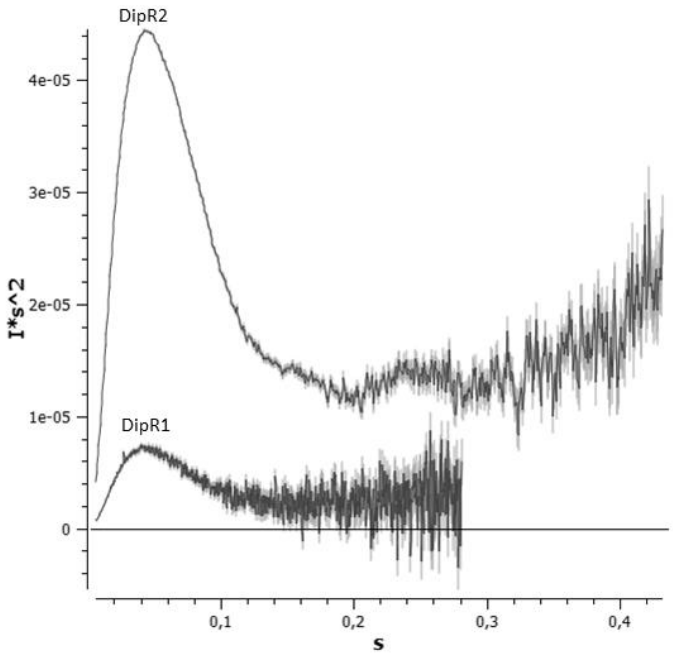

Figure 33: Kratky plots for both DipR datasets. I(s)*s^2 (y-axis) is plotted as a function of s (x-axis).The peaks in the low s regions indicate that the complexes are is predominantly structured. Since the Kratky curves don't descend to zero after the peak, some flexible or unstructured regions might be present in the Dip complexes.

4.3.2.3. Crystallography, SEC-MALS and ab initio models suggest Dip assembles into helical multimers upon binding of RNase E.

As mentioned in the previous paragraph, the molar mass ranges for both datasets are above the expected molar mass of a 2:2 complex of Dip and RNase E, 190.4 kDa. Moreover, the upper limits of both molar mass ranges approach the value of 230 kDa which was initially measured with SEC-MALS (see 4.2.2, data not shown). A meaningful interaction model which approaches this molar mass would contain three Dip dimers and two RNase E [583-835] fragments, with an estimated molar mass of 253.5 kDa. One Dip dimer would therefore not interact with the RNase E fragment, since only two target sites have been identified on the RNase E scaffold domain (see 1.4.2) (see Figure 39 C). However, the crystal structure of Dip + RNase E [756-775] consisted of a condensed helical trimer of Dip dimers in the unit cell (see 4.1.2 and Figure 14 B and C). Therefore, the theoretical scattering profile for the Dip + RNase E [756-775] crystal structure was calculated and fit to the experimental scattering profile of Dip + RNase E [583-835], with χ^2= 5.88 in FoXS and χ^2= 19.6 in CRYSOL. This poor fit might be due to the fact that Dip + RNase E [583-35] was predicted to be elongated (see 4.3.2.2), whereas the Dip + RNase E [756-775] crystal structure has a condensed helical shape. In addition, the complex used for SEC-SAXS measurements contains a larger RNase E fragment (RNase E [583-835], 32.1 kDa) than the complex used for co-crystallization experiments (RNase E [756-775], 2.8 kDa).

Interestingly, the P(r) function for the DipR1 dataset has some features similar to the P(r) function of a B-DNA strand, such as a long tail with little 'bumps' (personal communication with Dr. Nathan

Cowieson and Dr. Robert Rambo, Diamond lightsource; Putnam *et al.*, 2007). Therefore, an intermediary Dip structure from the manual Dip refinement with respect to the SAXS data (see 4.3.1.3) was used to generate a helical trimer of Dip dimers in PYMOL (see Figure 33A). This intermediary Dip structure is a twisted (60°) Dip dimer, Dipα, which has not been compacted and fits the SAXS data for Dip with χ^2= 2.47, according to FoXS (see Table 8). The helical trimer of Dip dimers fits the DipR1 scattering profile with χ^2= 1.93 in FoXS and χ^2=3.09 in CRYSOL, which is a significant improvement compared to the Dip + RNase E [756-775] crystal structure. However, this model is highly speculative, since it is very hard to predict the conformational changes of Dip upon binding RNase E. Furthermore, this helical trimer of dimers was assembled in a very rigorous way, without accounting for steric clashes.

Subsequently, Damfilt *ab initio* models with twofold symmetry, since an even number of Dip monomers and RNase E fragments make up the interaction model, and no symmetry were built according to the protocol explained in paragraph 4.3.1.4 (see Figure 34 B). In parallel, a series GASBOR *ab initio* models with twofold and no symmetry were generated (see Figure 34 C). To test the 'helical trimer of dimers' hypothesis, the number of dummy residues was adjusted to that of a theoretical 3:2 interaction model, i.e. three dimers of Dip bound to two RNase [583-835] fragments. All generated models have thick, rod-like shapes, whereas some models even tend to adopt a spiraling conformation. The low χ^2 values not only indicate that GASBOR has no difficulties fitting the inserted number of residues in an *ab initio* model based on the DipR1 scattering profile, but also that the imposed twofold symmetry doesn't decrease the goodness of fit.

No density has been accounted for RNase E [583-835] in the 'helical trimer of Dip dimers' structure, whereas this density is incorporated in the *ab initio* models. In all GASBOR models with twofold symmetry, an obvious density 'blob' is present in the center. Moreover, two RNase E [583-835] fragments could bind the 'helical trimer of Dip dimers'. Also, approximately 150 residues constitute the link between the two Dip target sites on RNase E, i.e. the RNA binding sites. Therefore, it is plausible that the outer Dip dimers in the helix bind the RNA binding site of the RNase E scaffold domain, whereas the middle Dip dimer plays a structural role in the oligomerization of Dip upon target binding (see Figure 39).

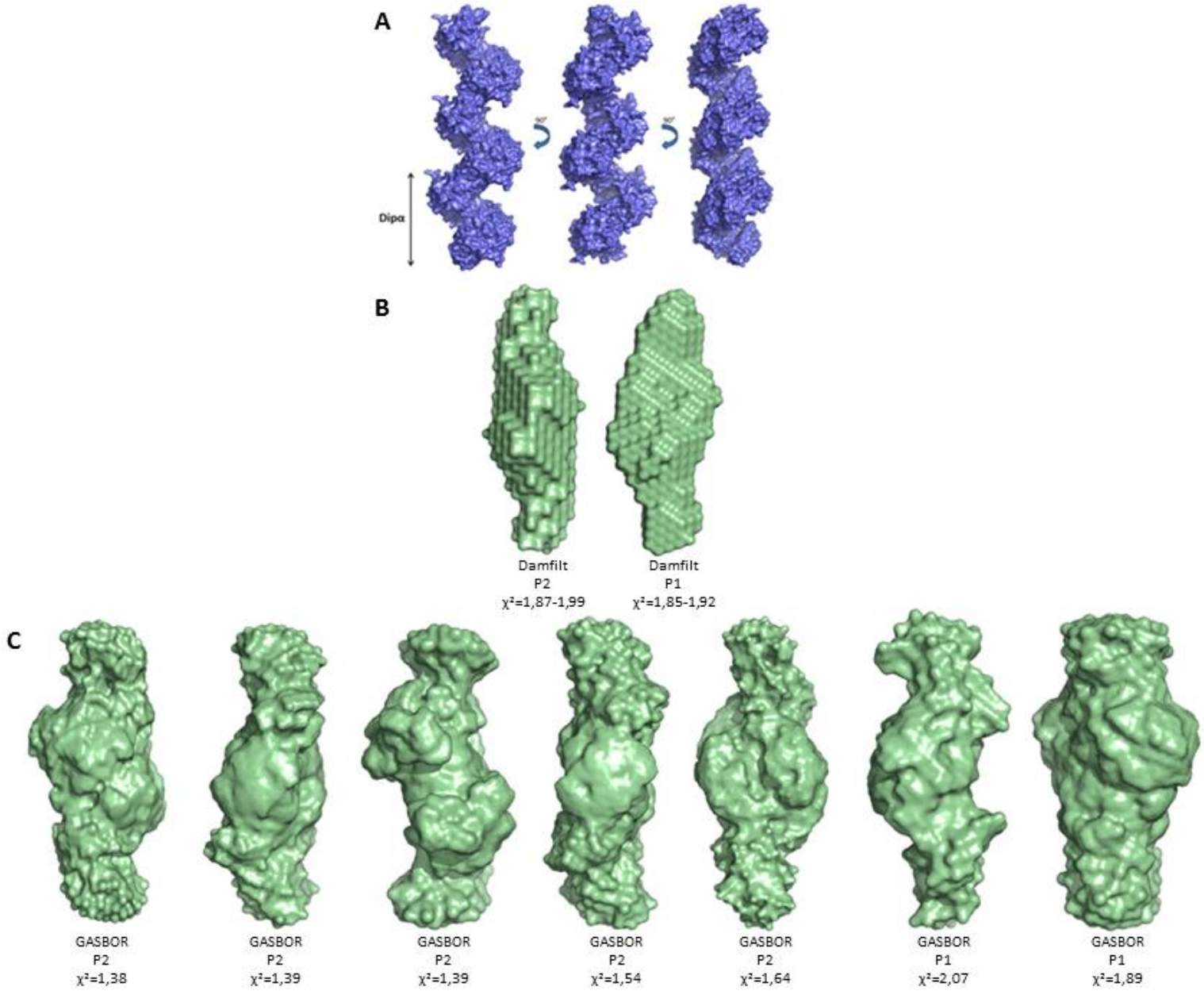

Figure 34: Overview of the helical trimer of Dip dimers and *ab initio* modeling efforts. A: A highly speculative helical trimer of Dip dimers was generated in PYMOL. The size of one Dipα dimer is indicated by a double arrow. B: *Ab initio* models with twofold symmetry and without symmetry were built in DAMMIF and averaged with the DAMAVER program suite. C: Several *ab initio* models with twofold symmetry and without symmetry were generated in GASBOR. All *ab initio* models have a thick rod-like shape, whereas the models with twofold symmetry tend to spiral. P1: no symmetry was imposed during *ab initio* modeling; P2: twofold symmetry was imposed during *ab initio* modeling. χ^2 values for Damfilt models are represented as the range of values for the initial DAMMIF models. The *ab initio* models are not presented to scale.

Since no crystal structure is available for Dip + RNase E[583-835], the 'helical trimer of Dip dimers' was superimposed to Damfilt and GASBOR models with SUPALM (see Figure 35). However, this hypothetical structure does not account for the bound RNase E fragments. Therefore, these superimpositions only serve as a tool to better understand the *ab initio* models and the NCT values should not be considered as strict parameters for the goodness of fit. The helix was superimposed on a Damfilt *ab initio* model with twofold symmetry, and on two GASBOR *ab initio* models with twofold symmetry (see Figure 35). The helical structure protrudes several edges of the Damfilt model (see Figure 35 A), whereas this is not the case for the GASBOR models (see Figure 35 B and C). Furthermore, both the longitudinal and cross sectional size of the helical structure correspond well to those of the *ab initio* models. Even though the superimpositions are incomplete, since the densities for the RNase E fragments are unaccounted for in the helical structure, these results strengthen the 'helical trimer of Dip dimers'. In addition, a rigid body modelling approach was used to further asses this hypothesis. Therefore, three Dipα dimers were assembled into a trimer of dimers in SASREF, according to the DipR1 scattering profile (see appendix 5). Although a helical complex could not be assembled with SASREF, these rigid body modelling efforts further add to the validity of the 'helical trimer of Dip dimers' hypothesis.

Even though the 'helical trimer of Dip dimers' hypothesis is still highly speculative, it is conceivable to hypothesize that Dip would assemble into a helical complex upon binding the RNase E scaffold domain. In section 1.2.2, a series of examples were given of bacteriophage-encoded DNA mimicry, which deceive their target by mimicking the intended binding partner, DNA. Ocr from bacteriophage T7 ,for example, mimics B-DNA to hijack the DNA binding sites on host restriction enzymes. This way Ocr protects T7 DNA from degradation. In accordance to Ocr, Dip might mimic an RNA duplex to increase its chances of hijacking RNase E. Therefore, Dip might be the first known member of a class of bacteriophage-encoded RNA mimicry.

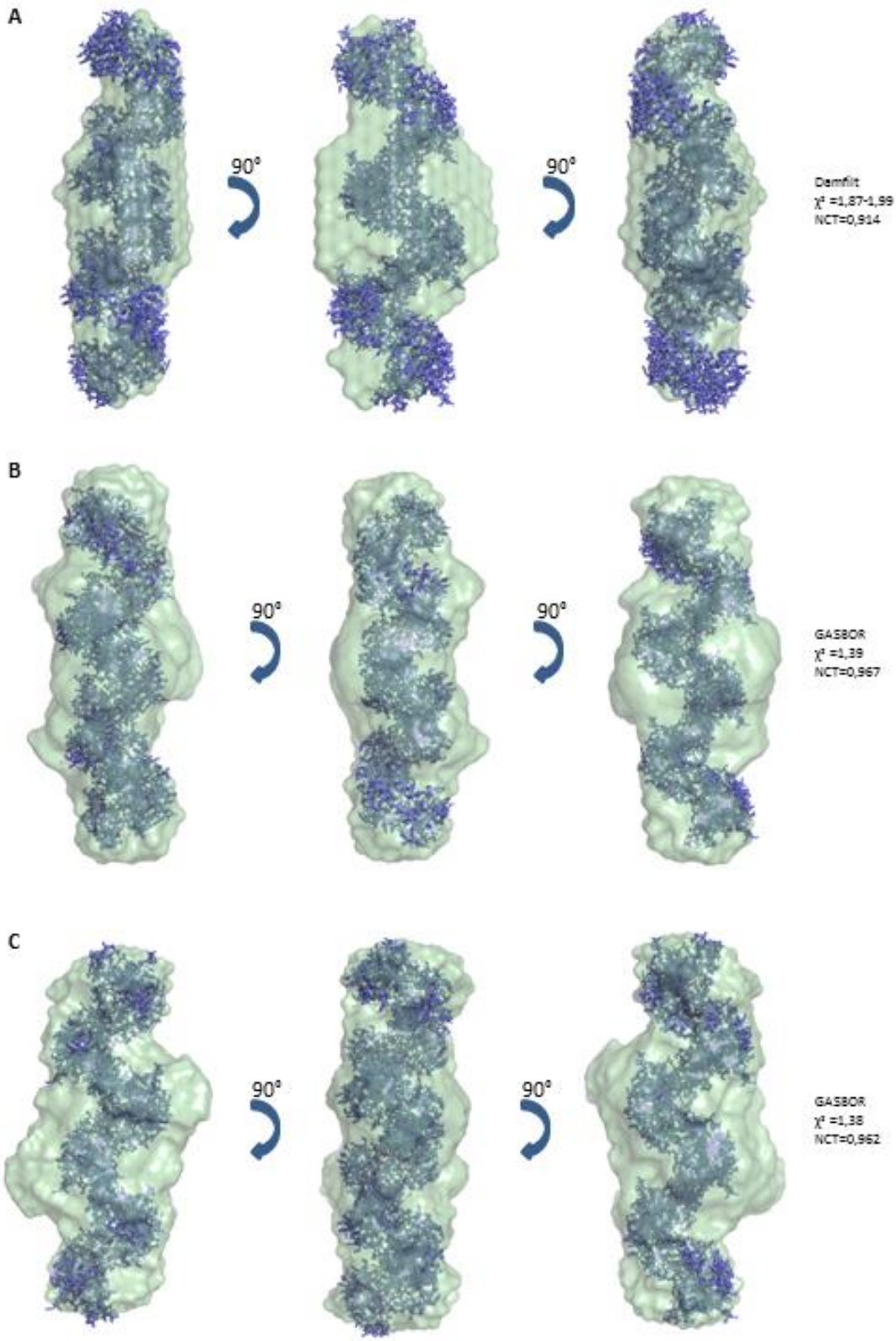

Figure 35: Overview of the superimposed 'helical trimer of dimers' in the *ab initio* models. A: The helical structure is superimposed in a Damfilt model with twofold symmetry. B,C: Next, the helix is superimposed in two GASBOR models with twofold symmetry, which improves the fit both visually and as suggested by the NCT value. The goodness of fit of the *ab initio* model against the DipR1 scattering data (χ^2) and the NCT values are depicted for each superimposition simulation.

However, as for every hypothesis, some open questions remain to be solved. First of all, when Dip would mimic duplex RNA, its size parameters should correspond to those of RNA duplexes. All current members of the DNA mimicry are monomeric or dimeric and have molecular weights around 15 kDa. Dip, however, has a molecular weight of 31.6 kDa and would assemble into a multimer of at least 180 kDa, given that further multimerization upon target binding might happen in the cell. Therefore, it is rather unrealistic to claim that Dip is effective at mimicking RNA duplexes without knowing the exact shape and size of the complex, as well as the charge distribution on its surface. Since crystallization screens did not provide any specific results in this regard, cryo-EM should be used to obtain a high resolution map of Dip in complex with (a part of) the RNA degradosome (see 4.3.3). Secondly, if Dip assembles into a helical oligomer upon binding of RNase E, it could further multimerize to 'infinite length'. However the SAXS models presented here suggest a helical trimer of dimers. On the other hand, RNase E is a tetramer and is predicted to form a dense network at the inner cell surface of *P. aeruginosa*. Therefore, Dip might oligomerize upon binding of RNase E and form long helical, RNA duplex-mimicking rods which co-localize with RNase E on the inner side of the plasma membrane. To further asses the 'helical trimer of dimers' hypothesis, experiments were initialized to fuse Dip with EGFP and visualize its intracellular localization and multimerization state in *P. aeruginosa* cells. Finally, there are some unresolved timing issues as to when Dip decides to oligomerize and form a higher order assembly. Crystallization experiments with Dip + RNase E [583-835] indicate that the interaction between Dip and RNase E is highly transient (see 4.3.2 and appendix 3). Furthermore, AUC and SEC-MALS measurements further strengthen this assumption (see 4.2). Moreover, SAXS measurements on highly concentrated Dip samples reveal multimer artefacts without obvious aggregation. Therefore it is possible that Dip assembles spontaneously into highly unstable oligomers in the cell, which are somewhat stabilized upon binding of RNase E. Alternatively, Dip could oligomerize upon binding of RNase E. Either way, it is worthwhile looking into these timing and hypothetical oligomerization aspects.

4.3.3. Cryo-EM to the rescue?

To test the hypothesis of a helical assembly of Dip in complex with RNase E, the first steps towards a high resolution cryo-EM structure of Dip in complex with the *E. coli* ternary complex were taken. The *E. coli* ternary complex is a multicomponent complex consisting of RNase [583-901], the RhIB helicase and Enolase (available at the lab of professor Ben Luisi, see Figure 36). Therefore, Dip and the ternary complex were co-purified with size-exclusion chromatography (see Figure 36). A running buffer of 200 mM NaCl, 20 mM Tris pH 7.5 and 1 mM DTT was used. This complex has an estimated mass of 426 kDa to 489 kDa, depending on the interaction model, which is large enough for cryo-EM

experiments. Subsequently, the sample was co-purified to a concentration of 5 mg/ml, which corresponds to 34.7 µM when a 2:2 interaction model would form in the sample.

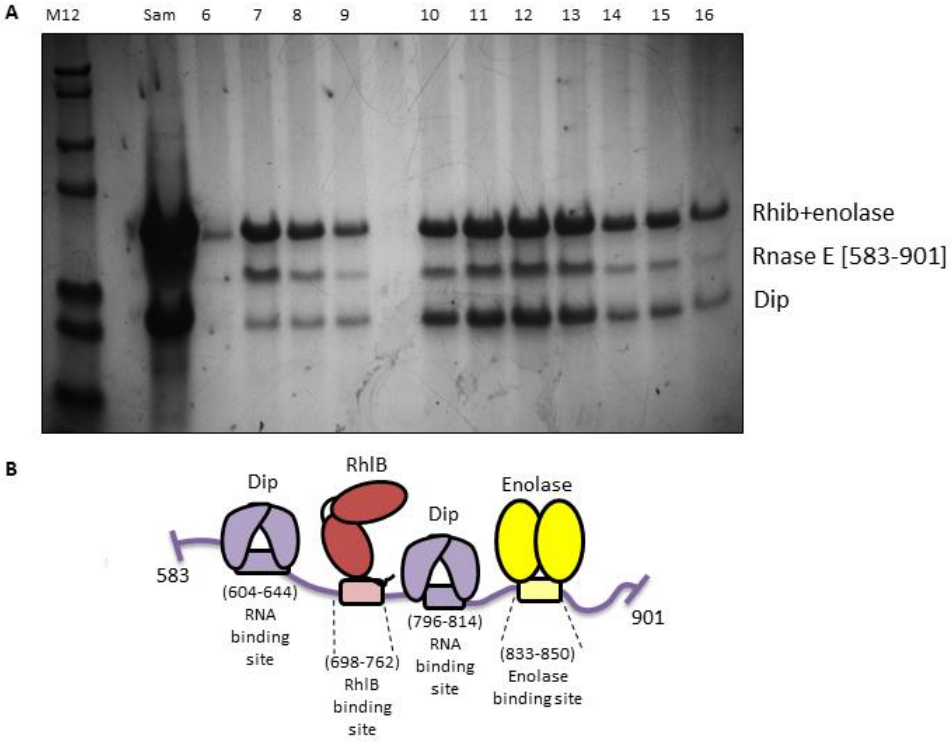

Figure 36: Co-purification of Dip and the *E. coli* ternary complex. A: SDS-PAGE gel of the elution fractions after size-exclusion chromatography. Fractions 6 to 9 contain the void volume. M12, molecular weight ladder; Sam, injected sample. B: Schematic representation of a hypothetical interaction model with two Dip dimers bound to one ternary complex.

Carbon coated copper grids were prepared with several dilutions of this the complex and screened with transmission electron microscopy (see Figure 37). At a concentration of 1 µM there is an ideal spacing of the particles without obvious aggregation. Furthermore, the particles are uniform, which points towards a pure and monodisperse sample. The particle size of approximately 30 nm corresponds well to what could be expected for a complex of Dip and the ternary complex. Despite the low resolution of the images, the particles look globular, whereas elongated particles were expected based on the *ab initio* models from GASBOR and Damfilt (see 4.3.1.4). However, the globular shape of the particles could be due to a space-filling effect of the RhIB and Enolase components in the complex. Since these preliminary screens look promising, grids for cryo-EM will be prepared and screened. This way, a high resolution map of the complex could be obtained to solve the interaction model problem between Dip and RNase E of the *P. aeruginosa* degradosome.

Finally, SEC-SAXS was used to obtain an initial low resolution map for this complex, which could facilitate the processing of cryo-EM datasets. The elution profile looked promising, with a constant R_g across the elution peak. Unfortunately, an error occured during data transfer at the synchrotron and has left the dataset unavailable. Therefore, these results can't be discussed here.

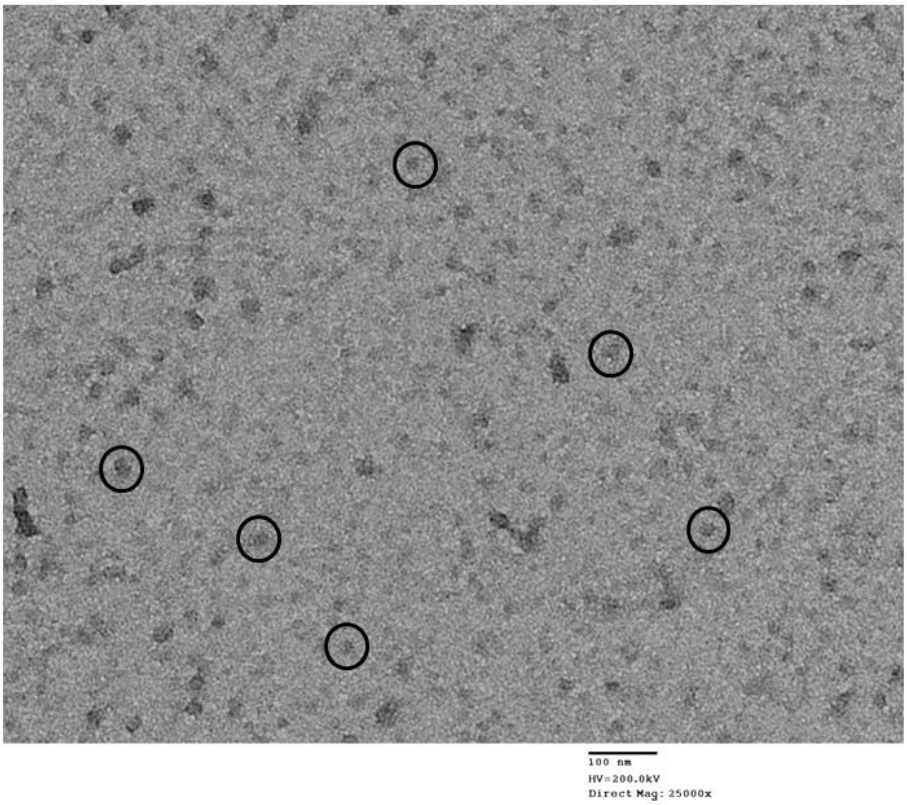

Figure 37: EM screen of Dip + ternary complex at 1 µM. Some particles are highlighted with black circles. Overall, the particles are not aggregated, have uniform sizes and have an ideal spacing. A scale bar, voltage and direct magnification are presented at the bottom.

4.4 Dip is persistent during phiKZ infection

Since Dip protects phiKZ RNA from degradation by the RNA degradosome one would imagine that, once produced, Dip engages RNase E for the remainder of the phage infection cycle and persistently inhibits the RNA degradosome. RNA seq. experiments have shown that Dip is mainly produced during the early phase of infection (personal communication with Bob Blasdel; Ceyssens *et al.*, 2014) (see Figure 38 B). In this section, Western blot experiments were used to evaluate whether Dip protein persists in the cell during later stages of the bacteriophage infection. Therefore, phage infection was halted every three minutes during a single infection cycle and Dip was detected with a total antibody mix of two rabbits who were immunized with highly purified Dip. In parallel, culture OD's were monitored to ensure that all bacteria were infected at the onset of phage infection. For each detected Dip band the intensity and number of pixels were counted in ImageJ and normalized against a purified Dip sample (positive control) (see Figure 38). Three biological replicas were carried out, as well as mechanic replicas if needed.

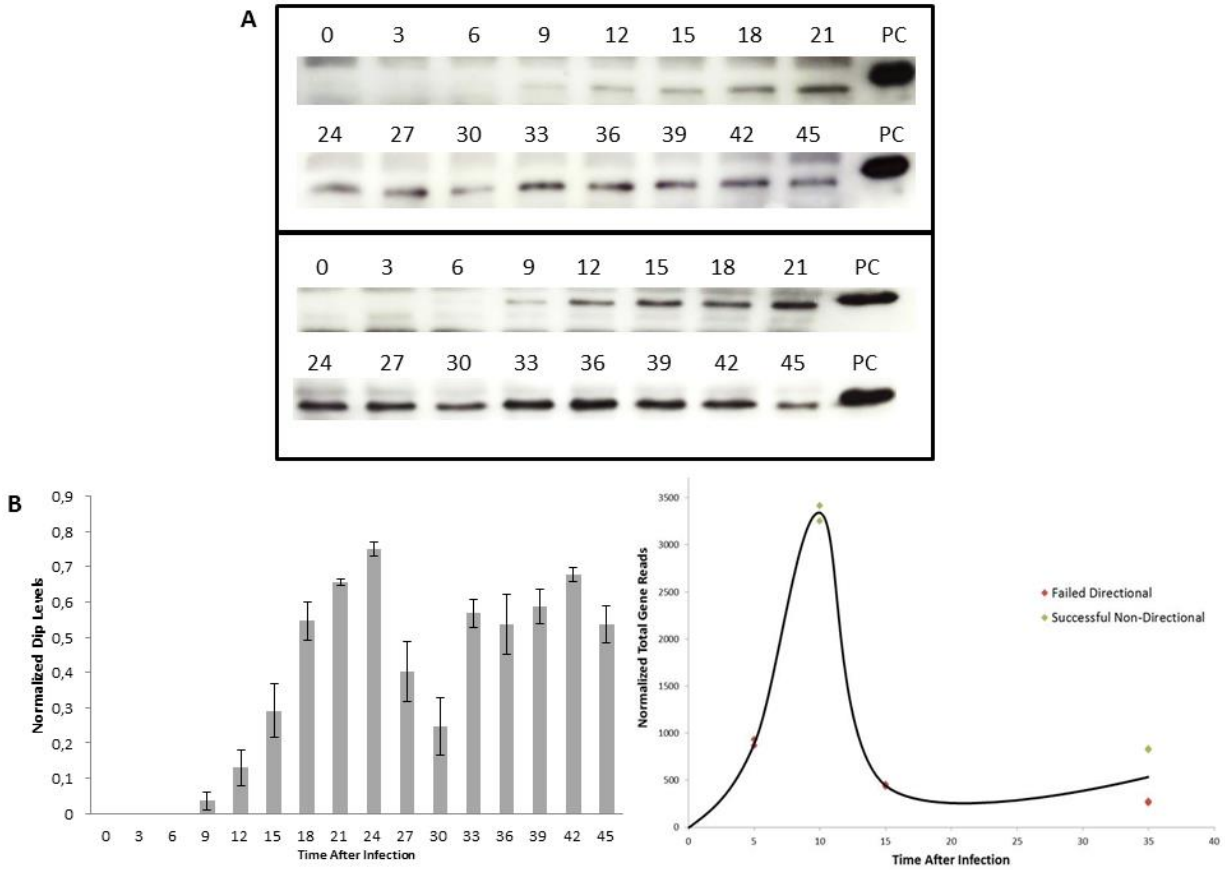

Figure 38: Follow-up on Dip levels during phiKZ infection. A: Western blots for two of three separate phiKZ infection cycles. Western blot was used to detect Dip every three minutes during the 45 minutes phiKZ infection cycle. B: Pixel number and intensity were quantified and normalized against the positive control in imageJ (left). Standard deviations are depicted for every time point and are based on three independent measurements. Non-directional RNA seq. data suggest a strong increase in transcription at minutes, whereas failed directional RNA seq. data indicate a decay in Dip transcript levels at 15 minutes (Blasdel, personal communication; Ceyssens *et al.*, 2014) (right).

The Western blot results correspond relatively well with the available RNA seq. data. A first trace of Dip is detected at nine minutes and peak levels are present at 24 minutes after the start of phiKZ infection. The RNA seq. data suggest a transcription peak at 10 minutes (non-directional), whereas poor directional data suggest there is a strong decay of Dip transcript levels at 15 minutes. However, a delay of 14 minutes seems to be present between the transcription and translation peaks of Dip. This delay could be due to differences in experimental set up between the Dip persistence and RNA seq. experiments. Alternatively, Dip translation could occur in several rounds, which would explain the gradual increase in Dip levels (see Figure 38 B). As such, Dip would protect its own transcripts by inhibition of the RNA degradosome. Moreover, the RNA seq. data that suggest a decay in Dip transcripts at 15 minutes after phage infection have a very low sequencing depth and are therefore not very reliable. In addition, Dip levels seem to drop after 24 minutes and rise again at 30 minutes, according to the western blot experiments. Therefore, a second round of transcription might occur at approximately 25 minutes after phage infection. This 'second batch' of Dip could serve to protect the transcripts from structural genes at late phage infection. Since no RNA seq. data is available for these

time points, this hypothesis should be confirmed by real time PCR. Either way, transcription and translation are complex processes and it's difficult to devise a solid theory solely based on these limited RNA seq. and additional Western blot experiments. To link the protein-level data presented here with transcript-level data and infer strong conclusions, real time PCR experiments should be used to effectively track the Dip transcripts during phage infection. However, from the current data it is clear that Dip is present in the cell approximately nine minutes post infection and persists throughout the phiKZ infection.

5 General conclusions and future perspectives

In this dissertation we set out to characterize the unique interaction between a phiKZ encoded protein, Dip, and the RNA degradosome of the multidrug resistant pathogen *P. aeruginosa*. Moreover, the role of Dip during the phage infection cycle was further clarified. It is well known that most effector proteins fulfil their biological role by means of direct interactions with their target, either within an intracellular network or in a predator-host relationship (Wodak *et al.,* 2013). For the latter, bacteriophages have developed an impressive and currently undervalued repertoire of effector proteins which interact with specific host proteins. Through these interactions, phages redirect the host metabolism, which allows them to take over their bacterial victims (Roucourt & Lavigne, 2009). Much is to be learned about these often clever interaction strategies. Once an interesting interaction is identified, a full structural and functional understanding of the interaction mechanism must be obtained in order to devise derivative applications, either in pharmaceutics or as a novel biotech tool. Therefore, the rather fundamental research presented here contributes indirectly to these new developments.

5.1 Glutamate and aspartate residues on the outer surface of Dip are crucial for binding the RNase E scaffold domain.

Previous research provided some evidence that phages can act on the RNA degradosome of their host (Ueno & Yonesaki, 2004; Marchand *et al.*, 2008). However, Dip is the first known viral effector protein to do so by a direct interaction with the RNA degradosome, i.e. with both RNA binding sites on the RNase E scaffold domain. Furthermore, co-crystallization experiments indicate that Dip binds these RNA binding sites by means of large acidic patches on its outer surface. A series of mutagenesis experiments and mobility shift assays have proven that two glutamate residues on the outer edge of Dip (E214 and E222) are crucial in maintaining the acidity of the surface patches and hence the binding capacity of Dip. In addition, two aspartate residues add to the acidity of these patches. Together, these residues constitute the two RNase E binding pockets on the Dip dimers, as further clarified by crystallography experiments. The next step would be to design virtual small molecule inhibitors that mimic this binding pocket in terms of structure and charge distribution. Unlike the RNase E catalytic domain, the RNase E scaffold domain has not been crystallized and is predicted to be unstructured. As a consequence, designing inhibitory small molecule inhibitors based on the RNA binding sites of the RNase E scaffold domain has been unfeasible to date. Therefore, Dip may prove to be an excellent blueprint to explore the efficacy of a new set of small molecules as inhibitors of the RNA degradosome. In addition, the production of small molecule inhibitors is straightforward and

their formulation is stable compared to the whole Dip protein. Some possible applications for these small molecule inhibitors are discussed in 5.4.

5.2 Dip, the first multi-domain member of a bacteriophage-encoded RNA mimicry protein family?

Several techniques can be used to determine the molar mass of proteins and protein complexes and to infer possible interaction models. For some proteins the interaction model is straightforward and is rather easy to reveal. However, different techniques seem to suggest different interaction models for Dip and RNase E. Figure 39 presents an overview of the probable and less probable interaction models.

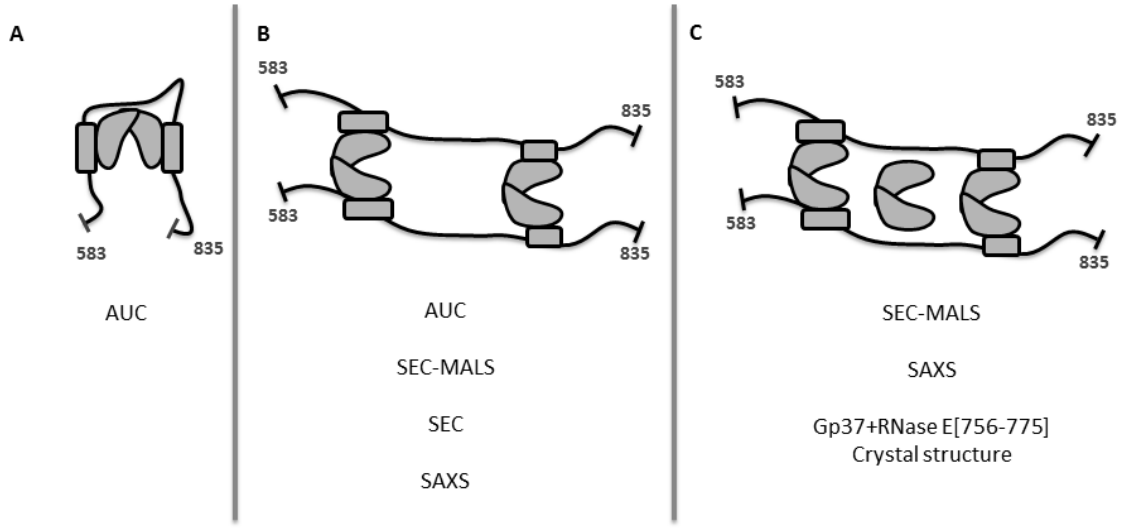

Figure 39: Overview of all possible interaction models between Dip and RNase E, as suggested by the experiments carried out in this dissertation. RNase E [583-835] is presented as thick lines and Dip is presented as clamp-like dimers.

Although initial AUC experiments clearly suggest a 1:1 interaction model of Dip and RNase E, other experiments have provided differing results. The AUC experiments however, were carried out at room temperature and repeating these UAC experiments at 4°C might stabilize the complex, which could result in a single, higher molecular weight peak. A more appropriate approach might be to repeat the SEC-MALS experiments with freshly purified complex, since SEC-MALS is a more accurate technique than AUC. Furthermore, in depth optimization of the buffer should lead to a more stable complex between Dip and RNase E fragments. Once an optimal buffer is found, crystallography screens should be carried out again, using the conditions that produced crystals previously. Finally, cross-linking the complexes should prevent dissociation and might result in well diffracting crystals.

SAXS experiments, in combination with independent bioinformatics approaches indicate that the crystal structure of Dip is an imperfect representation of its solution structure. Moreover, structural

refinement against the SAXS data and *ab initio* modelling efforts indicate that a twisted and compact Dip dimer strongly resembles the solution structure. However, additional SAXS data should be collected for a dilution series of Dip. As such, the maximum resolution without any aggregation or multimerization can be achieved for *ab initio* model building. In addition, crystallography, SEC-MALS and SAXS experiments suggest that Dip assembles into a helical higher order structure when bound to RNase E (see Figure 39 C). Even though this is a daring hypothesis and the supporting experimental data is rather scarce and of low resolution, the idea is not completely unimaginable. Bacteriophage-encoded members of the DNA mimicry have been identified, with Ocr of bacteriophage T7 being the representative. In Ocr, the glutamate and aspartate carboxyl groups mimic the charge distribution of the phosphate groups on a B-DNA backbone. As such, Ocr mimics B-DNA to misguide its target, type I restriction enzymes of the host (Atanasiu.*et al.*, 2001; Walkinshaw *et al.*, 2002). Similarly, Dip might mimic RNA duplex strands to misguide the RNA degradosome of *P. aeruginosa* and efficiently block the binding of structured RNAs. Even though glutamate and aspartate residues make up the binding pocket on the Dip surface, a high resolution map of the multimeric state of Dip in solution should be obtained to verify the helical assembly.

Should the hypothetical Dip helix be confirmed, the charge distribution on the helical surface as well as the size parameters must be compared to those of duplex RNA before crowning Dip as the first bacteriophage-encoded mimic of RNA. Preliminary EM screens of Dip bound to the E. coli ternary complex point towards ideal particle behavior for cryo-EM studies, which should resolve the interaction model mystery that has been put forward in this dissertation. Finally, the question as to whether Dip undergoes 'limited' or 'unlimited' multimerization in the cell could be resolved with straightforward fluorescence experiments. Therefore, Dip has already been fused to GFP to track Dip *in vivo* with fluorescence microscopy and assess its oligomerization state, as well as its intracellular localization.

5.3 PhiKZ sustains transcript protection throughout the entire infection cycle

Western blot experiments indicate that Dip persists during the phiKZ infection cycle. Furthermore, Dip is detected only after 9 minutes, which correlates to previously available RNA seq. data (Ceyssens *et al.*, 2014). These observations strengthen the hypothesis that Dip is produced to protect the newly transcribed RNA by direct inhibition of the RNA degradosome. Furthermore, *in vitro* tests have shown that the inhibitory effect is independent of the origin of the mRNA. Since Dip is being expressed after 10 minutes, phiKZ could regulate its transcript protection in a time dependent way, after most of the host mRNA has already been degraded. Indeed, RNA seq. experiments point towards a strong increase in overall transcript levels at 15 and 35 minutes post phiKZ infection

(ceyssens *et al.*, 2014). Additional quantitative RT-PCR experiments could be used for accurate *in vivo* measurements on the mRNA levels of both phiKZ and the host at several time points post phiKZ infection. Moreover, RT-PCR of the Dip transcript can partly confirm the observed expression profile and assess the transcript persistence *in vivo*. However, to fully map the expression profile of Dip, the variability of the phiKZ infection cycle should be investigated first. PhiKZ is a giant phage and some variability in replication time and particle assembly should be expected. Even though the infection cycle was determined to be 45 minutes, time lapse microscopy experiments have shown that cells can still be alive 60 minutes post phiKZ infection (De Smet, 2012; Ceyssens *et al.*, 2014). Additional large-scale time lapse microscopy experiments can be used to further clarify the infection cycle variability of phiKZ.

Next, the role of Dip in phiKZ infection should be assessed. Two separate experiments were initiated towards a further functional elucidation of Dip. First, overexpression of an RNase E fragment containing the Dip binding sites during phiKZ infection might sequester Dip from the RNA degradosome. Second, antisense RNA experiments can be used to knock down Dip during infection. As such, the efficiency of phiKZ infection without Dip can be assessed. Finally, CRISPR-Cas genome editing should enable a knockout of Dip, despite the size of the phiKZ genome, which could independently confirm the role of Dip during the infection.

5.4 Towards therapeutic applications and biotechnological tools

During the past decades, the characterization of phage-host PPIs has brought new insights into at least two fields. First, understanding phage-PPIs has fed the need for new and inventive strategies to combat multidrug resistant bacteria, like *P. aeruginosa*. Second, host-phage interactions have led to numerous ground breaking biotechnological tools, such as restriction-ligation cloning and CRISPR-Cas editing.

5.4.1 Dip as an antibacterial agent

As described in 1.1.4 '*Pseudomonas aeruginosa*: a superbug driving the development of inventive new therapies', the innovation gap in drug discovery and the overuse of antibiotics has led to an ever increasing number of multidrug resistant bacteria since 2000 (Basetti *et al.*, 2013). Since Dip inhibits the RNA degradosome in a direct and efficient way, it is tempting to think of the degradosome as a new antibacterial target. Even though Dip decreases the growth rate of *P. aeruginosa and E. coli*, it does not kill these bacteria unless it's being overexpressed in the cell (Van den Bossche *et al.*, in submission). Therefore, it remains to be determined whether the RNA degradosome is a good antibacterial target. Nevertheless, small molecule inhibitors have been designed and tested for the

catalytic domain of the *E. coli* and *Mycobacterium tuberculosis* RNase E (Kime *et al.*, 2015). Therefore it is worth trying to develop Dip-based small molecule inhibitors against the scaffold domain of RNase E, and test these against a series of pathogens, including *P. aeruginosa* and *E. coli*, whether or not in conjunction with the small molecule inhibitors against the catalytic domain. However, it remains to be determined whether Dip can be an effective, stand-alone drug.

Since Dip is able to interact with the *E. coli* and *C. crescentus* RNA degradosome as well, and inhibit RNA degradation, the strength of Dip lays in its broad interaction range rather than in its toxicity (Van den Bossche *et al.*, in submission). Therefore, it might be interesting to test whether Dip improves the infection of a series of phages in *P. aeruginosa*, *E. coli* and *C. crescentus*. Therefore, the efficiency of phage infection for a range of *P. aeruginosa* phages should be tested with and without heterologous expression of Dip at several time points during infection. As such, the efficiency can be quantified in terms of the infection cycle duration and burst size. In addition, even though therapeutic applications for whole phages still face a lot of regulatory problems, phage therapy is, amongst others, currently being used to treat *P. aeruginosa* infections in severe burn wounds (Rose *et al.*, 2014; Brüssow, 2015). Moreover, whole phages and modified phages are gaining popularity in the food industry, where they are used to control microbial contaminations in food and food processing environments (Endersen *et al.*, 2014). If Dip would prove to be beneficial to other phages in terms of infection efficiency, then recombinant phages could be designed to improve phage therapy and phage-mediated microbial control in food processing and other applications.

5.4.2 Dip could open the door to new biotechnological applications

Since Dip might interact with RNase E from a broad range of bacterial species and can inhibit RNA degradation without killing the bacterial cell, several possible biotechnological applications can be envisaged. Either heterologous Dip expression in the bacterial cell of interest or small molecule inhibitors based on Dip can be utilized. One could imagine, for example, that heterologous expression of a protein of interest in an *E. coli* expression strain could yield higher protein levels when the corresponding mRNA is subject to little degradation. However, the Dip or small molecule dose needed to obtain a maximal yield with a minimal growth retardation should be established, since RNase E plays an important role in RNA processing as well (Mackie, 2013). Moreover, researchers are often interested in the direct cause of the degradation of mRNA, tRNA and rRNA in a given experimental set up, e.g. when testing stress responses of bacteria. A specific example is that of the degradation of stable RNAs, rRNA and tRNA, upon starvation. Although RNase E is involved in the maturation of rRNA and tRNA, it is not known whether the degradosome is also involved in the degradation of these stable RNAs (Mäivali *et al.*, 2013; Deutscher, 2003). Heterologous expressed Dip

or Dip-based small molecule inhibitors could be employed to switch off the RNA degradosome, rather than designing RNase E knock out mutants, and thus facilitate such experiments.

In addition, Dip or Dip-based small molecule inhibitors can be related to CRISPR-Cas editing or RNA interference applications. Both the RNA interference and CRISPR-Cas mechanisms use short RNA fragments in association with a ribonuclease (complex) to target RNA or DNA substrates in the cell. Although no information has been found in the current literature, it is conceivable that RNase E influences the efficiency of these knock down (RNAi) and genome editing/knock out (CRISPR-Cas) techniques. In the case of CRISPR-Cas for example, one may want to use a CRISPR array to knock out several genes at once. The corresponding pre-crRNA will be long and could be subject to degradation by the bacterial RNase E. Therefore Dip or Dip-based small molecule inhibitors might improve the CRISPR-Cas performance *in vivo*. In antisense RNA experiments, on the other hand, the specificity of the antisense transcript increases with its length. However, long antisense RNAs are unstable and might be subject to degradation by ribonucleases. It is worth testing whether Dip or Dip-based small molecule inhibitors can improve the stability of long antisense RNAs thus the performance of antisense based knock down of gene expression.

This dissertation proves that bacteriophage-host PPIs hold many unresolved and inspiring mechanisms. Considering the possible aims for Dip, the research presented here again illustrates the importance of gaining fundamental insights as a driver for potential therapeutic or biotechnological applications.

References

Ackermann HW & Krisch HM (1997) A catalogue of T4-type bacteriophages. *Arch. Virol.* **142:** 2329-45

Atanasiu C, Bryon O, McMiken H, Sturrock SS & Dryden DTF (2001) Characterisation of the structure of ocr, the gene 0.3 protein of bacteriophage T7. *Nucleic acids Res.* **29:** 3059-68

Balasubramanian D, Schneper L, Kumari H & Mathee K (2013) A dynamic and intricate regulatory network determines *Pseudomonas aeruginosa* virulence. *Nucleic Acids Res.* **41:** 1-20

Bandyra KJ, Bouvier M, Carpousis AJ & Luisi BF (2013) The social fabric of the RNA degradosome. *Biochim. Biophys. Acta* **1829:** 514-22

Baños-Sanz JI, MojardÍn L, Sanz-Aparicio J, Lázaro JM, Villar L, Serrano-Heras G, González B & Salas M (2013) Crystal structure and functional insights into uracil-DNA glycosylase inhibition by phage phi29 DNA mimic protein p56. *Nucleic Acids Res.***41:** 6761-6773

Bassetti M, Merelli M, Temperoni C & Astilaen A(2013) New antibiotics for bad bugs: where are we? *Ann. Clin. Microbiol. Antimicrob.* **12:** 22

Battye TGG, Kontogiannis L, Johnson O, Powell HR and Leslie AGW (2011).IMosflm: a new graphical interface for diffraction-image processing with MOSFLM. *Acta Cryst.***67:** 271-81

Ben Haj Khalifa A, Moissenet D, Thien HV, Khedher M (2011) Les facteurs de virulence de *Pseudomonas aeruginosa*: Mécanismes et modes de régulations. *Ann Biol. Clin.* **69:** 393-403

Bernstein JA, Lin PH, Cohen SN & Lin-Chao S (2004) Global analysis of *Escherichia coli* RNA degradosome function using DNA microarrays. *Proc. Natl. Acad. Sci. U. S. A.***101:** 11109-11114

Breidenstein EBM, de la Fuente-Nùñez C & Hancock REW (2011) *Pseudomonas aeruginosa*: all roads lead to resistance. *Trends Microbiol.* **19:** 419-26

Brooun A, Liu S & Lewis K (2000) A dose-response study of antibiotic resistance in *Pseudomonas aeruginosa* biofilms. *Antimicrob. Agents Chemother.* **44:** 640-6

Brüssow H (2012) What is needed for phage therapy to become a reality in Western medicine? *Virology* **2:** 138-42

Callaghan AJ, Marcaida MJ, Stead JA, McDowall KJ, Scott WG & Luisi BF (2005) Structure of *Escherichia coli* RNase E catalytic domain and implications for RNA turnover. *Nature* **437:** 1187-91

Callaghan AJ, Aurikko JP, Ilag LL, Günter Grossman J, Chandran V, Kühnel K, Poljak L, Carpousis AJ, Robinson CV, Symmons MF & Luisi BF (2004) Studies of the RNA degradosome organizing domain of the *Escherichia coli* ribonuclease RNase E. *J. Mol. Biol.* **340:** 965-79

Carpousis AJ (2002) The *Escherichia coli* RNA degradosome: structure, function and relationship in other ribonucleolytic multienzyme complexes. *Biochem. Soc. Trans.* **30:** 150-155

Carpousis AJ (2007) The RNA degradosome of Escherichia coli: an mRNA degrading machine assembled on RNase E. *Annu. Rev. Microbiol.* **61:** 71-87

Ceyssens P-J, Glonti T, Kropinski NM, Lavigne R, Chanishvili N, Kulakov L, Lashkhi N, Tediashvili M & Merabishvili M (2011) Phenotypic and genotypic variations within a single bacteriophage species. *Virol. J.* **8:** 134

Ceyssens P-J, Hertveldt K, Ackermann H-W, Noben J-P, Demeke M, Volckaert G & Lavigne R (2008a) The intron containing genome of the lytic Pseudomonas phage LUZ24 resembles the temperate phage PaP3. *Virology* **377:** 233-8

Ceyssens P-J, Mesyanzhinov V, Sykilinda N, Briers Y, Roucourt B, Lavigne R, Robben J, Domashin A, Miroshnikov K, Volckaert G & Hertveldt K (2008b) The genome and structural proteome of YuA, a new *Pseudomonas aeruginosa* phage, resembling M6. *J. Bacteriol.* **190:** 1429-35

Ceyssens P-J, Minakhin L, Van den Bossche A, Yakunina M, Klimuk E, Blasdel B, De Smet J, Noben J-P, Severinov K & Lavigne R (2014) Development of giant bacteriophage phiKZ is independent of the host transcription apparatus. *J. Virol.* **88:** 10501-10

Chandran V, Poljak L, Vanzo NF, Leroy A, Miguel RN, Fernandez-Recio J, Parkinson J, Burns C, Carpousis AJ & Luisi BF (2007) Recognition and cooperation between the ATP-dependant RNA helicase RhIB and ribonuclease RNase E. *J. Mol. Biol.* **367:** 113-32

Chen YT, Chang HY, Lu CL & Peng H-L (2004) Evolutionary analysis of the two component systems in *Pseudomonas aeruginosa* PAO1. *J. Mol. Evol.* **59:** 725-37

Choi KH, Kumar A & Schweizer HP (2006) A 10-min method for preparation of highly electrocompetent Pseudomonas aeruginosa cells: application for DNA fragment transfer between chromosomes and plasmid transformation. *J. Microb. Meth.* **64:** 391-7

Clokie MRJ, Millard AD, Letarov A V & heaphy S (2011) Phages in nature. *Bacteriophage* **1:** 31-45

Coleman FT, Mueschenborn S, Meluleni G, Ray C, Carey VJ, Vargas SO, Cannon CL, Ausubel FM & Pier GB (2003) Hypersusceptibility of cystic fibrosis mice to chronic *Pseudomonas aeruginosa* oropharyngeal colonization and lung infection. *Proc. Natl Acad. Sci. U. S. A.* **100:** 1949-1954

Cordin O, Banroques J, Tanner NK & Linder P (2006) The DEAD-box protein family of RNA helicases. *Gene* **367:** 17-37

Cornelissen A, Hardies SC, Shaburova O V, Krylov VN, Mattheus W, Kropinski AM & Lavigne R (2012) Complete genome squenc of the giant virus OBP and comparative genome analysis of the diverse phiKZ-related phages. *J. Virol.* **86:** 1844-52

Court R, Cook N, Saikrishnan K & Wigley D (2007) The crystal structure of λ-Gam protein suggests a model for RecBCD inhibition. *J. Mol. Biol.***371:** 25-33

Courvalin P (2008) predictable and unpredictable evolution of antibiotic resistance. *J. Intern.Med.* **264:** 4-16

De Lay N, Schu DJ & Gottesman S (2013) Bacterial small RNA-based negative regulation: Hfq and its accomplices. *J. Biol. Chem.* **288:** 7996-8003

Deana A, Celesnik H & Belasco JG (2008) The bacterial enzyme RppH triggers messenger RNA degradation by 5' pyrophosphate removal. *Nature* **451:** 355-8

De Smet J (2011) Search for the unknown: Proteome analysis of bacteriophage-infected Pseudomonas aeruginosa cells. Master thesis

Deutscher PM (2003) Degradation of stable RNA in Bacteria. *Journ. Biol. Chem.* **278:** 45041-44

Diggle SP, Matthijs S, Wright VJ, Fletcher MP, Chhabra SR, Lamont IL, Kong X, Hider RC, Cornelis P, Camara M *et al.* (2007) The *Pseudomonas aeruginosa* 4-quinolone signal molecules HHQ and PQS play multifunctional roles in quorum sensing and iron entrapment. *Chem. Biol.* **14:** 87-96

Drenkard E (2003) Antimicrobial resistance of *Pseudomonas aeruginosa* biofilms. *Microbes Infect.***5:** 1213-19

Dressaire C, Picard F, Redon E, Loubière P, Queinnec I, Girbal L & Cocaign-Bousquet M (2013) Role of mRNA stability during bacterial adaptation. *PLoS One* **8:** e59059

Driscoll JA, Brody SL & Kollef MH (2007) The epidemiology, pathogenesis and treatment of *Pseudomonas aeruginosa* infections. *Drugs* **67:** 351-68

Eidem TM, Roux CM & Dunman PM (2012) RNA decay: a novel therapeutic target in bacteria. *Wiley Interdicip. Rev. RNA.* **3:** 443-454

Emsley P & Lohkamp B (2010) Features and development of coot. *Acta Crystallogr. Sect. D, Biol. Crystallogr.* **66:** 486-501

Endersen L, O'Mahony J, Hill C, Ross RP, McAuliffe O, Coffey A (2014) Phage therapy in the food industry. *Annu. Rev. Food Sci. Technol.* **5**: 327-49

Engel LS, Hill JM, Moreau JM, Green LC, Hobden JA & O'Callaghan RJ (1998) *Pseudomonas aeruginosa* protease IV produces corneal damage and contributes to bacterial virulence. *Invest. Ophthalmol. Vis. Sci*. **39:** 662-5

Evans PR & Mushudov GN (2013) How good are my data and what is the resolution? *Acta Cryst.* **69:** 1204-14

Feigin LA & Svergun DI (1987) Structure analysis by small-angle X-ray and neutron scattering. *D.I. Plenum Press*, New York. 335p.

Flemming HC & Wingender J (2010) The biofilm matrix. *Nat. Rev. Microbiol.* **8:** 623-33

Fokine A, Battisti AJ, Bowman VD, Efimov AV, Kurochkina LP, Chipman PR, Mesyanzhinov VV, Rossmann MG (2007) Cryo-EM study of the pseudomonas Bacteriophage phiKZ. *Structure* **15:** 1099-1104

Franke D & Svergun DI (2009) DAMMIF, a program for rapid ab-initio shape determination in small-angle scattering. *J. Appl. Cryst*. **42:** 342-6

Gallet R, Lenormand T & Wang I-N (2012) Phenotypic stochasticity protects lytic bacteriophage populations from extinction during the bacterial stationary phase. *Evolution* **66:** 3485-94.

Galperin MY (2006) Structural classification of bacterial response regulators: diversity of output domains and domain combinations*. J Bacteriol* **188:** 4169–4182.

Gao J, Lee K, Zhao M, Qiu J, Zhan X, Saxena A, Moore CJ, Cohen SN & Georgiou G (2006) Differential modulation of *E. coli* mRNA abundance by inhibitory proteins that alter the composition of the degradosome. *Mol. Microbiol.* **61:** 394-406

Garrey SM, Blech M, Riffell JL, Hankins JS, Stickney LM, Diver M, Hsu Y-HR, Kunanithy V & Mackie GA (2009) Substrate binding and active site residues in RNases E and G: role of the 5' sensor. *J. Biol. Chem.* **284:** 31834-50

Gellatly SL, Hancock REW (2013) *Pseudomonas aeruginosa*: new insights into pathogenesis and host defenses. *FEMS Pathogens and Disease* **67**: 159-173

Gooderham WJ & Hancock REW (2009) Regulation of virulence and antibiotic resistance by two-component regulatory systems in *Pseudomonas aeruginosa*. *FEMS Microbial. Rev.* **33:** 279-94

Górna MW, Carpousis AJ & Luisi BF (2012) From conformational chaos to robust regulation: the structure and function of the multi-enzyme RNA degradosome. *Q. Rev. Biophys.* **45:** 105-45

Górna MW, Pietras Z, Tsai Y-C, Callaghan AJ, Hernández H, Robinson C V & Luisi BF (2010) The regulatory protein RraA modulates RNA-binding and helicase activities of the *E. coli* RNA degradosome. *RNA* **16:** 553-62

Grant BJ, Rodrigues APC, ELSawy KM, McCammon JA & Caves LSD (2006) Bio3d: an R package for the comparative analysis of protein structures. *Bioinformatics* **22:** 2695-96

Hanahan D (1983) Studies on transformation of *Escherichia coli* with plasmids. *J. Mol. Biol.* **166:** 557-80

Hardwick S & Luisi B (2012) Rarely at rest: RNA helicases and their busy contributions to RNA degradation, regulation and quality control. *RNA Biol.* **10:** 56-70

Hauser AR (2010) The type III secretion system of *Pseudomonas aeruginosa*: Infection by injection. *Nat. Rev.***7:** 654-665

Hendrix RW (2002) Bacteriophages: Evolution of the Majority. *Theor. Popul. Biol.* **61:** 471-480

Hertveldt K, Lavigne R, Pleteneva E, Sernova N, Kurochkina L, Korchevskii R, Robben J, Mesyanzhinov V, Krylov VN & Volckaert G (2005) Genome comparison of *Pseudomonas aeruginosa* large phages. *J. Mol. Biol.* **354:** 536-545

Hood RD, Singh P, Hsu F, Güvener T, Carl MA, Trinidad RRS, Silverman JM, Ohlson BB, Hicks KG, Plemel RL, Li M, Schwarz S, Wang WY, Merz AJ, Goodlett DR & Mougous JD (2010) A type VI secretion system of *Pseudomonas aeruginosa* targets a toxin to bacteria. *Cell Host Microbe* **7:** 25-37

Horn MP, Zuercher AW, Imboden MA, Rudolf MP, Lazar H, Wu H, Hoiby N, Fas SC & Lang AB (2010) Preclinical in vitro and in vivo characterization of the fully human monoclonal IgM antibody KBPA101 specific for *Pseudomonas aeruginosa* serotype IATS-O11. *Antimicrob. Agents Chemother.* **54:** 2338-44

Huang B (2009) MetaPocket: a meta approach to improve protein ligand binding site prediction. *OMICS* **13:** 325-30

Ikeda Y, Yagi M, Morita T & Aiba H (2011) Hfq binding at RhIB-recognition region of RNase E is crucial for the rapid degradation of target mRNAs mediated by sRNAs in *Escherichia coli. Mol. Microbial.* **79:** 419-32

Iost I, Guillerez J & Dreyfus M (1992) Bacteriophage T7 RNA polymerase travels far ahead of ribosomes in vivo. *J. Bacteriol.* **174:** 619-622

Jacques DA & Trewhella J (2010) Small-angle scattering for structural biology- Expanding the frontier while avoiding the pitfalls. *Protein science: A Publication of the Protein Society.* **19:** 642-57

Jakobsen TH, van Gennip M, Phipps RK, Shanmugham MS, Christensen LD, Alhede M, Skindersoe ME, Rasmussen TB, Friedrich K, Uthe F, Jensen PØ, Moser C, Nielsen KF, Eberl L, Larsen TO, Tanner D, Høiby N, Bjarnsholt T & Givskov M (2012) Ajoene, a sulfur-rich molecule from garlic, inhibits genes controlled by quorum sensing. *Antimicrob. Agents Chemother.* **56:** 2314-25

Kaberdin V & Bläsi U (2013) Bacterial helicases in post-transcriptional control. *Biochim. Biophys. Acta* **1829:** 878-83

Kaberdin VR (2003) Probing the substrate specificity of *Escherichia coli* RNase E using a novel oligonucleotide based assay. *Nucleic acids Res.* **31:** 4710-4716

Kenna DT, Doherty CJ, Foweraker J, Macaskill L, Barcus VA, Govan JRW (2007) Hypermutability in environmental Pseudomonas aeruginosa and in populations causing pulmonary infection in individuals with cystic fibrosis. *Microbiol.* **153:** 1852-59

Khemici V & Carpousis AJ (2003) The RNA degradosome and poly(A) polymerase of *Escherichia coli* are required in vivo for the degradation of small mRNA decay intermediates containing REP-stabilizers. *Mol. Microbiol*. **51:** 777-90

Khemici V, Poljak L, Luisi BF & Carpousis AJ (2008) The RNase E of *Escherichia coli* is a membrane-binding protein. *Mol Microbiol.* **70:** 799-813

Kime L, Vincent HA, Gendoo DMA, Jourdan SS,Fishwick CWG, Callaghan AJ & McDowall KJ (2015) The first small-molecule inhibitors of members of the ribonuclease E family. *Scient. Rep.* **5:** 8028

Konarev PV, Petoukhov MV, Volkov VV & Svergun DI (2006) ATSAS 2.1, a program package for small-angle scattering analysis. *J. Appl. Cryst.* **39:** 277-86

Konarev PV, Volkov VV, Sokolova AV, Koch MHJ & Svergun DI (2003). PRIMUS - a Windows-PC based system for small-angle scattering data analysis. *J Appl Cryst.* **36:** 1277-82

Koskella B & Brockhurst MA (2014) Bacteria-phage coevolution as a driver of ecological and evolutionary processes in microbial communities. *FEMS Microbiol. Rev.* **38:** 916-31

Kovalyova I V & Kropinski AM (2003) The complete genomic sequence of lytic bacteriophage gh-1 infecting *Pseudomonas putida*-evidence for close relationship to the T7 group. *Virology* **311:** 305-315

Kropinski AM (2000) Sequence of the genome of the temperate serotype-converting *Pseudomonas aeruginosa* bacteriophage D3. *J. Bacteriol.* **182:** 6066-74

Krylov V, Smirnova T, Minenkova I, Plotnikova T, Zhazikov I & Khrenova E (1984) *Pseudomonas* bacteriophage contains an inner body in its capsid. *Can. J. Microbiol.* **30:** 758-62

Krylov VN, Dela Cruz DM, Hertveldt K & Ackermann H-W (2007) "phiKZ-like viruses", a proposed new genus of myovirus bacteriophages. *Arch. Virol.* **152:** 1955-9

Kühnel & Luisi BF (2001) Crystal structure of the *Escherichia coli* RNA degradosome component enolase. *J. Mol. Biol.**313:** 583-92*

Laarman AJ, Bardoel BW, Ruyken M, Fernie J, Milder FJ, van Strijp J a G & Rooijakkers SHM (2012) *Pseudomonas aeruginosa* alkaline protease blocks complement activation via the classical and lectin pathways. *J. Immunol.* **188:** 386-93

Laue B, Shah B, Ridgeway T & Pelletier S (1992) Computer aided interpretation of analytical sedimentation data for proteins. In Ultracentrifugation in Biochemistry and Polymer Science, Harding, R.S.E., and J.C. Horton, eds. pp. 90-125

Leroy A, Vanzo NF, Souza S, Dreyfus M & Carpousis AJ (2002) Function in Escherichia coli of the non-catalytic part of RNase E: Role in the degradation of ribosome free mRNA. *Mol Microbiol.* **45:** 1231-43

Li Y, Petrova OE, Su S, Lau GW, Panmanee W, Na R, Hassett DJ, Davies DG & Karin Sauer (2014) BdlA, DipA and induced dispersion contribute to acute virulence and chronic persistence of *Pseudomonas aeruginosa. PLOS Pathogens* **10 (6):** e1004168

Lindahl T, Ljungquist S, Siegert W, Nyberg B & Sperens B (1997) DNA N-glycosidases: properties of uracil-DNA glycosidase from *Escherichia coli. J. Biol. Chem.,* **252:** 3286-94

Linder P & Jankowsky E (2011) From unwinding to clamping – the DEAD bos RNA helicase family. *Nat. Rev. Mol. Cell. Biol.* **12:** 505-16

Macfarlane EL, Kwasnicka A & Hancock RE (2000) Role of *Pseudomonas aeruginosa* PhoP-PhoQ in resistance to antimicrobial cationic peptides and aminoglycosides. *Microbiology* **146:** 2543-2554

Mackie GA (2013) RNase E: at the interface of bacterial RNA processing and decay. *Nat. Rev. Microbiol.* **11:** 45-57

Mäivali Ü, Paier A & Tenson T (2013) When stable RNA becomes unstable: the degradation of ribosomes in bacteria and beyond. *Biol. Chem.* **394:** 845-55

Majorek KA, Dunin-Horkawicz S, Steczkiewicz K, Muszewska A, Nowotny M, Ginalski K & Bujnicki JM (2014) The RNase H-like superfamiliy: new members, comparative structural analysis and evolutionary classification. *Nucleic Acids Res.* **42:** 4160-79

Malaby AW, Chakravarthy S, Irving TC, Kathuria SV, Bilsel O & Lambright DG (2015) Methods for analysis of size-exclusion chromatography-small-angle X-ray scattering and reconstruction of protein scattering. *J. Appl. Cryst.***48:** 1102-13

Maniloff J & Ackermann H-W (1998) Taxonomy of bacterial viruses: establishment of tailed virus genera and the order *Caudovirales. Archives of virology* **143:** 2051-2063

Marchand I, Nicholson AW & Dreyfus M (2008) Bacteriophage T7 protein kinase phosphorylates RNase E and stabilizes mRNAs synthesized by T7 RNA polymerase. *Mol. Microb.* **42:** 767-76

Marcaida MJ, DePristo MA, Chandran V, Carpousis AJ & Luisi BF (2006) The RNA degradosome: life in the fast lane of adaptive molecular evolution. *Trends Biochem. Sci.* **31:** 359-65

Mathee K, Narasimhan G, Valdes C, Qiu X, Matewish JM, Koehrsen M, Rokas A, Yandava CN, Engels R, Zeng E, Olavarietta R, Doud M, Smith RS, Montgomery P, White JR, Godfrey PA, Kodira C, Birren B, Galagan JE & Lory S (2008) Dynamics of Pseudomonas aeruginosa genome evolution. *Proc. Natl. Acad. Sci. U. S. A.* ***105*****:** 3100-5

Maxwell KL (2016) Phages fight back: inactivation of the CRISPR-Cas bacterial immune system by Anti-CRISPR proteins. *PLOS Pathog.***12:** e1005282

McCoy AJ, Grosse-Kunstleve RW, Adams PD, Winn MD, Storoni LC & Read RJ (2007) *Phaser* crystallographic software. *J. Appl. Cryst.* **40:** 658-74

McPhee JB, Bains M, Winsor G, Lewenza S, Kwasnicka A., Brazas MD, Brinkman FS & Hancock RE (2006) Contribution of the PhoP-PhoQ and PmrA-PmrB two component regulatory systems to Mg^{2+} -induced gene regulation in *Pseudomonas aeruginosa*. *J. Bacteriol* **188:** 3995-4006

Mesyanzhinov VV, Robben J, Grymonprez B, Kostyuchenko VA, Bourkaltseva MV, Sykilinda NN, Krylov VN & Volckaert G (2002) The genome of Bacteriophage phiKZ of *Pseudomonas aeruginosa*. J. Mol. Biol.**317:** 1-19

Miao EA, Andersen-Nissen E, Warren SE & aderem A (2007) TLR5 and Ipaf: dual sensors of bacterial flagellin in the innate immune system. *Semin. Immunopathol.* **29:** 275-288

Morita T, Kawamoto H, Mizota T, Inada T & Aiba H (2004) Enolase in the RNA degradosome plays a crucial role in the rapid decay of glucose transporter mRNA in the response to phosphosugar stress in *Escherichia coli*. *Mol. Microbiol.* **54:** 1063-75

Murshudov G, Vagin A & Dodson E (1997) Refinement of macromolecular structures by the maximum likelihood method. *Acta Crystallogr. Sect. D, Biol. Crystallogr.* **53:** 240-255

Oliver A, Baquero F & Blázquez J (2002) The mismatch repair system (mutS, mutL, and uvrD genes) in *Pseudomonas aeruginosa*: molecular characterization of naturally occurring mutants. *Mol. Microbiol.* **43:** 1641-50

Olsen I (2015) Biofilm-specific antibiotic tolerance and resistance. *Eur. J. Clin. Microbiol. Infect. Dis.* **34:** 877-86

Ow MC, Kushner SR (2002) Initiation of tRNA maturation by RNase E is essential for cell viability in *E. coli*. *Genes Dev.***16:** 1102-15

Panjkovich A & Svergun DI (2016) Deciphering conformational transitions of proteins by small angle X-ray scattering and normal mode analysis. *Phys. Chem. Chem. Phys.* **18:** 5707-19

Petoukhov MV, Franke D, Shkumatov AV, Tria G, Kikhney AG, Gajda M, Gorba C, Mertens HDT, Konarev PV & Svergun DI (2012) New developments in the ATSAS program package for small-angle scattering data analysis. *J. Appl. Cryst.* **45:** 342-50

Petoukhov MV & Svergun DI (2005) Global rigid body modelling of macromolecular complexes against small-angle scattering data. *Biophys. J.* **89:** 1237-50

Poirel L, Naas T & Nordmann P (2010) Diversity, epidemiology, and genetics of class D beta-lactamases. *Antimicrob.Agents chemother.* **54:** 24-38

Poole K (2005) Aminoglycoside resistance in *Pseudomonas aeruginosa*. *Antimicrob. Agents Chemother.* **49:** 479-487

Poole (2011) *Pseudomonas aeruginosa*: resistance to the max. *Front. Microbiol.* **2:** 65

Purusharth RI, Klein F, Sulthana S, Jäger S, Jagannadham MV, Evguenieva-Hackenberg E, Ray MK & Klug G (2005) Exoribonuclease R interacts with endoribonuclease E and an RNA helicase in the psychrotropic bacterium *Pseudomonas syringae* Lz4W. *J. Biol. Chem.* **280:** 14572-8

Putnam CD, Hammel M, Hura GL & Tainer JA (2007) X-ray solution scattering (SAXS) combined with crystallography and computation: defining accurate macromolecular structures, conformations and assemblies in solution. *Q. Rev. Biophys.* **40:** 191-285

Putnam CD, Shroyer JN, Lundquist AJ, Mol CD, Arvai AS, Mosbaugh DW & Tainer JA (1999) Protein mimicry of DNA from crystal structures of the uracil-DNA glycosylase inhibitor protein and its complex with E*scherichia coli* uracil-DNA glycosylase. *J. Mol. Biol.* **287:** 331-46

Putnam CD & Tainer JA (2005) Protein mimicry of DNA and pathway regulation. *DNA repair* **4:** 1410-20

Rasamiravaka T, Labtani Q, Duez P & El Jaziri M (2015) The formation of biofilms by *Pseudomonas aeruginosa*: a review of the natural and synthetic compounds interfering with control mechanisms. *Biomed. Res. Int.* **2015**

Rice LB (2008) Federal funding for the study of antimicrobial resistance in nosocomical pathogens: no ESKAPE. J. infect. Dis. **197:** 1079-81

Rodrigue A, Quentin Y, Ladzunski A, Mejean V & Foglino M (2000) Two-component systems in *Pseudomonas aeruginosa*: why so many? *Trends. Microbiol.*, **8:** 498-504

Reimmann C, Beyeler M, Latifi A, Winteler H, Foglino M, Lasdunski A & Haas D (1997) The global activator Gac A of *pseudomonas aeruginosa* PAO positively controls the production of the autoninducer N-butyryl-homoserine lactone and the formation of the virulence factors pyocyanin, cyanide, and lipase. *Mol. Microbiol.* **425:** 309-19

Roberts V, Thompson EE, Pique ME, Perez MS & Ten Eyck LF (2013) DOT2: Macromolecular docking with improved biophysical models. *J. Comput. Chem.* **34:**1743-58

Rose T, Verbeken G, De Vos D, Merabishvili M, Vaneechoutte M, Lavigne R, Jennes S, Zizi M, Pirnay J-P (2014) Experimental phage therapy of burn wound infection: difficult first steps. *Int. J. Burns Trauma* **4**: 66-73

Roucourt B & Lavigne R (2009) The role of interactions between phage and bacterial proteins within the infected cell: a diverse and puzzling interactome. *Environ. Microbiol.* **11:** 2789-805

Sadikot RT, Blackwell TS, Christman JW & Princa AS (2005) Pathogen-host interactions in *Pseudomonas aeruginosa* pneumonia. *Am. J. Respir. Crit. Care Med.* **171:** 1209-1223

Schaible B, Taylor CT, Schaffer K (2012) Hypoxia increases antibiotic resistance in Pseudomonas aeruginosa through altering the composition of multidrug efflux pumps. *Antimicrob. Agents. Chemother.* **56:** 2114–2118

Schneidman-Duhovny D, Hammel M, Tainer JA & Sali A (2013) Accurate SAXS profile computation and its assessment by contrast variation experiments. *Biophys. J.* **105:** 962-74

Schuck A, Diwa A & Belasco JG (2009) RNase E autoregulates its synthesis in *Escherichia coli* by binding directly to a stem-loop in the *rne 5'* untranslated region. *Mol. Microbiol.* **72:** 470-8

Schuck P (2000) Size-distribution analysis of macromolecules by sedimentation velocity ultracentrifugation and Lamm equation modeling. *Biophys. J.* **78:** 1606-19

Schultz MJ, Speelman P, Zaat SA, Hack CE, van Deventer SJ & van der Poll T (2000) The effect of *Pseudomonas* exotoxin A on cytokine production in whole blood exposed to *Pseudomonas aeruginosa*. *FEMS immunol. Med. Microbiol.* **29:** 227-32

Schuster M & Greenberg EP (2006) A network of networks: quorum-sensing gene regulation in *Pseudomonas aeruginosa*. *Int J. Med. Microbiol.* **296:** 73-81

Schweizer HP (2003) Efflux as a mechanism of resistance to antimicrobials in *Pseudomonas aeruginosa* and related bacteria: unanswered questions. *Genet. Mol. Res.* **2:** 48-62

Shen J, Meldrum A & poole K (2002) FpvA receptor involvement in pyoverdine biosynthesis in *Pseudomonas aeruginosa*. *J. bacterial.* **184:** 3268-3275

Silby MW, Winstanley C, Godfrey SAC, Levy SB & Jackson RW (2011) Pseudomonas genomes: diverse and adaptable. *FEMS microbial.* Rev. **35:** 652-80

Smith EE, Buckley DG, Wu Z, Saenphimmachak C, Hoffman LR, D'argenio DA, Miller SI, Ramsey BW, Speert DP, Moskowitz SM, Burns JL, Kaul R & olson M V (2006) Genetic adaptation by *Pseudomonas aeruginosa* to the airways of cystic fibrosis patients. *Proc. Natl. Acad. Sci. U. S. A.* **103:** 8487-92

Stevens AM, Schuster M & Rumbaugh KP (2012) Working together for the common good: cell-cell communication in bacteria. *J. bacterial.* **194:** 2131-2141.

Stock AM, Robinson VL & Goudreau PN (2000) Two-component signal transduction. *Annu. Rev. Biochem.* **69:** 183-215

Stover CK, Pham XQ, Erwin a L, Mizoguchi SD, Warrener P, hickey MJ, Brinkman FS, Hufnagle WO, Kowalik DJ, Lagrou M, Garber RL, Goltry L, Tolentino E, Westbrock-Wadman S, Yuan Y, Brody LL, Coulter SN, Folger KR, Kas a, Larbig K, et al. (2000) Complete genome sequence of Pseudomonas aeruginosa PAO1, an opportunistic pathogen. *Nature* **406:** 959-64

Svergun DI (1992) Determination of the regularization parameter in indirect-transform methods using perceptual criteria. *J. Appl. Crystallogr.* **25:** 495-503

Svergun DI (1999) Restoring low resolution structure of biological macromolecules from solution scattering using simulated annealing. *Biophys J*. 2879-86

Svergun DI, Barberato C & Koch MHJ (1995) CRYSOL - a Program to Evaluate X-ray Solution Scattering of Biological Macromolecules from Atomic Coordinates *J. Appl. Cryst.* **28:** 768-73

Svergun DI, Petoukhov MV & Koch MHJ (2001) Determination of domain structure of proteins from X-ray solution scattering. *Biophys. J.*, **80:** 2946-53

Symmons MF, Williams MG, Luisi BF, Jones GH & Carpousis AJ (2002) Running rings around RNA: a superfamily of phosphate-dependant RNases. *Trends Biochem. Sci.* **27:** 11-18

Taghbalout A & Rothfield L (2007) RNaseE and the other constituents of the RNA degradosome are components of the bacterial cytoskeleton. *Proc. Natl. Acad. Sci. U. S. A* **104:** 1667-1672

Taghbalout A & Rothfield L (2008) RNaseE and RNA helicase B play central roles in the cytoskeletal organization of the RNA degradosome. *Journ. Biol. Chem.***283:** 13850-55

Tanaka G, Shigeta M, Komatsuzawa H, Sugai M, Suginaka H & Usui T (1999) Effect of the growth rate of *Pseudomonas aeruginosa* biofilms on the susceptibility to antimicrobial agents: beta-lactams and fluoroquinolones. *Chemotherapy* **45:** 28-36

Thomas JA, Weintraub ST, Wu W, Winkler DC, Cheng N, Steven AC & Black LW (2012) Extensive proteolysis of head and inner body proteins by a morphogenetic protease in the giant *Pseudomonas aeruginosa* phage phiKZ. *Mol. Microbiol.* **84:** 324-39

Toder DS, Ferrell SJ, Nezezon JL, Rust L & Iglewski BH (1994) LasA and LasB genes of *Pseudomonas aeruginosa:* analysis of transcription and gene product activity. *Infect Immun.* **62:** 1320-7.

Tsai Y-C, Du D, DomÍnguez-Malfavón L, Dimastrogiovanni D, Cross J, Callaghan AJ, GarcÍa-Mena J & Luisi BF (2012) Recognition of the 70S ribosome and polysome by the RNA degradosome in *Eschrichia coli. Nucleic Acids Res.* **40:** 10417-31

Ueno H & Yonesaki T (2001) Recognition and specific degradation of bacteriophage T4 mRNAs. *Genetics* **158:** 7-17

Ueno H & Yonesaki T (2004) Phage-induced change in the stability of mRNAs. *Virology* **329:** 134-41

Van den Bossche A (2015) Identification and characterization of interactions between bacteriophage proteins and protein complexes of *Pseudomonas aeruginosa*. PhD thesis

Vanzo NF, Li YS, Py B, Blum E, Higgins CF, Raynal LC, Krisch HM & Carpousis AJ (1998) Ribonuclease E Organizes the protein interactions in the Escherichia coli RNA degradosome. *Genes Dev.* **12:** 2770-81

Vogel J & Luisi BF (2011) Hfq and its constellation of RNA. *Nat. Rev. Microbiol.* **9:** 578-89

Volkov VV and Svergun DI (2003) Uniqueness of ab-initio shape determination in small-angle scattering. *J. Appl. Cryst*. **36**: 860-864.

Wagner EGH (2009) Kill the messenger: bacterial antisense RNA promotes mRNA decay. *Nat. Struct. Mol. Biol.* **16:** 804-6

Walhout AJ, Vidal M (2001) Protein interaction maps for model organisms. *Nat. Rev. Mol.Cell Biol.* **2:** 55-62

Walkinshaw MD, Taylor P, Sturrock SS, Atanasiu C, Berge T, Henderson RM, Edwardson JM & Dryden DTF (2002) Structure of Ocr from Bacteriophage T7, a protein that mimics B-form DNA. *Mol Cell.* **9:** 187-94

Walsh CT, Wencewicz TA (2013) Prospects for new antibiotics: a molecule-centered perspective. *J. Antibiot.* **67:** 7-22

Walters MC 3rd, Roe F, Bugnicourt A, Franklin MJ & Stewart PS (2003) Contributions of antibiotic penetration, oxygen limitation, and low metabolic activity to tolerance of *Pseudomonas aeruginosa* biofilms to ciprofloxacin and tobramycin. *Antimicrob. Agents Chemother.* **47:** 317-323

Watanabe Y & Inoko Y (2009) Size-exclusion chromatography combined with small-angle X-ray scattering optics. *J. Chrom. A* **44:** 7461-65

Watanabe Y & Inoko Y (2011) Further application of size-exclusion chromatography combined with small-angle X-ray scattering optics for characterization of biological macromolecules. *Anal. Bioanal. Chem.* **399:** 1449-53

Westritschnig K, Hochreiter R, Wallner G, Firbas C, Schwameis M & Jilma B (2013) A randomized, placebo controlled phase I study assessing the safety and immunogenicity of a *Pseudomonas aeruginosa* hybrid outer membrane protein OprF/I vaccine (IC43) in healthy volunteers. *Hum. Vaccin. Immunother.* **10:** 170-183

Williams P & Camara M (2009) Quorum sensing and environmental adaptation in *Pseudomonas aeruginosa*: a tale of regulatory networdks and multifunctional signal molecules. *Curr. Opin. Microbiol.* **12:** 182-191.

Williams BJ, Dehnbostel J & Blackwell TS (2010) *Pseudomonas aeruginosa*: host defence in lung diseases. Respirology **15:** 1037-56

Winsor GL, Lam DK, Fleming L, Lo R, Whiteside MD, Yu NY, Hancock RE & Brinkman FS (2011) *Pseudomonas* genome database: improved comparative analysis and population genomics capability for *pseudomonas* genomes. *Nucleic Acids Res.* **39:** D596-D600.

Wodak S, Vlasblom J, Turinsky A & Pu S (2013) Protein-protein interaction networks: puzzling riches. *Struct. Biol.* **23**: 941-53

Yali G, Jing C, Chunjiang L, Cheng Z, Xiaoqiang L and Peng Y (2014) Comparison of pathogens and antibiotic resistance of burn patients in the burn ICU or in the common burn ward. *Burns* **40:** 402-407

Yoshida K, Nakayama K, Kuru N, Kobayashi S, Ohtsuka M, Takemura M, Hoshino K, Kanda H, Zhang JZ, Lee VJ & Watkins WJ.(2006) MexAB-OprM specific efflux pump inhibitors in *Pseudomonas aeruginosa*. Part 5: Carbon-substituted analogues at the C2-position. *Bioorg. Med. Chem.* **14:** 1993-2004

Zhang L & Mah TF (2008) Involvement of a novel efflux system in biofilm-specific resistance to antibiotics. *J. Bacteriol.* **190:** 4447-52

Zhang M, Su s, Bhatnagar RK, Hassett DJ & Lu LJ (2012) Prediction and analysis of the protein interactome in *Pseudomonas aeruginosa* to enable network based drug-target selection. *PLoS One* **7:** e41202

Appendices

Appendix 1

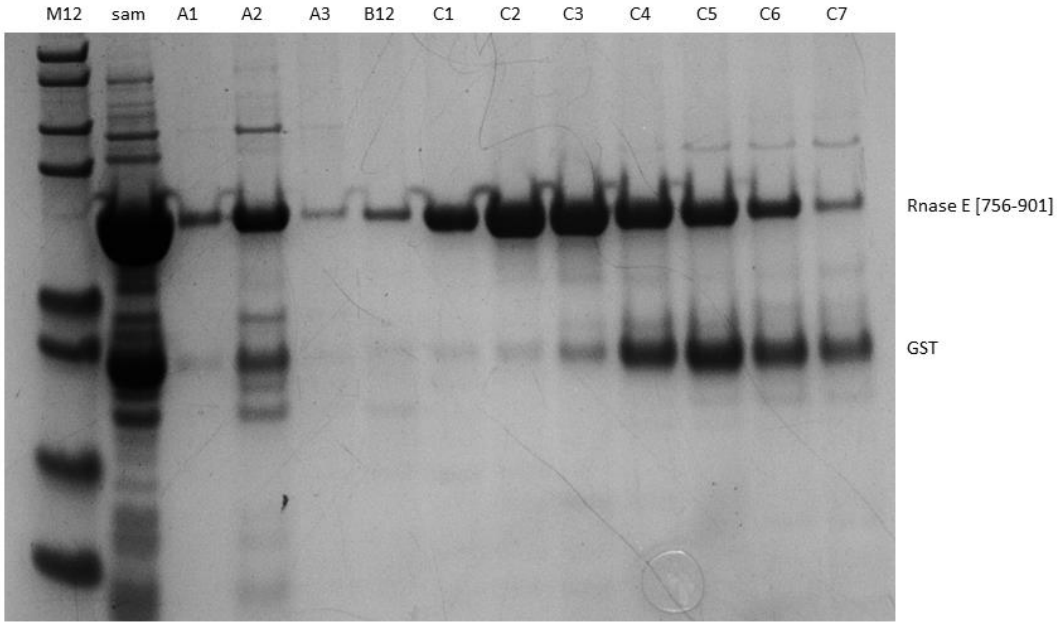

Figure S1: SDS-PAGE gel of RNase E [756-901] after affinity purification with a heparin column. Fractions B12 to C3 were used for EMSA experiments. M12, Mark 12 molecular weight ladder; sam, injected sample; GST, cleaved GST-tag.

Appendix 2

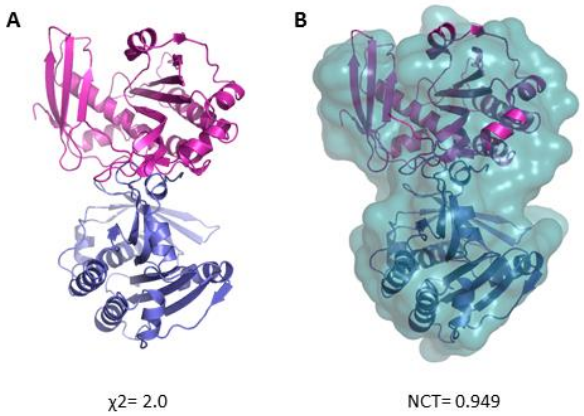

Figure S2: Rigid body modelling of two Dip monomers. A: SASREF was used to model two Dip monomers as rigid bodies against the Dip17 scattering data. From the crystal structure, a sheet interaction between residues 122-124 and 254-256 on both monomers was identified and set as the dimer interface. The final fit against the Dip17 scattering data was with χ^2=2.0. B: A low resolution envelope of AdjDip was generated in Pymol and used to assess the rigid body model for Dip. When superimposing the rigid body model on the AdjDip envelope, an NCT=0.949 is calculated, which indicates the rigid body model is in good agreement with the AdjDip conformer.

Appendix 3

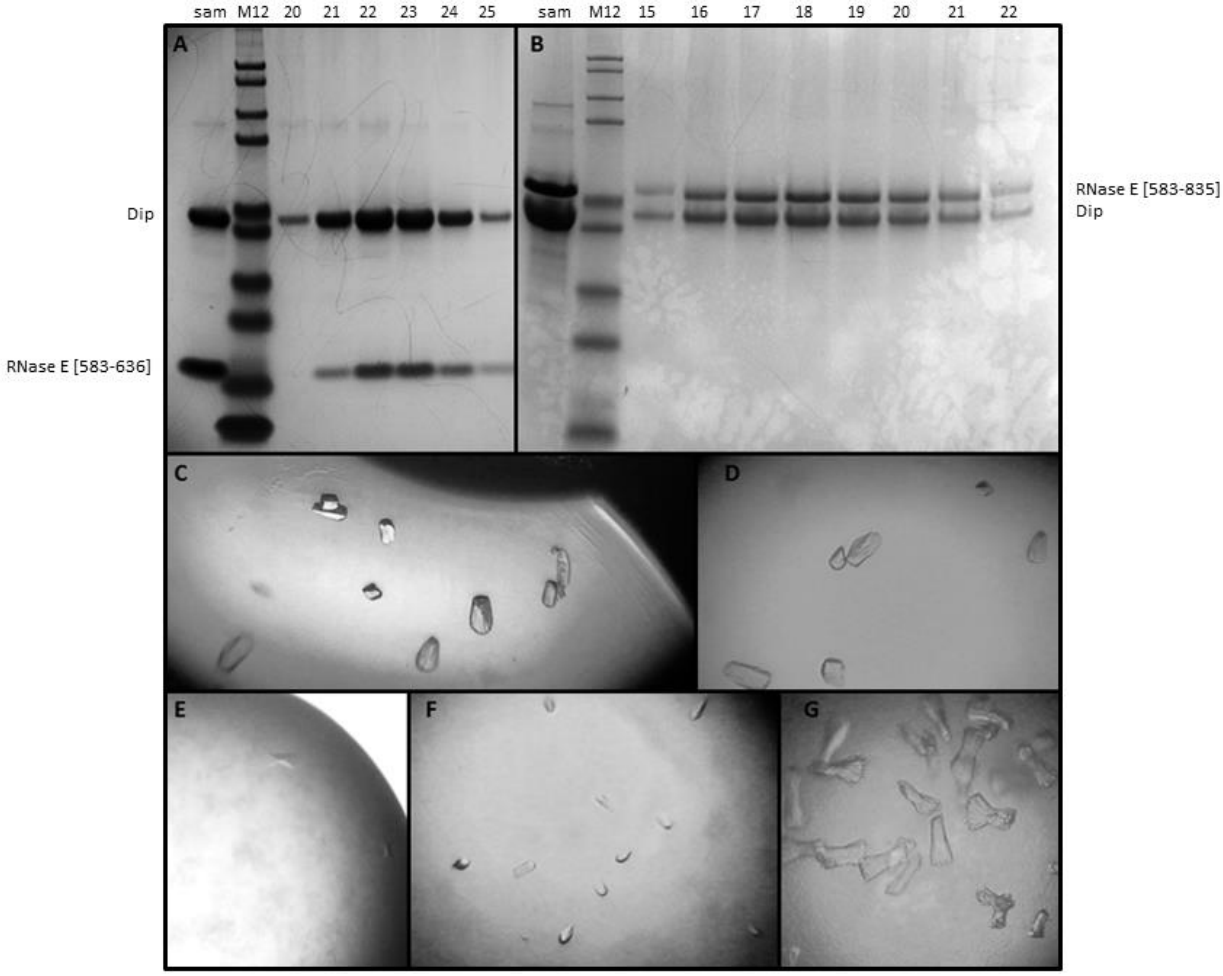

Figure S3: Co-purification of Dip and RNase E fragments and subsequent crystallization screens. A: SDS-PAGE of Dip and RNase E [583-636] after co-purification by size exclusion chromatography. B: SDS-PAGE of Dip and RNase E [583-835] after co-purification by size exclusion chromatography. C-G: Crystals obtained for the Dip + RNase E [583-835] complex after screening several conditions. Since the Dip + RNase E complex is highly transient, most of the resulting crystals were Dip crystals. Therefore, only the crystals that looked significantly different from the Dip crystals are presented here. The crystallization conditions were: 0.2 M sodium acetate, 0.1 M sodium citrate pH 5.5, 5 % (w/v) PEG 4000 (C,D); 0.1 M MES pH 6.5, 15 % (v/v) PEG 550 monomethyl ether (MME) (E); 0.1 M sodium acetate, 0.2 M sodium citrate pH 5.5, 7 % (w/v) PEG 4000 (F); 0.3 M sodium acetate, 0.1 M sodium citrate pH 5.5, 5% (w/v) PEG 4000 (G).

Appendix 4

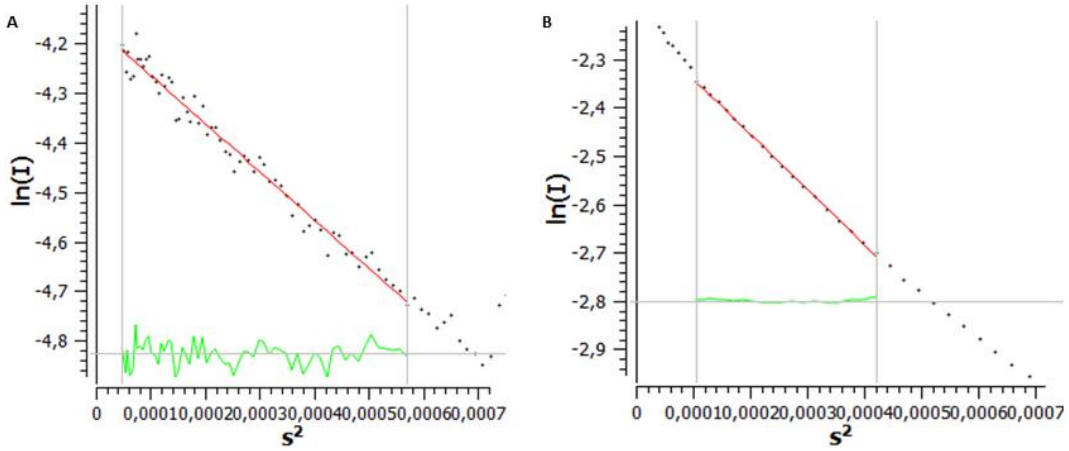

Figure S4: Guinier plots for the DipR1 and DipR2 scattering datasets. Ln(I) (y-axis) is plotted as a function of s^2 (x-axis). A: Since there is no obvious 'smiling' or 'frowning' of the curve in the highest s-regions of the DipR1 scattering profile, no aggregation is expected for this dataset. Furthermore, the fidelity of this Guinier approximation is 0.93 B: No obvious aggregation is expected for the DipR2 scattering profile either, since a good linearity is observed in the lowest s regions, with a fidelity of 0.88.

Appendix 5

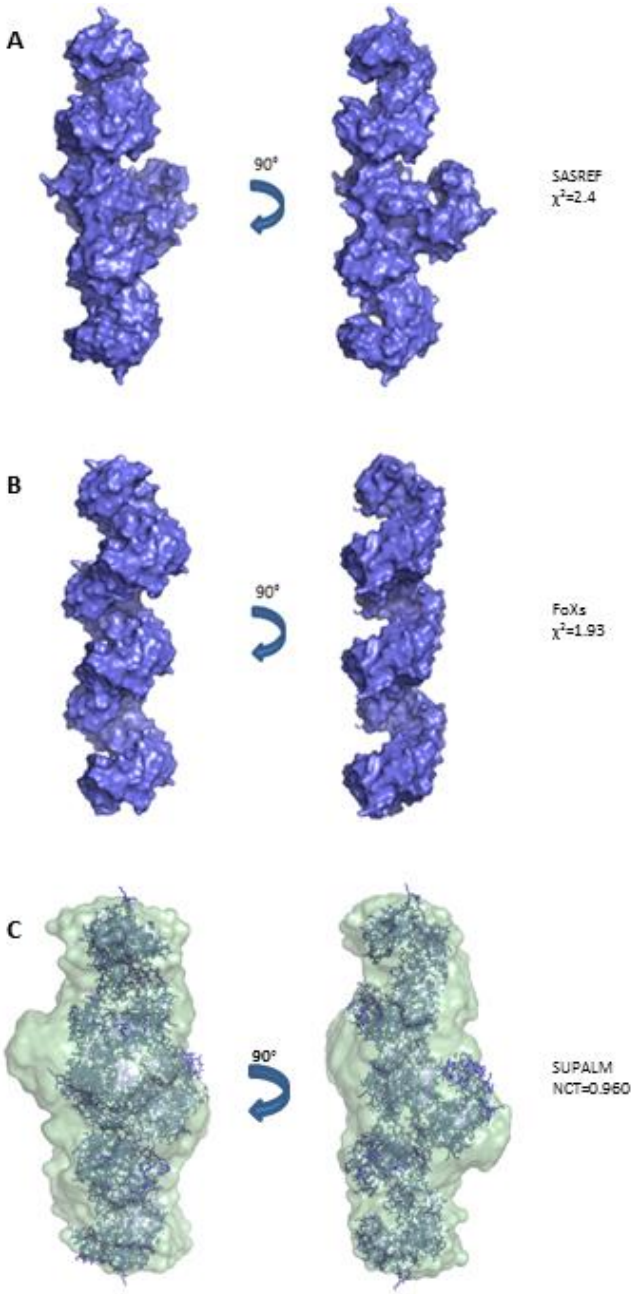

Figure S5: Rigid body modelling of three Dipα dimers against the DipR1 scattering data with SASREF. A: three Dipα dimers served as rigid bodies for the ab initio assembly of a trimer of dimers against the DipR1 scattering profile with SASREF. Although no clear helix is being formed, the upper and bottom dimers align well. A final χ^2= 2.4 was calculated. B: Hypothetical 'helical trimer of Dip dimers' built from Dipα dimers in PYMOL. A χ^2=1.93 against the DipR1 scattering data was calculated with FoXS. C: Superimposition of the rigid body model and an ab initio envelope of Dip + RNase E [583-835] (GASBOR) with SUPALM. From this superimposition, it is clear that the middle Dipα dimer is docked into the large density blob at the center of the ab initio model, which could explain why it's not being aligned with the top and bottom dimers by SASREF. Since about 60 kDa of density, i.e. two RNase E [583-835] fragments, in the ab initio model is not being accounted for by the three Dipα dimers, SASREF might have difficulties with aligning the dimers correctly into a helical trimer of dimers. Nevertheless an NCT= 0.960 was calculated for the superimposition.

Popularizing summary

Pseudomonas aeruginosa is a dangerous pathogen which contains a large genome and a broad regulatory network. This regulatory network allows for a rapid adaptation to changing environments and the colonization of a multitude of ecological niches. In addition, this opportunistic pathogen can cause life-threatening diseases, especially in immunocomprised persons. Moreover, due to the innovation gap in drug discovery and the irresponsible use of antibiotics during the past few decades, some *P. aeruginosa* strains have become resistant to all current antibiotics. Therefore, the need for new and inventive strategies to combat this superbug is urgent.

One strategy that has regained popularity in this context are bacteriophages, which are viral enemies of bacteria. Billions of years of co-evolution between these viruses and their host has driven the development of an impressive repertoire of mechanisms to kill bacteria fast and efficiently. In these mechanisms, direct interactions between bacteriophage-encoded proteins and bacterial complexes are of key importance. Since these mechanisms are often highly efficient, they are of interest in the search for new antibacterial targets.

Recently such an interesting and unique interaction has been revealed between a bacteriophage-encoded protein and a *P. aeruginosa* key complex, the RNA degradosome. This protein, which is termed 'degradosome interacting protein', Dip, inhibits the RNA degradosome by hijacking its RNA binding sites. As such the bacteriophage protects its mRNA, the 'intermediate code' in protein expression and thus its proliferation. In this dissertation the interaction between Dip an the RNA degradosome is further elucidated both structurally and functionally. As such the RNA degradosome might be considered as a new antibacterial target. Since the binding pocket of Dip is fully characterized in this dissertation, virtual Dip-based small molecule inhibitors can be designed for therapeutic purposes. Moreover, the research presented here indicates that Dip might be the first member of a class of RNA mimicry.

However, Dip has more potential than just therapeutic applications. Since Dip also binds the RNA degradosome of other, more distant bacteria it might hold great premise as a novel biotechnological tool. For example, It is conceivable that Dip could improve large scale protein expression in an expression strain by protecting mRNA. In addition, deletion mutants are being used nowadays to identify the ribonuclease responsible for the degradation of a specific structured RNA substrate under a given experimental condition. Since Dip inhibits RNase E, which is a subunit of the RNA degradosome, it can be used to efficiently identify or rule out RNase E as the responsible degrading ribonuclease. Finally, it is not unthinkable that well known biotechnological tools such as CRISPR-Cas, RNA interference or antisense RNAs would benefit from a direct inhibitor of the RNA degradosome.